Role of transport versus fueling upon pedestal density

Saskia Mordijck

Department of Physics

The College of William and Mary

Rich Groebner

DIII-D Experimental Science Group

General Atomics

Jerry Hughes

Plasma Science and Fusion Center

Massachusetts Institute of Technology

Ahmed Diallo

NSTX-U Experimental Team

Princeton Plasma Physics Laboratory

Q4 Report and final report

for the period:

October 1, 2018 through September 30, 2019

submitted on

October 1, 2019

Contributors to FY19 Joint Research Target

Livia Casali, GA
Ahmed Diallo, PPPL
Rich Groebner, GA
Jerry Hughes, MIT PSFC
Florian Laggner, PPPL
Tony Leonard, GA
Saskia Mordijck, William and Mary
Auna Moser, GA
Oak Nelson, Princeton University
Tom Osborne, GA
Richard Reksoatmodjo, William and Mary
Aaron Rosenthal, MIT PSFC
Filippo Scotti, LLNL
Aaron Sontag, ORNL
Vlad Soukhanovskii, LLNL
Huiqian Wang, GA

FY19 Joint Research Target: Milestone Statement

The edge pedestal is a vital component in achieving overall high confinement in a magnetic fusion device. Therefore, obtaining a physics understanding and predictive capability for the pedestal height and structure is a major goal of domestic and international fusion research. Great progress has been made in understanding the pressure limits imposed by MHD stability on pedestals in tokamaks. It is now clear, though, that the goal of predictive capability for the pedestal structure requires advances in the physics understanding of the separate structure of density and temperature profiles in the pedestal region. A key challenge is to understand the importance of particle sources in determining the density pedestal and project to burning plasma scenarios. Experiments on DIII-D and archived data from C-Mod, DIII-D, and NSTX will be used to test how fueling, reduced recycling, and transport affect the density pedestal structure. The role of divertor geometry strongly affects ionization properties and thus its effect upon the pedestal structure will be investigated. US researchers involved in collaborative activities on international experiments and at university facilities may gather, analyze and contribute data to this research effort.

4th Quarter Targets

Consolidate and synthesize results from the analysis together with any results from analysis and/or simulation of data from international and/or university devices. Prepare a joint report documenting the progress made toward the JRT goals. Identify open issues and provide guidance for future work based on the JRT results.

4th Quarter Results

In Q4 the JRT team met the quarterly targets, in the process of completing the tasks discussed in this report.

- Consolidate and synthesize results from the analysis together with any results from analysis and/or simulation of data from international and/or university devices.
- Prepare a joint report documenting the progress made toward the JRT goals.
- Identify open issues and provide guidance for future work based on the JRT results.

It was determined that, at this time, there was not a suitable pathway for incorporating data from international machines or university programs.

Executive summary

Fueling a future fusion reactor and the effects of fueling upon the pedestal structure is an open physics question that motivates an intensive community effort. The pedestal density is determined by a set of variables that affect both neutral dynamics as well as plasma transport. In this Joint Research Target (JRT) we are focusing on three major aspects that affect the pedestal density due to changes in fueling characteristics. This should indirectly also give us some insight into the plasma transport mechanisms in the pedestal region. The FY19 Joint Research Target brings together US expertise from multiple facilities and institutions to advance progress in this key research area. Contributions are being assembled by a number of US collaborators, in order to leverage high quality archival data from C-Mod and NSTX as well as utilize the unique capabilities of DIII-D. Overall the work explores the importance of localization of ionization as fueling source: that is, is the particle source for the discharge originating mainly in the core, pedestal, or scrape-off layer (SOL)? Specifically we are investigating three techniques for altering this localization:

- Variation in edge neutral opacity, see section 2,
- Shallow *vs.* deep plasma fueling, see section 3,
- Closed *vs.* open divertor configuration, see section 4.

High level summary of results The results in this report broadly show that devices with low opacity, primarily NSTX and DIII-D in this study, are able to modify the density pedestal with various techniques and locations of fuelling. Increased fueling with either more core sources or gas puffing typically increases the pedestal density. Data constrained modeling with 2D edge codes in some of these studies show that there is an ionization source in the pedestal and that a higher pedestal density is associated with a higher pedestal source. There is no strong reason to invoke the presence of a transport source (i.e., a pinch) to fuel the plasma from the open fields lines.

In contrast, experiments in C-Mod reached high SOL neutral opacities, near those expected on ITER. At these high opacities, C-Mod found that the density pedestal did not increase with increased gas puffing, as is expected for an opaque SOL. This result suggests that little if any of the density source came from within the pedestal. Despite the fact that the only fueling source came from the open field lines, the pedestal density profile had a strong gradient inside the separatrix, similar to normal H-mode operation. These results suggest that a transport source (pinch) was necessary to fuel the pedestal from the open field lines, under these conditions of high opacity.

The research presented here represents significant steps in the characterization and understanding of the density pedestal, but it also highlights that predictive capability remains a challenge. Improved understanding of both the particle source and particle transport are required to fully understand these results, as well as to predict the pedestal density. Understanding particle transport requires strong coupling between experiment and modeling in order to identify the transport physics. A key need in such studies is an improved quantitative knowledge of the source. In turn, an improved knowledge of the source requires measurements of the neutral source.

Summaries of research in the three sections noted above follow. In addition, we also have a section highlighting new diagnostic capabilities to measure the particle source in the pedestal, developed during this JRT, in section 1.

Measurements of neutral density In order to further our understanding of how the edge density pedestal is determined in tokamaks, it is critical to close the loop on the edge ionization

source. This has motivated improved experimental characterization of main chamber neutral density and ionization profiles. The ENDD instrument on NSTX was adapted successfully for use on NSTX-U during its initial campaign, allowing observation of well-resolved profiles of Balmer alpha emission from the NSTX-U plasma edge. These measurements were augmented with passive signals obtained from GPI, and the combined data were inverted to produce radial emissivity profiles. This made possible estimation of the upper bound of edge neutral density, under the assumption that all emission is due to electron impact ionization of atomic deuterium. Simulations using DEGAS2 were used to validate the interpretation of these data, and demonstrated that the emission observed inside the separatrix was dominated by electron impact ionization as assumed, while emission in the lower temperature SOL is dominated by molecular contributions. In recent DIII-D experiments supporting this JRT, filterscopes measuring main chamber Balmer alpha were used to provide an estimate of the edge neutral density during gas fueling scans along with the recent installation of a LFS/HFS Lyman alpha profile diagnostic. All these diagnostic advancements will provide valuable data for the validation of edge simulation tools.

Effect of opacity Generally speaking, *neutral opacity* is a representation of the likelihood that a launched neutral ionizes before entering the confined plasma, and thus indicates the degree to which neutrals may influence the edge pedestal structure. A commonly used screening parameter is the product of the plasma density and device size, $n \times a$. The three devices available in the US span a significant range of this parameter. On a single machine, it is also possible to perform experimental scans of density in order to directly test the impact of neutral penetration on the pedestal.

Our current understanding of the pedestal density structure is based mostly on low to moderate opacity experiments, while next step devices can expect to operate in very opaque SOL conditions. Understanding how moving the ionization source further away from the separatrix and how this affects the pedestal structure and overall performance is vital (DIII-D and C-Mod contributions). Principal results from this work include:

- In a series of experiments on DIII-D and C-Mod in which the SOL opacity was increased, modeling shows that neutral penetration was reduced with increasing opacity.
- C-Mod achieved SOL opacities close to those expected in ITER.
- At ITER-relevant opacities achieved in C-Mod, a normal electron density pedestal profile was observed.

Effect of fueling location To investigate the role of ionization deeper inside the separatrix, we test fueling strategies such as pellets and supersonic gas injection, which can penetrate up to the pedestal top (DIII-D and NSTX contributions). Both 'core' fueling and opacity affect the radial deposition of neutrals and thus affect the pedestal density. However counter to plasma dynamics, neutrals act independent of the magnetic field structure, resulting in a poloidally non-uniform distribution. Principal results from this work include:

- Analysis of NSTX data with high and low side gas fuelling and supersonic gas injection found that higher pedestal densities correspond to wider density pedestals, which suggests that the impact of fuelling location is weak.
- Analysis of DIII-D data indicates that deeper radial fuelling with pellets increased the pedestal density compared to equal edge fuelling from gas.

Effect of divertor geometry Through changes in the divertor geometry we can restrict neutrals

from penetrating the pedestal structure. This allows us to investigate their effect upon the pedestal structure. In DIII-D, we observe that pedestal depends strongly on changes in fueling through a change in divertor geometry. No changes in transport are necessary and so far the level and role of transport is difficult to identify. Principal results from this work include:

- Increased baffling of neutrals with divertor configuration reduced ionization source in pedestal.
- Increasing the particle source in the pedestal caused an increase of pedestal density. There is no compelling need to invoke changes in transport in order to explain the result.
- Studies in various divertor configurations indicate that details of particle source have significant effects on pedestal pressure.

1 Measuring the neutral density in C-Mod, DIII-D and NSTX

1.1 Introduction

Inferring the neutral density in the edge of a fusion plasma is a significant experimental challenge, requiring one to combine accurate local measurements of both neutral emissivities (*i.e.* atomic transitions in the visible or UV) and rate-determining plasma parameters (*i.e.* electron temperature T_e and density n_e). However, if this inference can be made robustly, and with sufficient spatial resolution, it enables construction of radial ionization rate profiles and thus the pedestal fueling source.

To date most work in this area has aimed to combine T_e, n_e from Thomson scattering diagnostics with emissivity measurements from neutral deuterium. The most easily measured line from D is the visible Balmer alpha ($D_\alpha : 3 \rightarrow 2$) transition at 656nm. D_α measurements are often routine, such as from filterscopes on DIII-D [21], however the emissivity measurement may be impacted by in-vessel reflections, and also by parasitic contributions from molecular species. These effects are less significant for the 121nm Lyman alpha ($Ly_\alpha : 2 \rightarrow 1$) transition, which may also be measured using vacuum compatible optics [10].

Both approaches have been used previously to compute radial profiles of ionization rates on the C-Mod tokamak, beginning with the first implementation of *in vacuum* arrays for Ly_α on a tokamak [10]. High resolution midplane measurements of visible D_α were also available at times. Diagnosis of neutral emissivity on C-Mod enabled radial localization of the neutral source in the pedestal region [9, 39, 47], which in turn determined cross-field particle fluxes. These types of measurements helped demonstrate the phenomenon of main chamber recycling [48], the correlation of enhanced particle transport with edge fluctuation amplitudes [96, 22], the scaling of particle transport coefficients with plasma current [39] and the modification of the plasma boundary using auxiliary lower hybrid RF [35, 97, 26].

Measurements of D_α on DIII-D have also been used to constrain the neutral density both in the vicinity of the X-point [19] and in the main chamber [20]. These tools enabled a body of research aimed at characterizing the origin of neutrals in the main chamber, including the role of main chamber recycling [20, 101, 83]. They were also used to compute changes in midplane edge fueling during ELM cycles [27].

In the remainder of this section, we discuss work from the last year which contributed to our characterization of edge neutral density. We highlight the new capabilities developed on NSTX-U where ENDD measurements and DEGAS 2 simulations are compared. We also show how using mid-plane filterscope measurements on DIII-D, along with the measured electron density we can get an estimate for how the neutral density changed.

1.2 Neutral measurements and validation on NSTX-U

Deuterium neutral densities are inferred at the low field side (LFS) midplane of NSTX-U from deuterium Balmer α (D_α) emissivities. Measurements in this report are from the first NSTX-U experimental campaign [5]. Neutral density measurements and their validation via neutral transport simulations were developed for this JRT.

Measurements of D-α emissivity on the LFS midplane The main diagnostic employed in this work is the Edge Neutral Density Diagnostic (ENDD), which was re-developed for NSTX-U. The previous ENDD diagnostic in NSTX is described in Ref. [94] and shares with the NSTX-U diagnostic only the detector. Collection optics (25 mm F/1.4 C-mount lens) are located in a radial re-entrant viewport (10 inch in length) in the outer midplane of the NSTX-U vessel. A stainless steel in-vessel mirror is used to provide a tangential view of the LFS midplane covering a field of view extending approximately 20 cm radially and vertically at the tangency plane. The in-vessel mirror acts as a shutter to protect the 2 inch sapphire window from coatings generated by wall conditioning. The collected light is imaged onto a 5-feet-long coherent imaging bundle (1000×800 10 μm fibers, Schott). The fiber bundle relays the collected light outside the re-entrant viewport to a 100 mm F/2.8 collimating lens. The collimated light is filtered by a narrow-bandpass interference filter ($\Delta\lambda$=2 nm, Andover) centered at the D_α wavelength. The filtered light is then focused by a 50 mm F/1.4 lens onto the detector. The detector is a Charge Coupled Device (CCD) camera (DALSA 256T) with 128×127 4 μm square pixels with a 268 frames/s frame rate.

Some of the ENDD upgrades in NSTX-U were motivated by limits in the old system identified in the previous validation work [95, 94] via the Monte Carlo neutral transport code DEGAS 2 [93]. The diagnostic was moved to a different midplane port located two diagnostic bays away from the old location (60° toroidally). The field of view and the flat field response were optimized via a re-entrant viewport and an in-vessel mirror. A 5-feet-long fiber bundle was used to move the detector farther away from NSTX-U and allowed placing the bandpass interference filter between the collimating and focusing lenses, reducing vignetting due to filter blue-shift. Finally, it was chosen to image D_α emission instead of D_β due to the higher quality data available for molecular contribution to D_α emission.

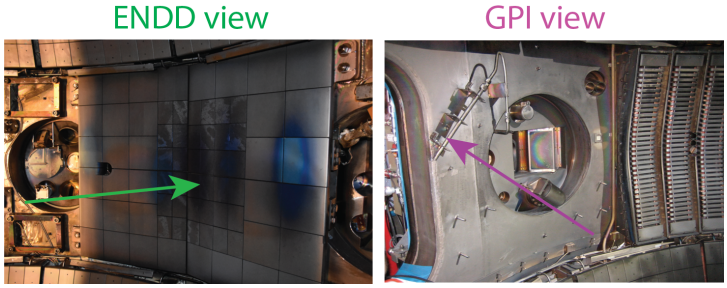

Figure 1: *View of the ENDD (left) and GPI (right) viewports from inside the NSTX-U vessel. Viewing directions are indicated with arrows.*

Two possible limitations with the new view and setup were the proximity of the neutral beam armor (i.e., a graphite recycling surface) to the edge of the plasma at this toroidal location (R=159 cm, with the typical Last Closed Flux Surface (LCFS) located at 150 cm). The second limitation is the time integration (3.7 ms), which leads to averaging over intermittent events (e.g., blobs). The latter can complicate the derivation of neutral density, given the non linearity of emissivity with respect to fluctuating plasma parameters [45]. To evaluate the possible impact of these two effects, a second D_α emissivity measurement was also considered. The field-aligned view of the LFS plasma edge from the gas puff imaging (GPI) diagnostic was utilized in passive mode (i.e., without active gas puff). The GPI view employs a Vision Research Phantom v710 CMOS detector with a 60×80 25 μm pixels and a 15-feet-long fiber bundle as image relay. The GPI diagnostic is located toroidally 150° away from the ENDD diagnostic. At this toroidal location there are no limiting surfaces besides the vessel wall. The GPI diagnostic is described in Ref. [107].

An image of the two diagnostics from inside the NSTX-U vessel is shown in Figure 1. The ENDD view is located below midplane with a near toroidal view. The GPI view is located below midplane with a field-aligned view. Viewing chords are show in green (ENDD) and purple (GPI) in a toroidal plan in Figure 2-left. The ENDD view is tangential to the plasma in front of the neutral beam

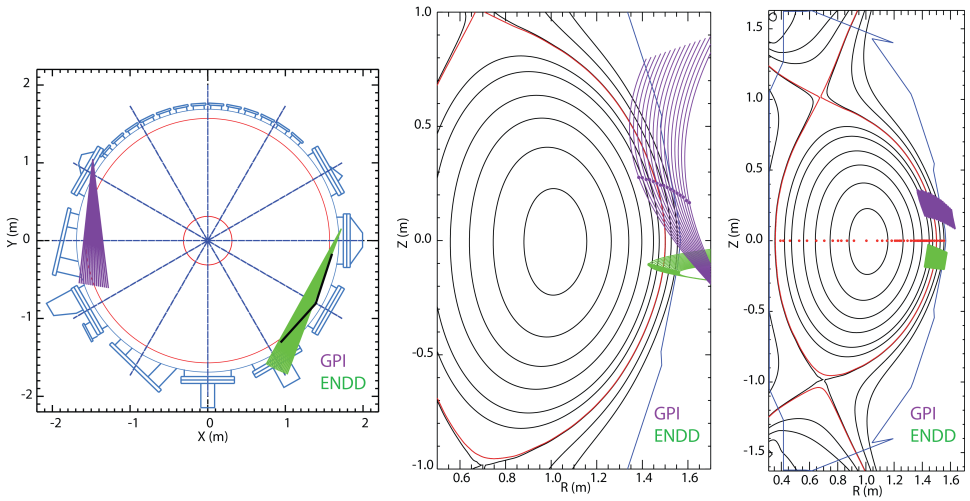

Figure 2: *Toroidal plan of NSTX-U with ENDD (green) and GPI (purple) views (left). Poloidal sightlines for ENDD (green) and GPI (purple) projected on a poloidal plane and overlaid to an NSTX-U equilibrium reconstruction (center). Tangency points for ENDD (green) and GPI (purple) overlaid to an NSTX-U equilibrium reconstruction.*

armor, indicated in black, while no limiting structure is present at the GPI toroidal location. The projection of a subset of sight-lines in a poloidal plane is shown in green (ENDD) and in purple (GPI) in Figure 2-center. Green (purple) markers indicate the tangency points. The tangency points for each pixel are then shown in green (purple) in Figure 2-right, overlaid to an NSTX-U equilibrium reconstruction.

ENDD and passive GPI were spatially calibrated in-vessel with a 3D measuring arm. The ENDD diagnostics was photometrically calibrated with an integrating sphere light source. The GPI diagnostics was cross calibrated to the ENDD diagnostic (peak-to-peak normalization) and only the emissivity profile shapes will be compared between GPI and ENDD in this report.

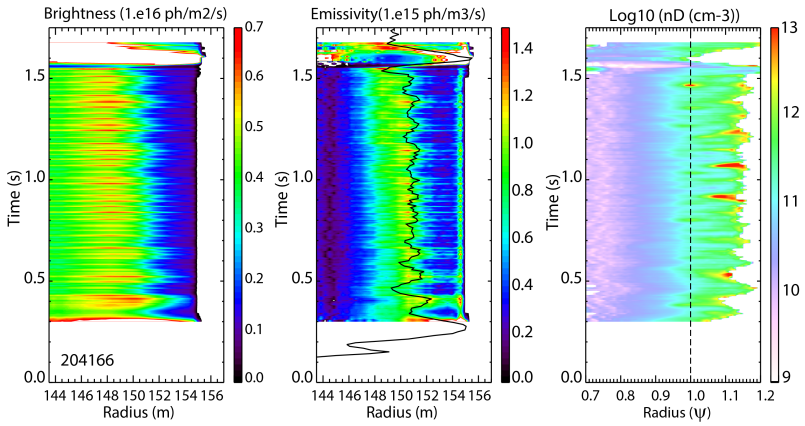

Figure 3: *Contour plot of Dα brightness as a function of major radius and time for NSTX-U discharge 204166 (left). Contour plot of Dα emissivity as a function of major radius and time with separatrix location overlaid in black (center). Contour plot of neutral density as a function of normalized poloidal flux and time (right).*

ENDD and passive GPI both provide line-integrated measurements through a D_α filter. A 3D inversion was developed to derive emissivity profiles from the ENDD and the GPI line integrated brightness. Local emissivity was calculated from brightness using a matrix inversion with the length matrix calculated for 3D geometry using EFIT equilibrium and assuming toroidal symmetry and constant emissivity along flux surface. Pixels from the 2D views were binned poloidally to improve the signal to noise ratio. Tangency radii were then mapped to the outer midplane (z = 0 m) for the direct use of Thomson scattering measurements for the derivation of neutral densities from the local emissivity.

Assuming that the D_α emissivity comes entirely from atoms excited by electron impact, the neutral density can be inferred from $n_D = E_{D_\alpha}/n_e/PEC(T_e, n_e)$ where PEC is the photon emission coefficient for electron impact excitation. In this work PEC coefficients calculated by the collisional radiative model used by DEGAS 2 are employed.

An example of ENDD data is shown in Figure 3 and 4. Figure 3-left shows a contour plot of the ENDD brightness as a function of radius and time for an NSTX-U L-mode discharge with sawtooth activity (204166). Figure 3-center shows a contour plot of the ENDD emissivity as a function of major radius and time. Overlaid in black is the separatrix location. Emissivity is peaked just inside the separatrix. From the local emissivity, an estimate for the neutral density is calculated assuming all the emission is due to electron impact excitation. The neutral density is plotted in Figure 3-right as a function of normalized poloidal flux (ψ_N) and time. Neutral density is approximately constant outside the separatrix, with an exponential decay inside the separatrix. Discharge parameters (input power P_{NBI}, plasma current I_p, line integrated density n_el, stored energy W_{MHD} and divertor D_α) are shown in Figure 4-left, while Figure 4-right shows the time evolution of n_e, T_e and n_D at ψ_N=0.9. During the discharge, n_e at this radial location is constant with a gradual decrease in T_e and a progressive increase in n_D over time. It should be noted however, that atoms excited by molecular processes can provide a significant contribution to D_α emissivity (especially in the SOL) and are neglected in the n_D values calculated by ENDD. In order to estimate the molecular contribution and to determine where and in which conditions the above assumption used for the n_D derivation from ENDD is valid, ENDD measurement were compared with simulations performed with the Monte Carlo neutral transport code DEGAS 2 [93].

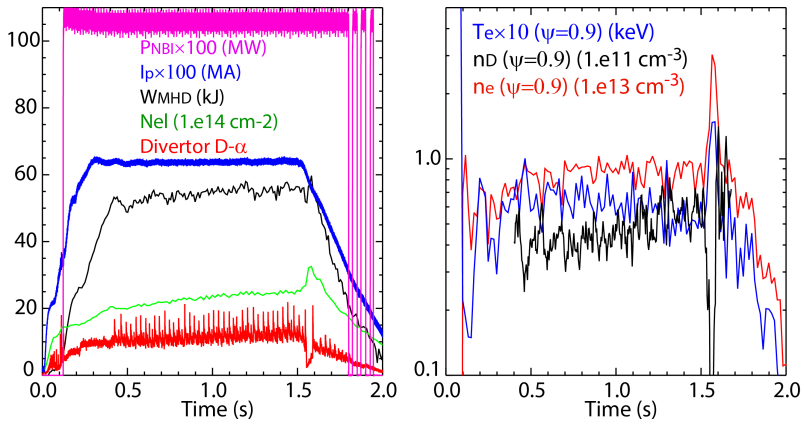

Figure 4: *Waveforms of I_p (blue), W_{MHD} (black), n_el (green), lower divertor D_α (red) and P_{NBI} (magenta) (left). n_e (red), T_e (blue) and n_D (black) at ψ_N=0.9 as a function of time (right).*

Monte Carlo neutral transport simulations with DEGAS 2 The Monte Carlo neutral transport code DEGAS 2 [93] was used in this work to validate the ENDD measurements, to gain a better understanding of the diagnostic measurements and to extract neutral densities and ionization profiles at locations where the ENDD measurements are not available. The general approach is similar to what described in [94].

A simulation box covering $R = [1.2, 1.6]$ m and $Z = [-0.4, 0.55]$ m was used in all the simulations (the last closed flux surface is typically at R = 1.5 m for z = 0). On the wall side at R = 1.6 m a solid interface is used with a uniformly distributed neutral source. The top and the bottom of the simulation box are exit interfaces. The simulation grid was generated based on experimental *partial kinetic* EFIT02 equilibrium reconstructions. Plasma parameters are based on the experimental T_e and n_e profiles, assumed to be flux functions. An automated workflow was developed to create input files, launch and post-process DEGAS 2 simulations. For each run four million particles were launched at the wall. The neutral atoms and molecules distribution was calculated (for a given wall source) and the relative D_α emissivity profile was calculated including contribution

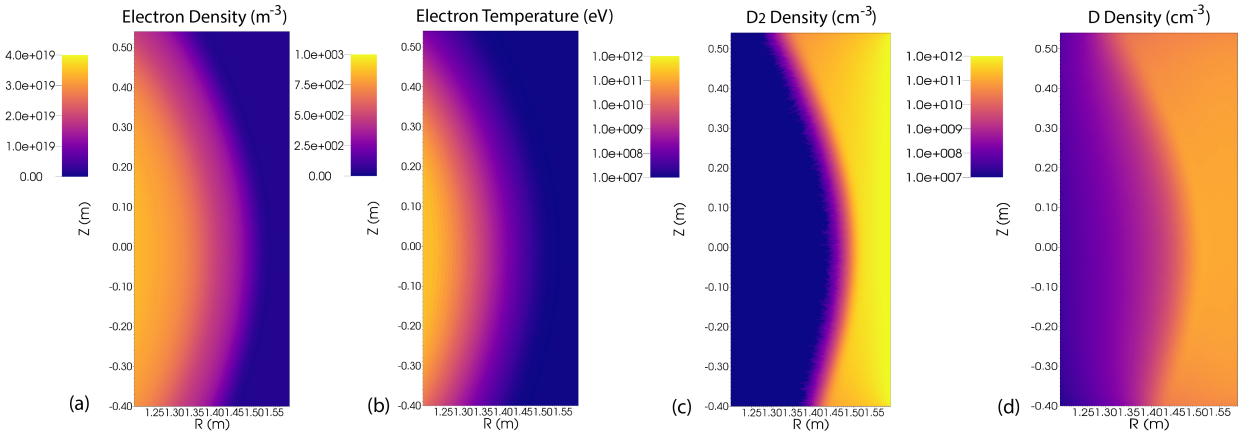

Figure 5: *Electron density (a) and electron temperature (b) input to the DEGAS 2 simulation for discharge 204563. Calculated atomic (c) and molecular (d) deuterium densities after normalization of simulated emissivity to the ENDD emissivity.*

due to electron impact excitation and excitation due to molecular processes. The simulated D_α emissivity was normalized to the experimental emissivity measured by the ENDD diagnostic. The normalization was then applied to the neutral densities calculated by DEGAS 2, allowing their absolute determination. The normalization was carried out either using the peak emissivity or using the emissivity value inside the separatrix. An example of T_e and n_e input values in the simulation box and the deuterium atomic n_D and molecular n_{D_2} densities calculated by DEGAS 2 for discharge 204563 are shown in Figure 5.

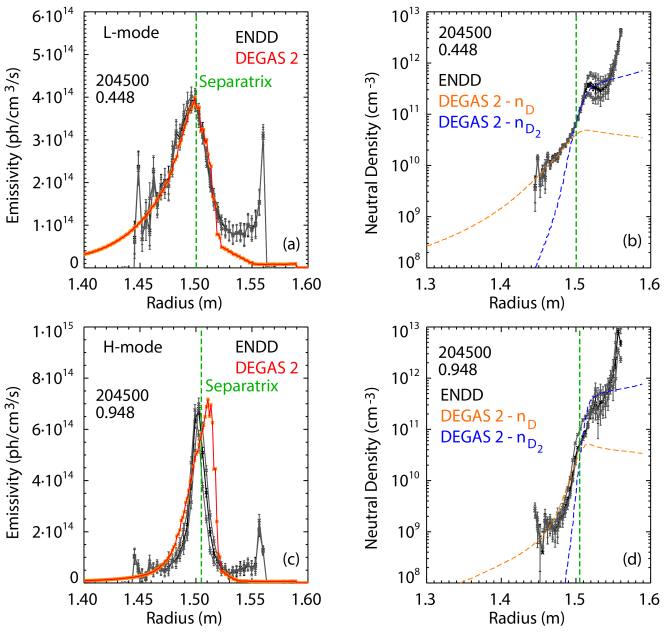

Figure 6: *Measured (black) and simulated (red) outer midplane D_α emissivity for an L-mode (a) and an H-mode (c) discharge. Measured outer midplane n_D (black) and simulated n_D (orange) and n_{D_2} (blue) for an L-mode (b) and an H-mode (d) discharge.*

From the DEGAS 2 simulations, we extract the following quantities:

- D_α emissivity profile shape,
- peak emissivity location,
- half width at half maximum on one side of the separatrix and on the outer of sperartrix of the D_α emissivity profile,
- neutral deuterium density inside the separatrix (1 cm), and
- integrated ionization rate.

These quantities are compared with those inferred from the ENDD diagnostic. Typically good agreement was observed in the D_α emissivity profile shape as shown in Figure 6 for an L- (a) and an H-mode (c) simulation. Peak emissivity, however, was systematically located at larger radii

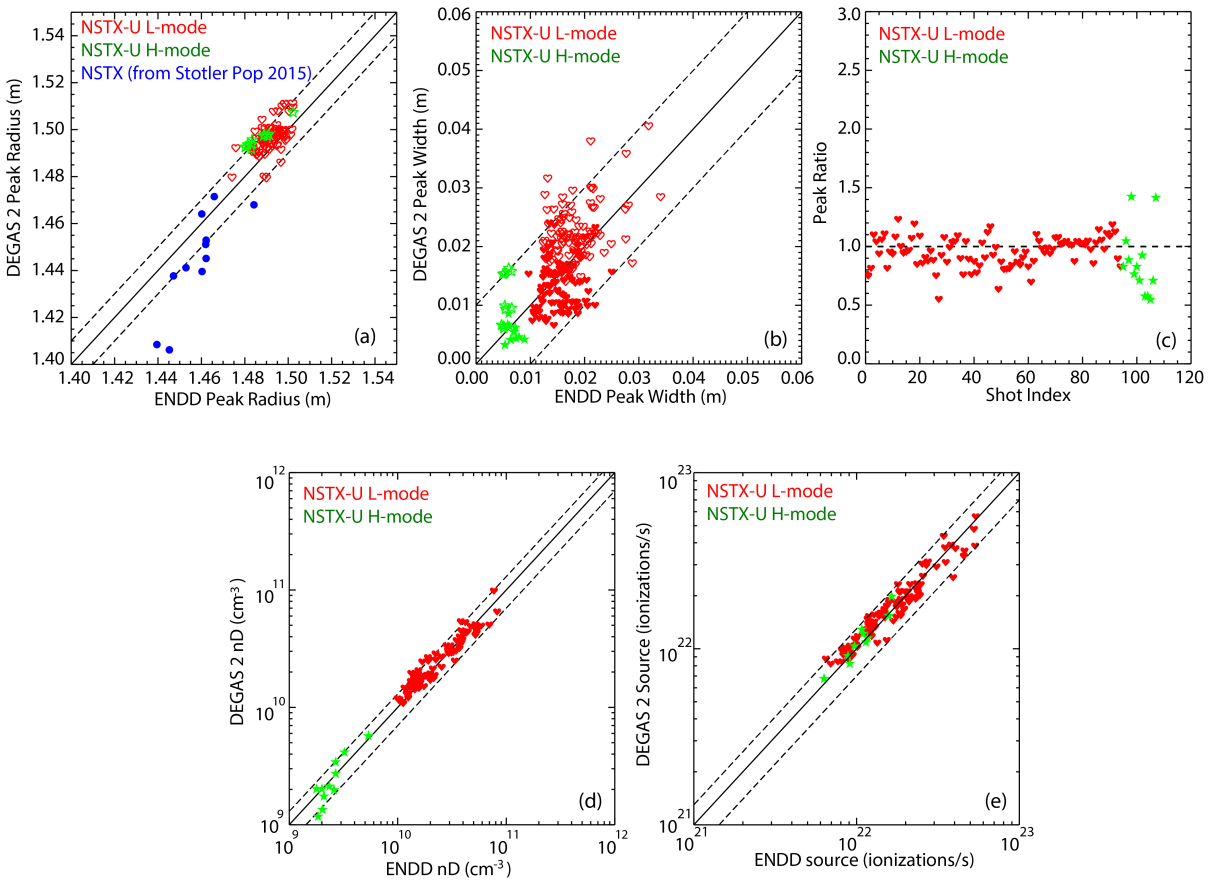

Figure 7: *(a) Peak D_α emissivity radius in DEGAS 2 simulations versus experiment. (b) Emissivity half width at half maximum in DEGAS 2 simulations versus experiment (SOL side - empty symbols, core side -filled symbols). (c) Ratio of peak emissivities between DEGAS 2 simulations and experiment. (d) n_D 1 cm inside the separatrix in DEGAS 2 simulations versus experiment. (e) Total ionization source in DEGAS 2 simulations versus experiment.*

in DEGAS 2 and appeared to be due to an excess in the predicted molecular contribution. The D_α emission in the far SOL (e.g., ∼R=1.55 m) was systematically under-predicted in the simulations. After the emissivity normalization, atomic deuterium densities inferred inside the separatrix were in very good agreement between ENDD and DEGAS 2 in both L- (b) and H-mode (d). In both cases, the shortest density gradient scale length is observed just inside the separatrix with a weaker neutral density gradient further in the core plasma. As mentioned in the previous section, the n_D inferred from ENDD (n_{D-ENDD}) represents an upper estimate of the actual n_D. It was observed that n_{D-ENDD} is accurate inside the separatrix where D_α emission is dominated by the contribution due to electron impact excitation. Furthermore, while in the SOL n_{D-ENDD} is only an upper estimate of the actual n_D, it tracked closely the profile of the sum of n_D and n_{D_2} as simulated by DEGAS 2.

Over 100 DEGAS 2 simulations were performed for different discharges and times in L- and H-mode conditions. The discharges were chosen to cover a large range of emissivities and neutral densities. The comparison between ENDD and DEGAS 2 is summarized in Figure 7. In the DEGAS 2 simulations, radii of peak emissivity were on average overestimated by ∼5 mm (Figure 7-(a)). The simulated emissivity profile half width at half maximum were on average in agreement in the core and wider in the SOL with respect to the experimental ones (Figure 7-(b)).

Two approaches for the profile normalization were tested: normalizing peak emissivities and normalizing by emissivities 1 cm inside the separatrix (where atomic contribution is dominant). While both approaches worked in L-mode, the latter (normalization by emissivity inside the separatrix) gave more reliable results in both L- and H-mode, where the simulated molecular contribution in the SOL was often overpredicted. The ratio of simulated and measured peak emissivity when the latter approach is used is shown in Figure 7-(c). Overall, good agreement was observed between DEGAS 2 and ENDD in both calculated neutral densities (7-(d)) and in a proxy for the total ionization source (7-(e)). The total ionization source proxy is here calculated from the volume integral of the low field side ionization rate (neglecting poloidal variations). Despite the small deviations in the simulated profiles, DEGAS 2 simulations indicated that the majority of the D_α emissivity inside the separatrix is due to electron impact excitation of neutral deuterium atoms, thereby confirming assumptions used in the ENDD neutral density derivation. ENDD densities and ionization rates were confirmed over two and one order of magnitude respectively. The validation of the ENDD measurements enables the use of neutral densities and ionization rate profiles in the core fueling analysis in the rest of the report.

Finally, in order to exclude diagnostics uncertainties as a possible source of the observed discrepancy, the ENDD emissivity profiles were compared with those measured passively with the GPI diagnostic. The GPI data were binned in time to obtain the same integration time used by ENDD (3.7 ms). A comparison between the ENDD (orange) and GPI (purple) emissivity (normalized to the ENDD peak emissivity) is shown in Figure 8. Both peak emissivity location and emission in the far SOL (e.g., at R = 1.55 m) show good agreement between the two diagnostics. The emissivity simulated by DEGAS 2 is overlaid in the same plot in black.

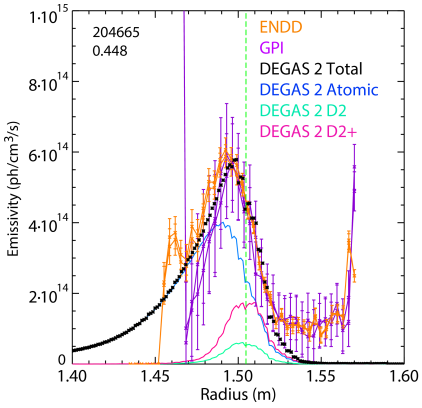

Figure 8: *ENDD (orange) and GPI (purple) Dα emissivity. Total emissivity from DEGAS 2 simulations is overlaid in black (with atomic, molecular ions and molecules plotted in blue, magenta and green, respectively).*

Deviations between the simulated and experimental peak emissivity location and SOL profile shape are thought to be related to uncertainties in the DEGAS 2 molecular model or to the possible role of intermittent transport. In order to evaluate the possible effect of intermittent transport in DEGAS 2 simulations, a scan in the far SOL T_e, n_e input profiles was performed starting from the experimental values. DEGAS 2 simulations are based on T_e, n_e from a single Thomson scattering profile, assumed to be representative of the steady state profiles. In the presence of intermittent SOL transport, due to the non-linearity of atomic physics coefficients with respect to T_e and n_e, the use of profiles from a single time point (or even time-averaged profiles) might not result in an accurate representation of the experimental emissivity. Minor changes in the far SOL T_e, n_e resulted in an improved agreement between the simulated and measured emissivity. A larger T_e in the far SOL was needed to increase the far-SOL emissivity (dominated by molecular contribution). The increase in far SOL T_e, n_e resulted in an increase molecular dissociation thereby reducing the molecular contribution to D_α emissivity around the peak location which was responsible for the observed outward shift. The results from the 2D scan are shown in Figures 9, 10. In Figure 9, top figures represent raw Thomson profiles (red) and DEGAS 2 input profiles (black) for the base case (left) and for a case in the 2D scan which provided a better agreement with the experimental profiles (right). The measured and simulated emissivities are shown on the bottom for the base (left) and optimized (right) cases. The variation of the difference in peak location and of the ratio of far SOL emission to peak

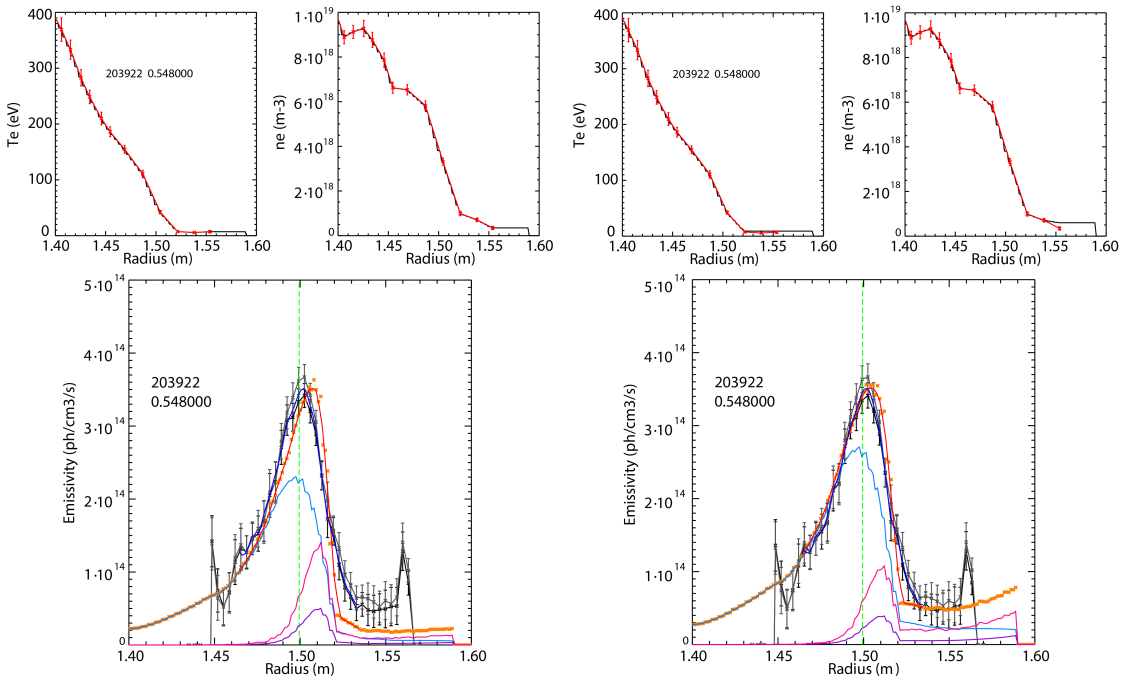

Figure 9: *Input T_e, n_e profiles (raw data in red and DEGAS 2 input in black) for base case (a,b) and optimized case (c,d). Radial profile of D_α emissivity for base case (e) and using for the optimized case (f): ENDD (black), DEGAS 2 (orange) with atomic (blue) molecular ions (magenta) and molecules contributions (purple) overlaid.*

emission are shown in Figure 10 as a function of T_e, n_e. For both quantities, the best agreement between simulation and experiment is observed for comparable T_e, n_e. It was then estimated how the contribution to emissivity due to molecular processes varied in the simulation based on raw profiles and in the one where profiles were modified to better match the experimental emissivity shape. Molecular contribution changed at the separatrix from 0.28 to up to 0.2 leading to only minor changes in the inferred neutral density and total ionization source inside the separatrix. This further justified the use of single-time Thomson profiles and the normalization approach chosen for the DEGAS 2 simulations.

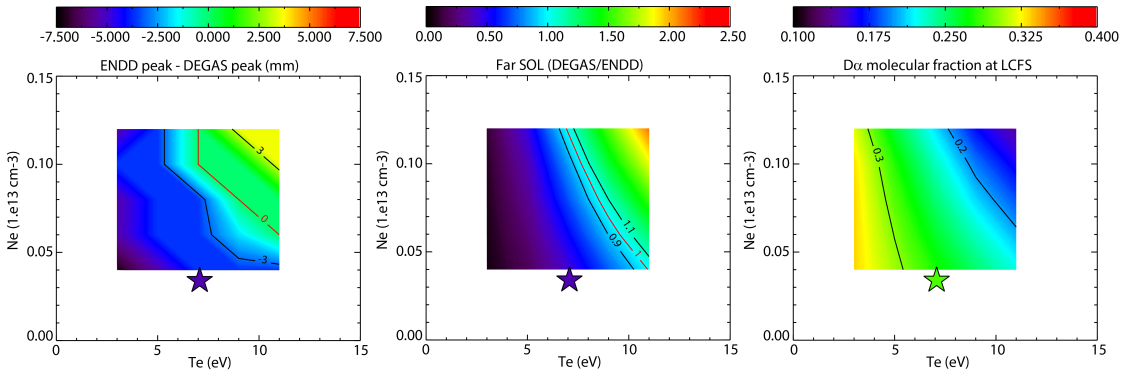

Figure 10: *Difference in peak location (left) and in ratio of far SOL emission (center) between DEGAS 2 simulations and ENDD as a function of T_e, n_e. Molecular fraction of D_α emissivity at the separatrix (right). Simulations carried out using raw experimental profiles are shown with a star.*

Neutral density profile shape

Next we extract the neutral density profile shape from the ENDD measurements and DEGAS 2 simulations and compare them with estimates for the ionization and charge exchange mean free paths in various experimental conditions. This is critical to build a fundamental understanding of the processes determining the neutral density profile and in turn assess its role in determining the pedestal structure.

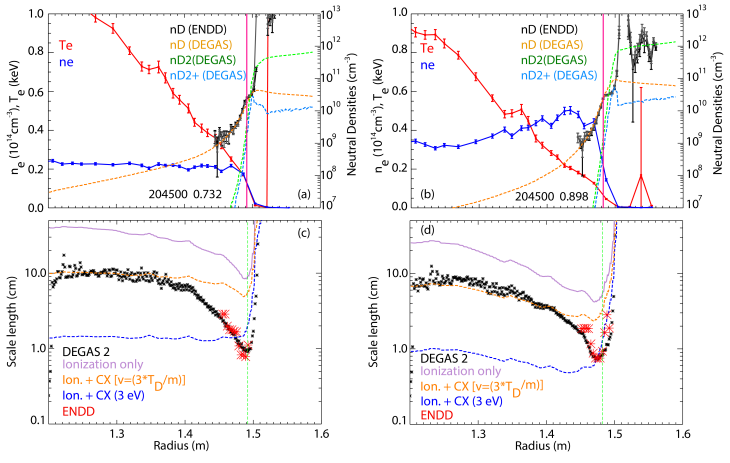

Figure 11: *Radial profiles of T_e, n_e, neutral densities (ENDD, DEGAS 2) for discharge 204500 at t=0.732s (a) and t=0.898s (b). Radial profile of neutral density radial scale length for discharge 204500 at t=0.732s (c) and t=0.898s (d).*

In Figure 11 (a,b), the radial T_e and n_e profiles are plotted as a function of major radius in red and blue, respectively. In the same plots, neutral densities are plotted (note the different vertical scales for n_e, T_e on the left and the neutral densities on the right): n_D from ENDD in black, n_D from DEGAS 2 in orange, n_{D_2} from DEGAS 2 in green and $n_{D_2^+}$ from DEGAS 2 in cyan. In Figure 11-(a) and -(b), the profiles are plotted for two different times during the same discharge: at 732 ms early after the transition to H-mode (during the pedestal build up) and at 898 ms at saturated pedestal.

In Figure 11-(c, d), for the same discharge/times, the neutral deuterium density scale length is plotted from the DEGAS 2 simulation in black together with the density scale length inferred from the ENDD measurements in red. Overlaid in purple is the ionization mean free path and in orange the mean free path from ionization and charge exchange calculated using the gas temperature T_D from the DEGAS 2 simulations. Overlaid in blue is the total ionization mean free path for 3 eV neutrals such as those generated by dissociation processes. In both plots, the separatrix location is indicated with a green dashed line.

We observe that well inside the pedestal top, the DEGAS 2 scale length agrees with estimates for charge exchange and ionization mean free path (as first discussed in [94]). The increase in the estimated total mean free path at smaller radii is due to the increase in T_D/T_i driven by charge exchange. In the steep gradient region and at the pedestal top, the DEGAS 2 and ENDD scale lengths (in very good agreement with each other) disagree with calculated mean free path for thermal neutrals. In particular, the scale lengths fall in between the mean free path calculated for thermal neutrals and the one evaluated for 3 eV neutrals, showing the possible importance of non-thermalized neutrals generated by molecular dissociation. A scan in n_e shows that the region showing disagreement is radially reduced with the increase in electron density.

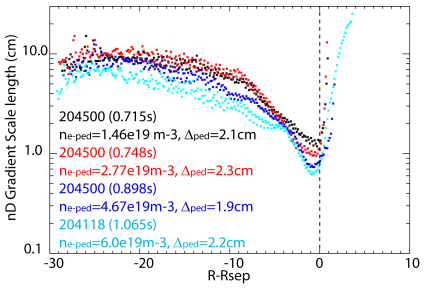

Figure 12: *Comparison of neural density radial gradient scale length for four different H-mode profiles with increasing pedestal density.*

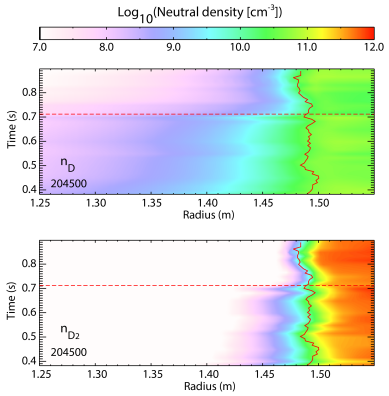

Figure 13: *Contour plot of neutral density (n_D and n_{D_2}) as a function of time and radius from coupled ENDD/DEGAS 2 analysis.*

The neutral density gradient scale length from DEGAS 2 was compared for four different H-mode experimental profiles: three profiles taken during the pedestal buildup from discharge 204500 and one from a high triangularity discharge (204118), see figure 12. As a result of the increase in separatrix and pedestal density (from 1.5 to 6.0 $\times 10^{19}\mathrm{m}^{-3}$), the predicted minimum neutral density gradient scale length decreased by nearly a factor of 2. Despite the changes in neutral density scale lengths, no change was observed in the pedestal width obtained from a modified hyperbolic tangent fit.

Comparison of neutral densities and ionization rate profiles Based on the completed validation effort for the ENDD measurements, neutral (atomic and molecular) density profiles can be obtained from the coupled ENDD/DEGAS 2 analysis while radial ionization profiles inside the separatrix can be directly inferred from the ENDD data. An example of neutral density profiles and their time evolution through an H-mode transition is shown in Figure 13 based on DEGAS 2 simulations at each Thomson time normalized by ENDD emissivity at each time.

In this section ionization rate and neutral density profiles directly inferred from ENDD are compared between L-mode and H-mode at different densities. Due to the lack of experimental scans during the prematurely-interrupted NSTX-U experimental campaign, the evolution during a single discharge is used to compare different conditions.

Figure 14 shows the time evolution of n_e pedestal height and pedestal width, neutral density at two different radial locations ($\psi_N = 0.9, 0.95$), peak ionization rate inside the separatrix and half width at half maximum of the ionization rate (towards the core plasma). This discharge transitioned into H-mode at 0.7 s (two more H-mode phases happen at later times after the discharge had H-L back transitions). An increase in peak ionization rate is observed with the transition to H-mode together with a reduction in the ionization rate width and a steep decrease in edge neutral density due to the increased n_e from the pedestal formation. The radial profiles are compared in Figure 15, where ionization rate and neutral densities are plotted at two nearby times both in L-mode (black) and just after the transition to H-mode. The ionization rate profile become more peaked in H-mode, with an approximately unchanged radial location of ionization rate maximum. In H-mode, during the pedestal build up, the peak ionization rate increased, with smaller changes in the ionization rate profile width and edge neutral densities.

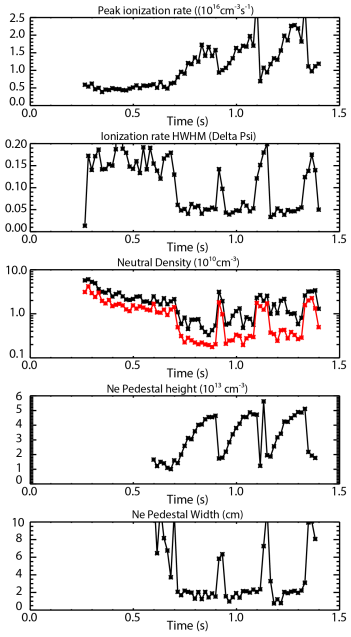

Figure 14: *Time evolution of peak ionization rate, ionization rate width, neutral density inside the separatrix and pedestal height and width for discharge 204500. In the third panel, the red and black traces represent the neutral density at $\psi_N = 0.9$ and $\psi_N = 0.95$, respectively.*

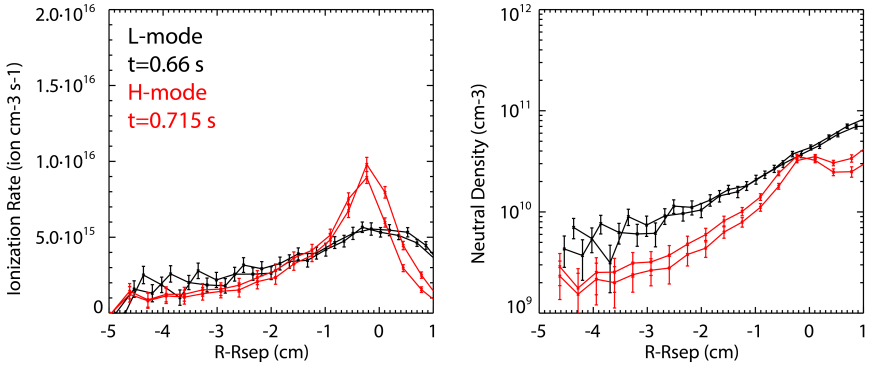

Figure 15: *Radial profiles of ionization rate (left) and neutral densities (right) for an L-mode time (black) and an H-mode time (red).*

1.3 Neutral measurements on DIII-D

Neutral density evaluation using filterscopes In Section 2 we will describe findings from a dedicated experiment on DIII-D that evaluated pedestal response to gas puffing, under a scan of neutral opacity. Key quantities to be inferred in this experiment are the neutral density and ionization rate in the pedestal and scrape-off layer region, at the midplane. To characterize the changes in neutral population we will use the midplane filterscope system on DIII-D.

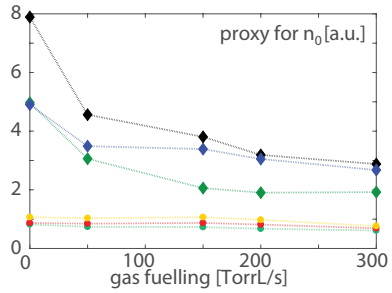

Figure 16: *Average L_{D_α}/n_e versus steady-state fueling levels for different radial midplane filterscope signals for DIII-D.*

The ionization rate of neutrals increases for higher n_e and T_e (up to $T_e \approx 100$eV). In our experiments, the electron temperature from the separatrix out varies weakly from discharge to discharge, and we thus increase the ionization rate predominantly by raising the electron density, enhancing the SOL 'opaqueness' to neutrals and reducing the penetration of neutrals inside the pedestal. We characterize the changes in neutral population using the midplane filterscope system on DIII-D, which measures filtered light using a group of radially spaced tangential chords near the midplane. The brightness profiles $L_{D_\alpha}(R)$ can in principle be inverted to emission using the geometrical properties of the system. The emission, I_{D_α} can then be related to the local neutral density, n_0, using $n_0 = I_{D_\alpha}/(n_e < \sigma\nu(T_e, n_e) >)$, where $< \sigma\nu(T_e, n_e) >$ is the electron excitation rate coefficient [20]. However, the inversion process depends on having an accurate spatial calibration of the system response and will not resolve feature scales that are smaller than the spacing of the filterscope channels. We therefore use the non-inverted brightness as a first order means of comparing the discharges. We assume that the variation in the electron excitation rate coefficient is small (the electron temperature in the SOL is similar), compared to the changes in n_e from discharge to discharge. Second, since all the plasmas have the same equilibrium and the midplane filterscope diagnostic geometry does not change, we use the brightness divided by the local electron density, L_{D_α}/n_e, as a proxy for n_0, as in figure 16.

This means we can compare the same filterscope signals from discharge to discharge, but the radial profile in itself needs to be adjusted using the geometrical factor. Figure 16 shows a strong decrease in our proxy for n_0 when more gas is added to increase the SOL n_e. Future work will include adding the geometrical factor as well as the correct excitation coefficient based on the local temperatures and densities using an atomic database.

Development of new main chamber Lyman alpha measurements The desire to better quantify edge particle transport has motivated the development of diagnostics that can measure profiles of Ly_α in DIII-D. Making this VUV measurement has advantages over the visible Balmar alpha line. The Lyman line is less subject to reflections from internal tokamak surfaces and it is not populated by excessive contributions from molecular deuterium in the same way the Balmer line is. However, because of its VUV wavelength, Ly_α must be measured in vacuum, which introduces greater technical challenges. Especially challenging is the carbon-rich environment on DIII-D. Intrinsic carbon impurity emits in a wavelength very close to the 121nm Ly_α line, putting strong demands on the spectroscopic rejection of one's imaging system. The high temperature bake on DIII-D also requires one to design in adequate water cooling.

These challenges were overcome, and a working main chamber Ly_α diagnostic was installed on DIII-D during FY19 [82]. It consists of two pinhole cameras viewing the low-field and high-field sides of the tokamak, 70cm below midplane, each with up to 20 tangential chords. Much like previous systems [10], photon detection is done using photodiodes with enhanced extreme UV response, behind optical filters with very high rejection outside of 121nm. Port geometry requires the use of additional mirrors to direct the light passing through the camera apertures onto filtered photodiodes. The mirrors have a narrow bandpass reflectivity that provide additional rejection of nearby impurity lines, mitigating the issue of unwanted carbon emission. The diagnostic is known by the whimsically recursive acronym LLAMA (LLAMA, the Lyman Alpha Measurement Apparatus).

Initial operation of the LLAMA has been quite promising. Shortly after the apertures were unshuttered, the signals from the low-field side view were digitized and filtered for noise to reveal reasonable profiles and time histories. An example of a time trace from a chord passing through the SOL is shown in Fig. 17. The signal has been processed to remove electronic pick-up, but still reveals key anticipated signatures: namely the drop in neutral emission following a transition from L-mode to H-mode and the spikes associated with edge-localized modes (ELMs).

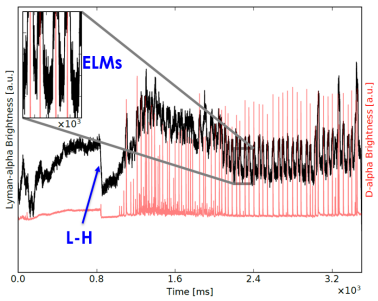

Figure 17: *Demonstration of the new LLAMA diagnostic. Black: time trace of Lyman alpha brightness from a single tangential chord on DIII-D. Red: Comparison Balmer alpha trace from a filterscope.*

Minor improvements to the diagnostic design are ongoing to ensure that it can take an abundance of data in coming DIII-D experiments. Analysis tools are also being developed to assist in interpretation of the LLAMA data, with the objective of inferring full ionization profiles in the main chamber. This will provide more routine empirical constraints on main chamber particle fluxes, which will be a boon to studies of pedestal and SOL transport in FY20 and beyond.

1.4 Conclusions

In order to further our understanding of how the edge density pedestal is determined in tokamaks, it is critical to close the loop on the edge ionization source. This has motivated improved experimental characterization of main chamber neutral density and ionization profiles. Such measurements provide both the means to directly evaluate particle fluxes and transport coefficients, but also provide valuable constraints on models of edge neutral transport. As seen above, instrumentation and interpretation of data have advanced considerably in recent years, with concerted effort supporting

the goals of this JRT.

The ENDD instrument on NSTX was adapted successfully for use on NSTX-U during its initial campaign, allowing observation of well-resolved profiles of Balmer alpha emission from the NSTX-U plasma edge. These measurements were augmented with passive signals obtained from GPI, and the combined data were inverted to produce radial emissivity profiles. This made possible estimation of the upper bound of edge neutral density, under the assumption that all emission is due to electron impact ionization of atomic deuterium. Simulations using DEGAS2 were used to validate the interpretation of these data, and demonstrated that the emission observed inside the separatrix was dominated by electron impact ionization as assumed, while emission in the lower temperature SOL is dominated by molecular contributions. Altogether this validation effort indicates that neutral (both atomic and molecular) density profiles can be obtained reliably from the coupled ENDD/DEGAS2 analysis, while radial ionization profiles inside the separatrix can be directly inferred from the ENDD data. This makes possible the evaluation of neutral penetration during changes in plasma confinement and obtained plasma density.

In recent DIII-D experiments supporting this JRT, filterscopes measuring main chamber Balmer alpha were used to provide an estimate of the edge neutral density during gas fueling scans. Future work will improve the interpretation of the filterscopes through application of calibrated geometric factors to the view chords, and through careful evaluation of the spatial and time dependence of local excitation coefficients. Future investigations of main chamber ionization will be augmented significantly by the recent installation of a LFS/HFS Lyman alpha profile diagnostic. Among these and other diagnostics, a fuller picture of the 2D structure of ionization is expected to emerge, and to provide powerful constraints on models of pedestal fueling.

2 Effects of opacity on pedestal density structure in C-Mod and DIII-D

2.1 Introduction

An important metric to consider when assessing the role of neutrals in determining pedestal structure is the degree to which fueling neutrals are screened in the plasma edge. As devices are built toward more reactor-like conditions, the degree of neutral influence on the edge pedestal may change considerably, as both non-normalized plasma density and machine size increase, reducing the ability of recycling or gas puff neutrals to penetrate the confined plasma and contribute to particle sources on closed flux surfaces. We can parameterize the screening of fueling neutrals using a neutral attenuation coefficient, or *neutral opacity*, η, analogous to the definition of opacity from optics. The neutral opacity is proportional both to local electron density n_e and to a (generic) cross-section for neutral-plasma interaction σ. A neutral population launched at a uniform plasma will have an exponential decay length given by $L_D = 1/\eta = 1/(n_e\sigma)$, or approximately $\propto 1/n_e$, given the relatively weak variation of σ values at temperatures relevant to the plasma boundary. Thus, higher absolute edge density makes plasmas more opaque to neutrals. Additionally an *opaqueness* screening parameter may be defined as $\eta \times \Delta = L_D/\Delta$, where Δ is the approximate boundary region width.

Neutral screening can vary significantly on a single device, and more so when comparing devices with large variation in size and density. For a given toroidal device, the opaqueness will be proportional to $n \times a$, assuming that the boundary region thickness is proportional to minor radius a. Neutral screening and its effects have been examined on Alcator C-Mod and DIII-D.

machine	shot	Ip (MA)	time-average D_2 puff
C-Mod	1160718025	1.0	12 Torr-L/s
C-Mod	1160718024	1.0	132 Torr-L/s
C-Mod	1160718012	1.3	15 Torr-L/s
C-Mod	1160718013	1.3	79 Torr-L/s
C-Mod	1160718023	1.3	143 Torr-L/s
DIII-D	166025	1.3	0 Torr-L/s
DIII-D	166032	1.3	115 Torr-L/s
DIII-D	166033	1.3	145 Torr-L/s
DIII-D	166037	1.3	180 Torr-L/s
DIII-D	175060	1.7	60 Torr-L/s
DIII-D	175046	1.7	110 Torr-L/s
DIII-D	175045	1.7	210 Torr-L/s
DIII-D	175047	1.7	260 Torr-L/s
DIII-D	175061	1.7	360 Torr-L/s

Table 1: Selected C-Mod and DIII-D discharges.

Here we present experimental and modeling results using controlled density variation on DIII-D in 2018 and on C-Mod in 2016, intended to explore the pedestal at variable neutral opacity. The most suitable discharges from these experimental sessions were identified, and the data were vetted and prepared as inputs to SOLPS modeling. Initial analysis and modeling results are discussed below.

2.2 Experimental setup

To test the role of opacity and fueling in determining the pedestal density structure experiments were performed on C-Mod and DIII-D. Experiments were performed in which through changes in plasma current and fueling, the electron density was varied. Considering that both machines have a different minor radius and we obtained a spread in the line-averaged density, we were able to scan a variety of *opaqueness*.

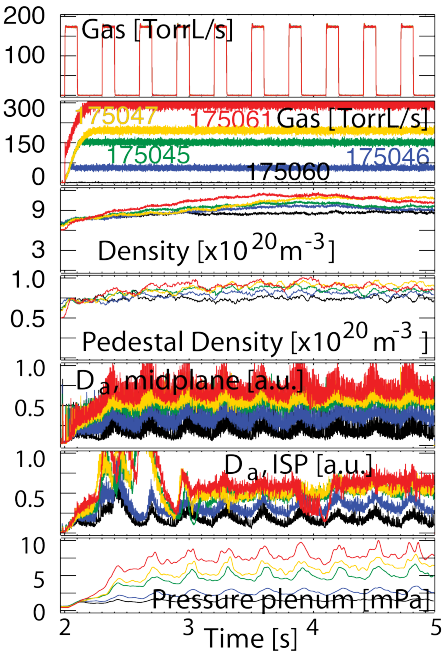

Figure 18: *Time-evolution of the gas puff modulation, gas fueling, line-averaged and pedestal density, midplane and inner strike point D_α and pressure under the shelf for opacity/fueling-scan in DIII-D H-mode plasmas.*

DIII-D H-mode experiments on DIII-D were conducted to investigate the role of ionization in determining the electron density pedestal structure. To reduce the ionization of neutrals inside the pedestal, we increased the SOL density using a gas puff. Higher electron densities are inversely proportional to the ionization rate for a given temperature, so increasing the Scrape-Off Layer density is the best way to increase the opacity to neutrals. These experiments were performed at I_p of 1.3 MA and 1.7 MA with $B_T = 2 - 2.1\ T$, resulting in a $q_{95} \sim 3.7$ (low I_p) and ~ 3.0 (high I_p). The plasmas are heated using $5 - 6\ MW$ (low I_p) $10 - 12\ MW$ (high I_p) of Neutral Beam Injection (NBI), leading to discharges with a $\beta_N \sim 1.8 - 2.2$ (high I_p) and $\sim 1.3 - 1.8$ (low I_p). The pedestal collisionality was high ($\nu^* \sim 2 - 4$, for high I_p and $\nu^* \sim 1 - 5$, for low I_p), since we were operating at high electron density, with pedestal electron densities ranging from $n_e \sim 0.75 - 1.0 \times 10^{20}\ m^{-3}$ (high I_p, as shown in Fig. 18) and $n_e \sim 0.4 - 0.8 \times 10^{20}\ m^{-3}$ (low I_p). The low I_p discharges are similar to the open divertor discharges in section 4 on the effects of the divertor geometry upon the pedestal structure.

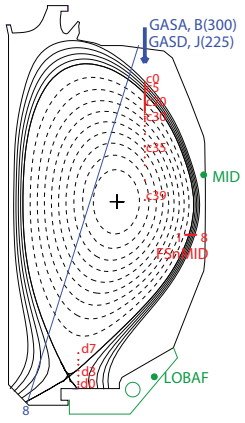

Figure 19: *Plasma shape and location of main diagnostic measurements for the DIII-D experiments.*

For both the high and low I_p discharges, an additional D_2 gas puff raises the SOL and pedestal densities even further, to increase the opacity. For the high I_p discharge, n_e increases as a result of an increase in fueling using 0 to 300 $TorrL/s$ main chamber gas puffing from $2000 - 5000\ ms$. For the low I_p discharges, the gas puff increase from 0 to 180 $TorrL/s$. This increase in fueling from discharge to discharge did not affect the main chamber neutral pressure for the high I_p discharge, but it resulted in a large increase in the pressure under the lower divertor shelf, which has a smaller volume than main chamber. For the low I_p discharges, the pressure valves were not calibrated and operational for that campaign. The experimental shape of the discharges was such that we had good diagnostic coverage to investigate the changes in pedestal structure as well as changes in fueling and divertor conditions, see figure 19.

Additionally, using a different gas valve, we added a 3 Hz perturbative gas puff in order to measure the electron density response to this perturbation, as well as the response of 1D and 2D ionization profiles using filterscopes and fast cameras using D_α and D_β filters. The response of

the electron density, as well as the emissivity from the filterscopes and the pressure changes in the pump plenum, can give us more information on the role of fueling versus transport, see section 1.

As shown in the time traces for DIII-D in Fig. 18, the increase in gas puffing results in an increase in the line-averaged density as well as the pedestal density. This is not just limited to the high I_p plasmas, shown in Fig. 18, but is also observed in the low I_p discharges. The natural electron density for the higher I_p discharge, without additional fueling is 75% higher than for the low I_p discharge. With additional fueling of 145 $TorrL/s$, the electron density increases to similar values observed in the high I_p discharge, without additional fueling. For higher fueling levels for the low as well as the high I_p discharges, there is a similar increase in the SOL as well as the pedestal density, as shown in the profiles of Fig. 20, which are snapshots taken during these discharges. We observe that for gas puffs of 150 $TorrL/s$ and higher for the high I_p discharges, a density shoulder develops in the near SOL, while the outer divertor starts to detach. Carralero et al. [16] show that shoulder formation is often observed when the outer divertor detaches and is linked to an increase in turbulent transport in the near SOL as well as an increase in opacity. As such, we can assume that observed shoulder formation in these DIII-D H-mode plasmas will affect the ionization profile and potentially also particle transport. A similar observation is also made for the low I_p discharges, while the average SOL density remains lower than for the high I_p discharges.

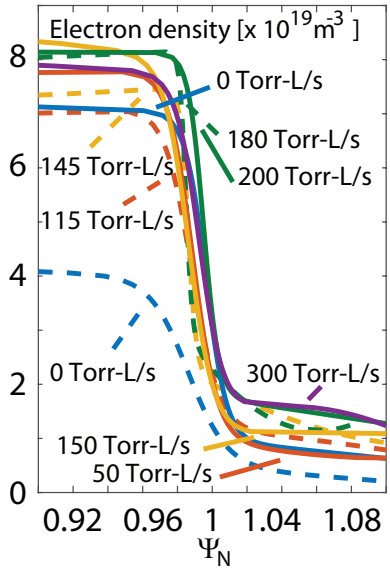

Figure 20: *Electron density profile tanh fits for low (dashed lines) and high (solid lines) current and various fueling levels taken in the* $80-99\%$ *of the ELM cycle on DIII-D.*

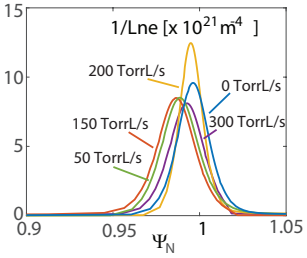

Figure 21: *Change in pedestal density structure based on the tanh inter-ELM fits for increased levels of gas fueling and thus increased opacity.*

While the increase in SOL density saturates and is linked to the formation of a density shoulder, the pedestal density keeps increasing. This increase is seen in the pedestal density waveforms of as well as in pedestal profiles averaged over 3 seconds, as shown in [64]. Only at the highest gas puffing rate of 300 $TorrL/s$, the increase in the pedestal density seems to saturate. In order to better understand how the pedestal structure is affected, not just the height, we calculate $-\nabla n_e$, shown in figure 21. With the exception of the discharge with 200 $TorrL/s$ gas puffing, all the tanh fits show a shift of the peak density gradient inward, a reduction in the maximum gradient and a slight broadening of the pedestal density structure. Prior results from AUG, DIII-D and JET observed a shift outward of the electron density profile into the SOL, with respect to the electron temperature profile [8, 23, 92]. For these earlier results, the shift was explained by an increase in fueling and ionization. However, none of the experiments in these papers were performed at very high absolute opacity, counter to the DIII-D experiments discussed in this section. However, opacity by itself cannot just explain why the density profiles shift inward. The high-opacity C-Mod discharges, which are discussed in this Joint Research Target, all show a significant portion of the pedestal density structure is located in the Scrape-Off Layer.

In DIII-D all the external fueling is through the NBI and the gas valves and in these experiments

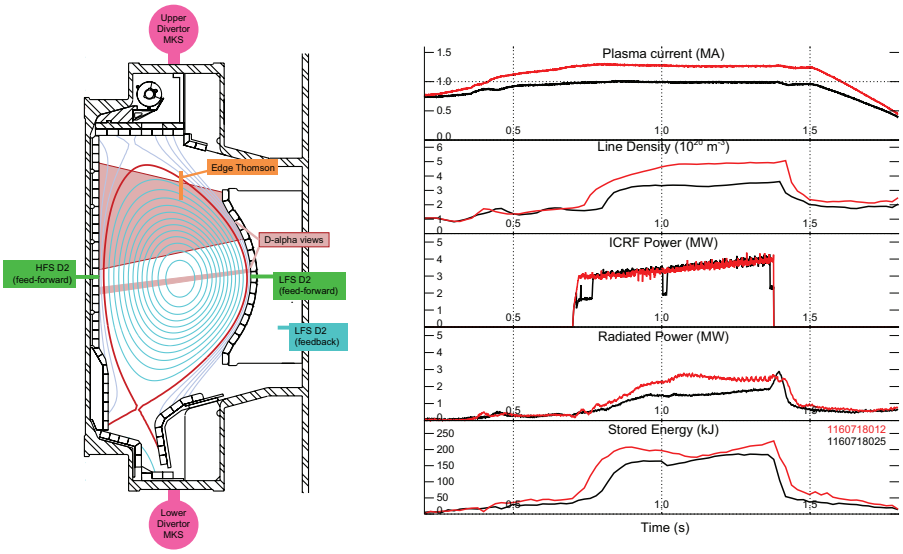

Figure 22: *(a) Typical magnetic equilibrium from the C-Mod experiment to raise neutral opaqueness in H-mode. The equilibrium is near double null with the primary x-point aligned with the ion ∇B drift direction. (b) Time traces from two point I_p scan: plasma current, line-averaged density, ICRF power, bulk radiated power, and plasma stored energy.*

only the lower cryo-pump was Helium cold to provide the exhaust. The maximum amount of fueling is close to 500 $TorrL/s$ where the maximum steady-state gas contribution is 300 $TorrL/s$, as shown in 18. The other $\sim$ 200 $TorrL/s$ comes from a 3 Hz170 $TorrL/s$ gas puff modulation and the steady-state NBI core fueling of about $\sim$ 28 $TorrL/s$. We observe that when the fueling is increased from $0-300$ $TorrL/s$ the pressure in the pump plenum increases linearly with respect to the increase in fueling levels. Based on simple particle balance, only a small fraction of the added fuel actually contributes to increase in the vessel inventory. Of this fraction, a small part contributes to the increase in pedestal and core plasma density, while the rest is attributed to wall loading. Only part of this term can really be linked to wall loading, the other part is due to an increase in the SOL electron density.

C-Mod Alcator C-Mod is a compact high field tokamak ($R = 0.68$m, $B_T \leq 8$T) that completed its last campaign in 2016. Since for given shaping parameters and safety factor, the obtainable density in a tokamak scales with B/R, C-Mod is an ideal device for obtaining high values of neutral opaqueness, which we can parameterize globally according to the product of plasma density and minor radius, $n \times a$. C-Mod routinely reached H-mode densities that pushed it into an ITER-relevant pedestal fueling condition, whereby recycling or puffed neutrals undergo numerous interactions prior to entering the confined plasma zone. Furthermore, edge neutral ionization is the only particle source for the plasma, since auxiliary heating on C-Mod was exclusively RF based, and introduced no core particle source. Significant experimental evidence exists from C-Mod demonstrating insensitivity of density pedestal gradients, and pedestal heights, to gas puffing, particularly at increased plasma current [39, 36].

The pedestal and boundary research program on C-Mod long held a goal of maximizing neutral opaqueness at ITER values of toroidal and poloidal field, in order to get as close to an ITER match as possible. This achievement was challenging because the typical C-Mod high performance regime, the enhanced D-alpha (EDA) H-mode, is favored by operating with $q_{95} > 4$, which typically

requires I_p of about 1MA or less. Taking the next step to raise I_p to 1.3–1.4MA and B_T to 5.4–5.7T, required discharge development which was completed in 2016. The final set of high density H-mode experiments on C-Mod optimized the discharges to maintain both high auxiliary power absorption (3–5MW) and tolerable radiated power fraction in a near double null (DN) equilibrium. An example of the magnetic equilibrium for these experiments with an overlay of the diagnostics used is shown in Fig. 22a. This resulted in line densities in excess of $5 \times 10^{20}\mathrm{m}^{-3}$. Figure 22b shows time traces from two discharges from a single run day, demonstrating the large impact of raising the plasma current on the attained density.

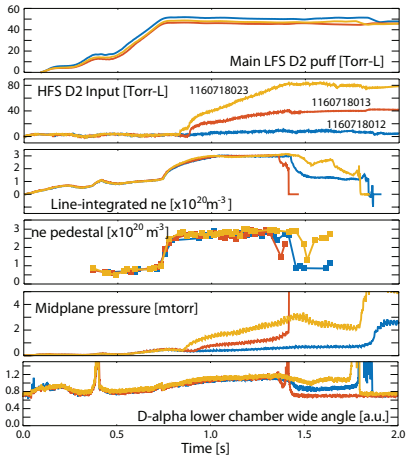

Figure 23: *Time traces from three point gas puff scan in which the HFS gas puff into an established H-mode was varied: integrated puff from LFS, integrated puff from HFS, line-integrated density, fitted density pedestal, midplane neutral pressure and main chamber D-alpha light.*

The H-modes remained in the EDA regime and have no edge-localized modes. Instead a quasi-coherent mode regulates the pedestal and near-SOL transport. Though H-factors are modest (0.8–1.0), these discharges demonstrate stationary confinement of plasma pressure ranging from 0.1 to 0.2MPa [38] Normalized pressure is given by $\beta_N \sim 1.8$. The pedestal collisionality is moderately high ($\nu^*_{\mathrm{ped}} \sim 2$–$4$) as we are operating at high pedestal density and with pedestal temperature well below 1keV, see figure 22b.

Discharges in this experiment were run with gas puffing under feedback, which effectively regulates the density in L-mode. The density rise following the L-H transition exceeds significantly the density demand, causing the feedback puff to go to zero. Therefore the typical H-mode (*e.g* in Fig. 22b) is fueled only from neutral recycling from plasma facing components. As noted above, no core particle source was present. After establishing the baseline H-modes at distinct values of plasma current, supplemental D_2 puffing was applied, using a capillary located on the high field side (HFS) as well as the low field side (LFS) of the tokamak, see Fig. 22a. This puffing strategy into a near double null (DN) equilibrium configuration was chosen in order to optimize the pedestal fueling, while mitigating the build up in low field side (LFS) neutral pressure, which tends to cause ICRF power to drop out, see figure 23.

By changing the gas pressure in the feed-forward puff plenum, the total injection rate into H-mode was scanned at 3 values for the high I_p discharge and at 2 values for the low I_p discharge. The higher current discharge from Fig. 22b is shown again in Fig. 23 along with two similar discharges with additional D_2 fueling at 79 and 143 $Torr - L/s$. The increase in fueling does not have a large effect on the line integrated or pedestal density, nor does the D_α increase in the lower chamber. The only substantial increase is in the mid plane pressure, see Fig. 23.

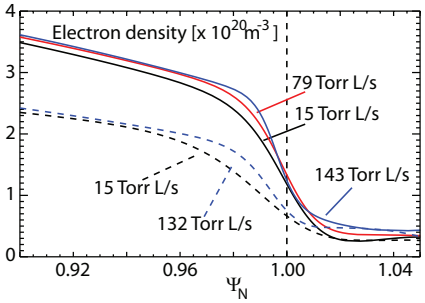

Figure 24: *Tanh fit around 1200 ms for the discharges shown in figure 23. Here the dashed lines are the discharges performed at $I_p = 1.0\ MA$ and the solid lines are the discharges at $I_p = 1.3\ MA$*

In C-Mod the increase in the electron density is much more modest for the low and high I_p discharge at any radial location as measured with the Thomson scattering system and fitted by a tanh curve, as shown in Fig. 24), when compared to the increase in DIII-D, see Fig. 20. The increase in gas puff levels has only a modest effect on the electron density profiles and

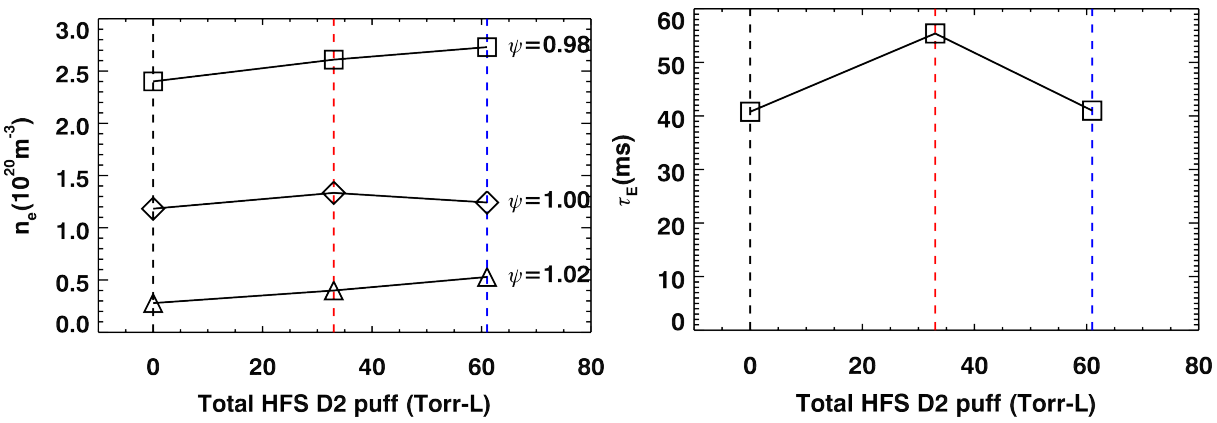

Figure 25: *(a) Response of electron density to HFS D_2 puffing at three positions in the profile: near the pedestal top ($\psi_n = 0.98$), at the separatrix ($\psi_n = 1.00$) and in the SOL ($\psi_n = 1.02$) (b) Confinement time in gas puff scan*

only for the highest puff rate do we observe a small increase in the averaged (from $1.1. - 1.3$ s) overall SOL and pedestal density at both low and high I_p. The separatrix location was determined based on the electron temperature and fixed at 80 eV and this results in density at the separatrix that does not change with additional fueling, but increases with higher plasma current, see Fig. 24. As on DIII-D, the SOL density on C-Mod could be increased approximately a factor of 2 using the supplemental gas puff. However, based on the higher SOL densities ($n_{e_{sep}} = 3 \times 10^{20}$ versus $n_{e_{sep}} = 0.3 \times 10^{20}$) in C-Mod the opacity is already about a factor 7 higher than in DIII-D and nearly reaches the opacity expected in ITER.

2.3 Experimental changes in Pedestal structure and transport

Prior research looking into the role of fueling and pedestal structure has shown that in current machines, the effects of fueling upon the pedestal density structure cannot be ignored [103, 31, 28, 44, 78]. However, as we can already observe when comparing the effect of increased fueling on C-Mod and DIII-D using similarly sized gas puffs, due to different levels of opaqueness and transport conditions, the effects are not identical. Eventually, in a machine like ITER, all fueling inside the separatrix through ionisation of recycled neutrals or additional gas puffing will be reduced to negligible levels and the pedestal density structure will be purely determined by transport effects.

DIII-D As preparation for the SOLPS modeling we performed ONETWO [75] simulations using the ELM-filtered tanh fits for the pedestal. We restricted the data to the 80-99% of the ELM cycle using the Thomson Scattering system for the electrons and the Charge Exchange Recombination (CER) for the ions. Using the information from the neutral beam injection for the various core sources, ONETWO, a 1.5D transport code calculates the fluxes and the transport coefficients, using a pure diffusive model. Prior research for H-mode experiments at much lower opacity and power, with pedestal densities of $\sim 3 \times 10^{19}$ m^{-3} has shown good agreement between ONETWO and an older SOLPS version using purely diffusive transport coefficients [74]. ONETWO should offer a good starting point to find the transport coefficients, based on a purely diffusive model, to match the experimental observations.

C-Mod We are beginning to examine the impact on confinement from the feed-forward gas puff

in this data set. The moderate puff rate has a measurable impact on the density pedestal (compare the red curve to the black in Fig. 24), increasing its magnitude and shifting it outward in minor radius. In many prior studies this was shown to degrade confinement, but in this case the plasma temperature and stored energy increase. Doubling the gas puff (blue curve) further increases the edge density, and this is accompanied by confinement degradation. This is suggestive that we scanned the optimum puff rate in this configuration, and that it is near the saturation condition for the density pedestal.

The effect of the additional gas puff on the global and pedestal density is subtle, although a clear impact is seen on the midplane neutral pressure, measured in a LFS port. Fits of pedestal profiles from Thomson scattering using a modified tanh function in Fig. 24 correspond to the discharges in Fig. 23, and show a significant increase in plasma density on open field lines with increased puffing. This 'filling up' of the scrape-off-layer was noted in prior gas puffing experiments [39], along with a shift of the density pedestal top towards the separatrix. Notably, in this configuration, which is at higher I_p and higher power than previous puffing studies, previous observations of separatrix density increasing and confinement loss [36, 37] are not automatically reproduced. Instead, as Fig. 25a illustrates, the separatrix density is changed very little as the SOL and pedestal density rise.

There is furthermore an increase in confinement in response to the introduction of some HFS puffing, followed by a rollover at higher puff rate, as shown in Fig. 25b. The causes for this effect are under investigation.

2.4 SOLPS-ITER Modeling

The SOLPS-ITER modeling has multiple goals. First, it is to verify that these experiments in which we increased the electron density, really result in an increase in '*opaqueness*' and whether it has an impact on for example the poloidal distribution of the neutrals. Second, SOLPS-ITER often assumes a poloidally symmetric distribution of the radial transport, however, in reality transport is much larger on the LFS than the HFS [47, 44]. This asymmetry in the transport has resulted in differences in how the pedestal density scales on the HFS versus the LFS. On the HFS, previous results found that the density pedestal structure is dominated by fueling, whereas on the LFS the density pedestal structure is more dominated by transport [44]. In this section we investigate how the poloidal distribution of the neutral density profiles is affected by altering the transport from radially uniform to ballooning on the LFS using an ad-hoc model. Finally, on DIII-D and C-Mod part of the density scan was performed using an additional gas puff. We use SOLPS-ITER to look at how the same gas puff in SOLPS-ITER, as used in the experiment, affects the electron density from the SOL up to the top of the pedestal.

SOLPS-ITER setup and physics SOLPS-ITER [102, 11] is an edge modeling package consisting of B2 [12], a 2D fluid code, using a 2-fluid Braginskii model for the plasma, coupled to EIRENE [79], a Monte-Carlo code, tracking the neutrals. For both DIII-D and C-Mod, the EIRENE grid extended all the way to the vessel walls and the B2 grid extended about 5% into the SOL for C-Mod and 10% for DIII-D. The radial extent of the grid for C-Mod was limited by the near double null geometry and for simplicity of the computational setup.

All simulations used flux boundary conditions for the core boundary, where the fluxes were determined from experimental input. The only exception here, is the particle flux for C-Mod. In order for the simulations to converge and reach electron density values similar to those measured at the plasma edge, we had to impose a particle flux of $\Gamma_p = 1.2 \times 10^{21}\ 1/m^2 s$ for high I_p and

$\Gamma_p = 7.5 \times 10^{20}\ 1/m^2 s$ for low I_p. In DIII-D, we were able to use a particle flux similar to the one give by the NBI particle flux calculated by ONETWO and set at $\Gamma_p = 2.4 \times 10^{19}\ 1/m^2 s$. The heat fluxes were for all cases similar to those based on power balance and experimental conditions. At the outer SOL, a simple exponential decay value was set, to allow the plasma profiles to relax to their preferred values.

We set the recycling on all wall elements to be 1 and only reduced the values to 0.99 at the target plates. These values are typical for metallic walls which have a very low absorption rate. However, carbon walls can absorb deuterium in short pulse machines [69] and thus recycling is often set to 0.99 for the typical DIII-D discharges at much lower density. In these experiments, however due to the high gas puff rates and warm upper cryo-pumps, the walls eventually saturated during the day. This was observed by tracking the neutral pressure in the main vessel during these experiments. At the moment when the high opacity discharges were performed, the pressure in the main chamber did not vary and was even unaffected by increase gas puffing. All simulations are performed without drifts in order to get a first estimate and avoid lengthy and time consuming computations that go beyond the time frame of the JRT.

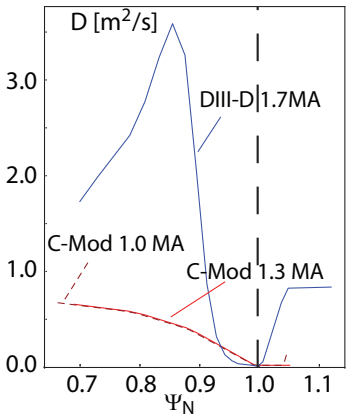

Figure 26: *Extracted diffusion coefficients using SOLPS-ITER to match experimental density profiles from the 1.7 MA DIII-D discharge (blue) and the 1.0 (dashed) and 1.3 (solid) MA C-Mod discharges (red).*

For DIII-D, we start from the transport coefficients calculated by ONETWO and adapt them so that the simulations 'match' the experimental density and temperature profiles (not shown for brevity in this report). We find that the transport coefficients needed to match the experimental profiles are very similar those calculated by ONETWO. For C-Mod, there are no ONETWO simulations to which we can compare the results. We find that both for the low and high I_p discharge on C-Mod the transport coefficients were very similar and the much higher density is achieved in the simulation with the increase in core particle flux, see Fig. 26.

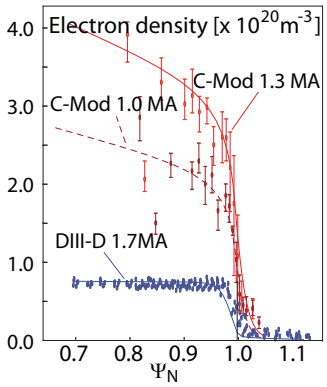

Figure 27: *SOLPS-ITER simulations (lines) using transport coefficients from figure 26 and experimental electron density profiles for the 1.7 MA DIII-D discharge (blue) and the 1.0 (dashed) and 1.3 (solid) MA C-Mod discharges (red).*

Opacity impact on neutral density Using the boundary conditions highlighted above, as well as the transport coefficients from figure 26, we find good agreement with experimentally measured electron density, see figure 27 and temperature profiles. SOLPS-ITER calculates the neutral interactions self-consistently and we can now compare the neutral density distributions for all 3 simulations. From the three contour maps, see Fig. 28, it is apparent that, on average, the neutral densities for the low current discharge are higher inside the separatrix than in the high current discharge.

The SOLPS-ITER simulations indicate, similar to the simplistic approximation for opacity $n \times a$, that the high I_p discharge in C-Mod, with higher electron density is more opaque to neutrals than the lower I_p C-Mod discharge was well as the DIII-D discharge. The difference is especially noticeable for C-Mod, where both discharges have similar neutral densities in the SOL, but the lower opacity discharge has higher neutral concentrations much deeper inside the plasma, see figure 28. Another interesting observation is that on first sight, the neutrals penetrate much deeper (in Ψ_N space) in the

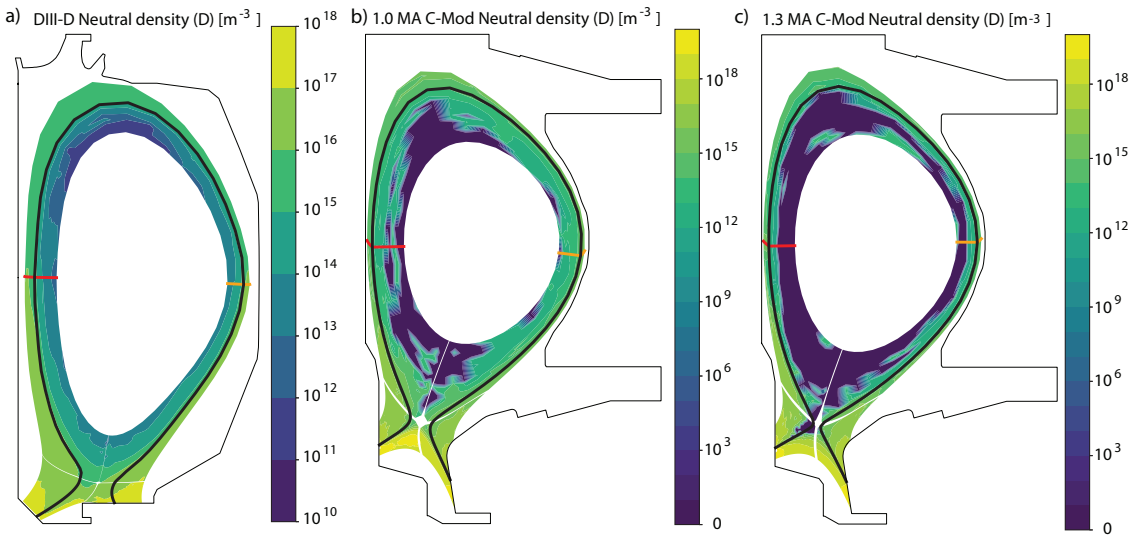

Figure 28: *2D contour plots of the neutral density in a) DIII-D, b) C-Mod at 1.0 MA and c) C-Mod at 1.3 MA. The discharges are arranged from low to high opacity.*

plasma on the low field side and not at the X-point. While the neutral mean free path might be longer close to the X-point, the flux surfaces are further apart due to flux expansion.

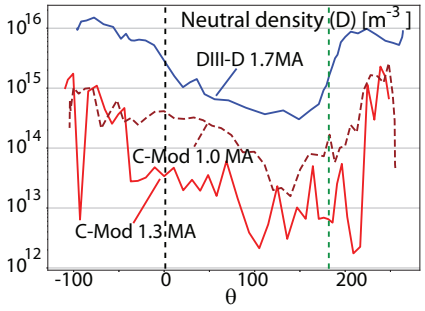

Figure 29: *Poloidal cut of the neutral density just inside the separatrix for the 1.7 MA DIII-D discharge (blue) and the 1.0 (dashed) and 1.3 (solid) MA C-Mod discharges (red). The X-point is where the poloidal angle starts (close to* $-110°$*) and ends (close to* $250°$*), the dashed lines are the LFS (black) and HFS (green) mid-plane locations.*

To investigate the poloidal distribution in more detail, we take look at the neutral density just inside the separatrix plotted versus the poloidal angle, see figure 29. We are not able to validate the calculated neutral density values directly against experimental data. However we note that the value calculated at the midplane on C-Mod is approximately 2 orders of magnitude below what has been inferred experimentally in similar discharges [39]. Instead of focusing on the absolute values of neutral density, we consider the poloidal variation. For the C-Mod discharges, the neutral densities are similar close to the X-point, but the highest opacity discharge has much lower (about an order of magnitude) densities from just below the LFS mid-plane over the crown to the HFS mid-plane (about $-30°$ to $220°$ in figure 29).

We can also observe that for each of the discharges and for each level of opacity just inside the separatrix the neutral density is about a factor of 10 higher near the X-point than at the LFS midplane. If we consider main chamber fueling, mostly occurring from just below the LFS midplane to the HFS midplane (about $-10°$ to $180°$), we can observe that for DIII-D, the densities are fairly low, compared to higher values at the X-point (close to $-100°$) as well as $\pm 90°$ away from the X-point. On C-Mod, especially for the 1.0 MA discharge, the decrease in neutral density from the X-point to the midplane on the LFS is much more rapid and remains at a constant neutral density, until we reach the crown of the plasma and cross over to the HFS. The neutral density results for the 1.3 MA discharge are very noisy, especially around the X-point. The different poloidal distribution of the neutrals between the 2 machines close to the separatrix illustrates the different perception

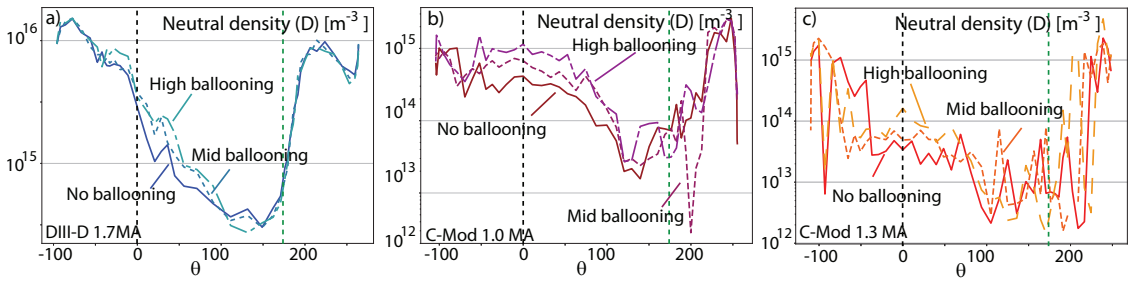

Figure 30: *Poloidal cut of the neutral density just inside the separatrix at various levels of ballooning transport in a) DIII-D, b) C-Mod at 1.0 MA and c) C-Mod at 1.3 MA. The discharges are arranged from low to high opacity. The X-point is where the poloidal angle starts (close to* $-110°$*) and ends (close to* $250°$*), the dashed lines are the LFS (black) and HFS (green) mid-plane locations.*

that on DIII-D most of the fueling occurs close to the X-point, whereas on C-Mod, the poloidal distribution of the neutrals is more uniform with the exception of near the plasma top.

Impact of ballooning-like transport

In the SOLPS-ITER simulations, we have assumed so far the radial transport is uniform poloidally, which is the most common approach. However, since transport is highly ballooning and also since prior research by Kirk et al. [44] showed that this could affect how the pedestal responds to fueling on the HFS versus LFS, we performed an artificial ballooning scan for all 3 discharges. The scan was performed in such a way to make sure that the total particle flux remained the same, just that the poloidal distribution was altered. This means that all of the SOLPS-ITER profiles of the electron density and temperature remain very similar to those without the ballooning transport effect. So the change in transport only changed the poloidal distribution of the radial flux. This redistribution of the radial flux poloidally, surprisingly affects the neutral density inside the separatrix, see figure 30. For these simulations the highest ratio of $D_{LFS}/D_{HFS} \sim 4$ for all 3 discharges, and the middle value is at $D_{LFS}/D_{HFS} \sim 2$.

For all of the modeled discharges we observe an increase in the neutral density just inside the separatrix on the LFS midplane and upward towards the crown of the plasma. There are no significant changes in the neutral density on the HFS or the X-point. The effect is the least pronounced at the highest opacity and this can be attributed to the low penetration level of neutrals inside the separatrix in the first place. The effect is much more pronounced for the lower opacity discharges in C-Mod and DIII-D. The chosen ballooning values are much lower than what has been observed in L-mode plasmas using probe measurements of turbulence on the HFS versus the LFS, where often on the HFS the turbulence levels were close to the noise level of the probe [47]. The measured turbulence levels were a factor 10-100 higher on the LFS versus the HFS in L-mode C-Mod discharges. These initial simulations show that the assumption of uniform transport can strongly affect the validity of self-consistent simulations and impact the validation of these models.

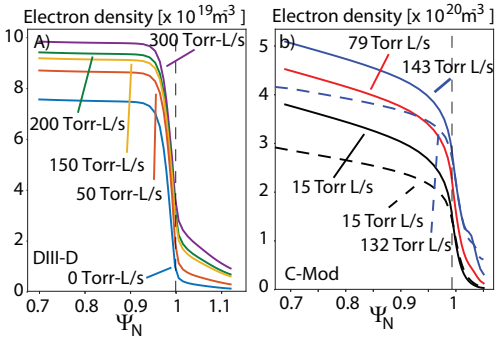

Figure 31: *Midplane electron density profile from SOLPS-ITER gas puff simulations for a) DIII-D and b) 1.0 MA (dashed) and 1.3 MA (solid) C-Mod discharges.*

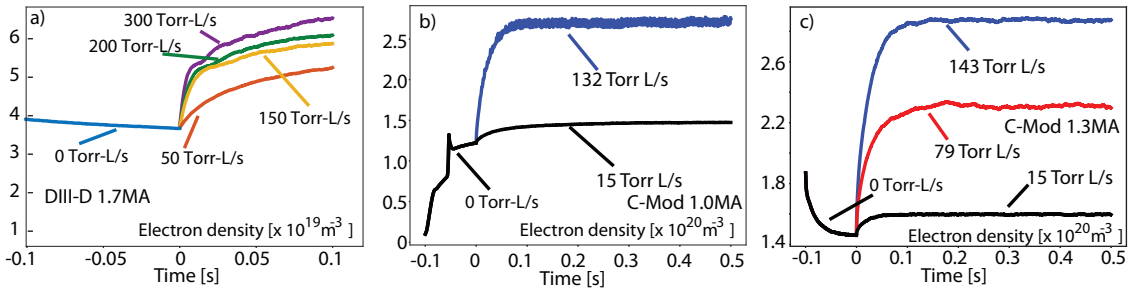

Figure 32: *Time evolution of the midplane separatrix electron density at various levels of injected gas in a) DIII-D, b) C-Mod at 1.0 MA and c) C-Mod at 1.3 MA. The discharges are arranged from low to high opacity. The gas puff starts at time* 0 *and before* $t = 0$ *is the evolution of the original discharge without gas puff to reach an equilibrium.*

Impact of additional gas fueling

In all these experiments additional gas puffing was performed to test the interaction between opaqueness, gas fueling and the pedestal structure. Prior research has linked a higher neutral concentration in the SOL to an outward shift of the electron density profile [8, 23, 92]. The idea being that part of the pedestal density structure is governed by the ionization source directly [31]. The DIII-D results show no such outward shift of the pedestal structure, see figures 20 and 21 and neither does the C-Mod pedestal shift further outward with additional gas fueling, see figure 24. Moreover, the outward shift of the pedestal density structure was accompanied by a decrease in confinement in JET and AUG [23, 92], whereas in C-Mod we are able to increase confinement with the right size puff.

To test the hypothesis that additional fueling, keeping transport the same, would result in an outward shift of the density profile, we use the SOLPS-ITER code and apply various levels of additional gas puffing. The size and the location of the gas puff is determined by the experimental location and amplitude. In figure 31 we show how the electron density changed in the SOLPS-ITER simulations as a result of the additional gas puff. Both in DIII-D and C-Mod we can observe in comparison with the experimental results a strong over prediction in the electron density at each radial location, see figure 24 and 20. In DIII-D, at the highest fueling rate the pedestal remains under $8.0 \times 10^{19}\ m^{-3}$ and in C-Mod the increase in electron density for the 1.3 MA discharge is barely noticeable outside error bars, whereas the SOLPS-ITER simulations show a strong increase overall. It is as if by shifting the SOL electron density up, the whole electron density profile has been lifted. The increase in neutral flux does shift the electron density pedestal outward in the C-Mod discharges, something which is not observed experimentally.

In figure 32 we show how the simulated electron density at the midplane separatrix changes with time as a result of the applied gas puff. We observe that all simulations have reached a new equilibrium and that the SOLPS-ITER simulations indicate a strong increase in the separatrix density, independent of the opacity level. If we focus on the experimental changes in the electron density at the midplane separatrix, we can observe that in the C-Mod experiments, there is no change, while in DIII-D the separatrix density hovers around $4 \times 10^{19}\ m^{-3}$ depending on the exact location of the separatrix. There is no clear increase in the experimental separatrix density and especially not an increase to $6 \times 10^{19}\ m^{-3}$ as shown in the simulations of figure 32.

2.5 Conclusions

Summary In a series of experiments on DIII-D and C-Mod in which the SOL opacity was increased, we observed that neutral penetration was reduced. The reduction in the penetration of neutrals inside the separatrix did not result in a reduction of the pedestal density, nor did we observe a shift outward, which is often observed at lower opacity and performance. The higher the opacity the less effective additional gas puffing became in raising the pedestal density. SOLPS-ITER simulations show that while X-point fueling is an order of magnitude larger than the fueling at the mid plane, this fueling increase can be very localized over a small area, thus allowing main chamber fueling to play a considerable role. We did find that for C-Mod the SOLPS-ITER model predicts neutral densities about 2 orders of magnitude lower than observed in prior experiments and as a consequence a large particle flux had to be implemented at the core boundary to prevent the electron density from collapsing. On DIII-D, the neutral densities were in agreement with prior models and observations.

Limitations of the SOLPS-ITER simulations The neutral density calculations from SOLPS-ITER for DIII-D are close to prior modeling results as well as prior experimental estimates using the filterscope system [20, 88, 74]. However we note that the value calculated at the midplane on C-Mod is approximately 2 orders of magnitude below what has been inferred experimentally in similar discharges [39]. This is closely linked to the need to have an outward particle flux at the core boundary condition in SOLPS-ITER, to increase the total radial particle flux across the separatrix. In DIII-D we found that small changes in recycling can strongly affect the need for such a flux and the neutral density inside the separatrix, however for C-Mod, all recycling values are already set to 1. While none of the simulations had any drifts, the drifts by themselves cannot increase the 2 orders of magnitude discrepancy between current simulations and prior measurements.

One option to increase the neutral density inside the separatrix for C-Mod is to increase the energy of the neutrals. There is experimental evidence that in metallic wall machines, the energy of the reflected neutrals is higher than in Carbon machines [104]. The higher energy level would result in a deeper penetration depth and the neutrals would not get trapped in the far SOL. Moreover, SOLPS-ITER has mostly been tested in low-opacity discharges and it could well be that the high opacity discharges put a burden on the neutral dynamics simulated by the Monte-Carlo code. This would explain why integrated modeling simulations of ITER using SOLPS-ITER result in very low electron density profiles, without an artificial large core particle flux [81]. This shows yet again the need for developing more capabilities to measure the neutral density at various locations in the plasma and provide direct data for validation of plasma edge codes, such as SOLPS-ITER.

Experimental changes in Opacity In current machines, increasing the Scrape-Off Layer density affects more than just the neutral opacity. Higher SOL densities also affect the divertor conditions and are linked to the onset of detachment in the outer divertor [54]. These changes in divertor conditions in turn affect the SOL and pedestal conditions [98, 105, 16]. For example, the detachment of the outer divertor will affect the parallel conductivity, which then in turn alters the filamentary and fluctuations behavior in the SOL. The increase in fluctuations is linked to an increase in radial turbulent transport and the formation of a flat spot in the near SOL density profile, also called a shoulder. The shoulder formation itself is very effective at increasing opacity and pushing the ionization front further out into the SOL. All these changes cannot be easily separated and further analysis and modeling is needed to help disentangle the transport from the fueling effects.

Consequences for ITER We will restrict ourselves here to discussing the potential impact of an opaque SOL on ITER, based on the experimental results presented in this section. In this section we showed that an increase in edge opacity does not eliminate the existence of a high performing pedestal structure. We can calculate the inverse mean free path of the neutrals for these experiments and compare them to ITER. The inverse mean free path for neutrals $1/\Delta c_x$ depends strongly on the electron density n_e and less on the electron temperature, T_e. We can use this as a proxy for opacity: $1/\Delta C_x = \frac{1}{1.91\times10^{17}} \frac{n_{sep}}{T_{esep}^{0.425}}$. In ITER $1/\Delta c_x \sim 220$. Using $T_{e_{sep}} \sim 200eV$ and $ne_{sep} = 4 \times 10^{20}$, the highest values in DIII-D in these opacity experiments was 22, while in C-Mod we achieved 162. For ITER the inverse neutral mean free path is close to 220, based on published SOLPS predictions. As such, the C-Mod results have an SOL that will resemble ITER's SOL closely when it comes to opacity. Counter to prior ITER simulations using SOLPS-ITER, where the density pedestal structure has disappeared [81], these C-Mod experiments still have a clear pedestal structure in the electron density. More SOLPS-ITER simulations will be necessary to assess how much of the pedestal is determined by fueling, but current work on DIII-D and C-Mod indicates that as we go to high opacity and neutral fueling in the pedestal decreases, the pedestal structure persists.

Future work There is a strong need to further our understanding of particle transport in the pedestal. From these experiments it is clear that ionization alone cannot determine the pedestal structure. Ionization plays a dominant role in most of our current day experiments, but when we increase the opacity in these experiments and thus limit the effects of ionization, we still observe a pedestal structure. A validation of edge modeling codes that capture the neutral dynamics is necessary before we couple these components to self-consistent transport simulations. Techniques to measure the transport changes directly using modulated gas puffs will benefit strongly from a much better prediction of the edge fueling source in order to test the separate transport components [65].

3 Localization of Fueling Source on DIII-D, NSTX

3.1 Introduction

Present-day magnetically confined fusion devices usually use gas injection at the plasma edge as the primary means of fueling. Energetic beam injection, cryogenic pellet injection and supersonic molecular beams are also used in some experiments. As noted in the previous section on opaque SOL, gas fueling at the plasma edge is not expected to be effective in ITER and pellet-injection is planned as the primary fueling technique on ITER [40].

Gas puffing and recycling fueling efficiency have been the subject of investigation since the first limiter and divertor tokamaks [29, 25, 24, 30, 106, 62]. The fueling efficiency was commonly defined as $\eta = (dN_i/dt)\ \ \Gamma_{gas}^{-1}$, where N_i is the confined particle inventory, and Γ_{gas} is the gas injection rate, i.e., the probability that an injected neutral atom (one half a molecule) crosses the separatrix and becomes an ion in the confined region. Typical low field side (outer) gas injection FE values are in the range 0.01 - 0.2 in divertor configurations, and much higher in limiter configurations [29]. It is desirable to reduce the amount of injected neutral gas while increasing the fueling efficiency.

In this section, the aim is to improve our understanding of impact of the localization of the particle source on the pedestal. Experiments on DIII-D have explored this through systematic fueling rate scans in ECH-heated and gas puffed discharges (edge source) and in NBI-heated discharges with pellet injection (core source). New analysis has been performed on NSTX data from H-modes with gas injection at various locations (e.g., low-field side and high-field side conventional gas injectors and a supersonic gas injector). A summary of the findings is described below.

3.2 Variation of radial fuelling location from core to edge

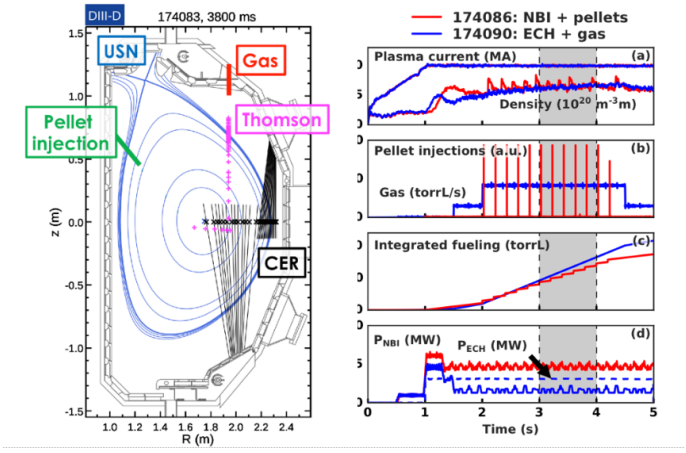

Figure 33: *Left panel: Typical equilibrium with positions of important diagnostics. Right panel: Comparison of waveforms for discharge with NBI + pellets (red) and ECH + gas (blue). a) Plasma current and line-averaged density; b) pellet injection rate or gas fueling rate; c) Integrated fueling; d) injected heating power (ECH or NBI) [70].*

Introduction An experiment was carried out in DIII-D in FY18 to determine the impact of the particle source location on the pedestal structure and the role of a pinch in setting the density pedestal [70]. Understanding what sets the density pedestal is important for predicting core performance and ELM stability. Furthermore, understanding pedestal fueling for next step devices, like ITER, becomes crucial as the SOL will be opaque to neutrals. Exploiting the flexibility of DIII-D, the strategy of this experiment was to vary core vs. SOL fueling schemes via a combination of pellet and NBI fueling (i.e. core) vs. gas puffing (i.e. SOL fueling). The goal of this experiment was to determine if there were measurable changes to

the pedestal profiles due to a change between more core and more edge pedestal fueling.

Experimental Strategy and Setup Because recycling is a dominant fueling source on DIII-D regardless of external fueling actuators, this experiment was performed in the upper closed divertor to reduce the recycling flux. The chosen equilibrium with important diagnostics is shown in Fig. 33. This shape was optimized to achieve good divertor closure as well as provide excellent profile diagnostic coverage of the edge to resolve the pedestal structure. Optimization of strike point position and flux expansion was attempted to maximize particle exhaust. The L-mode wall-loading was minimized by attempting early H-mode transitions to further reduce wall fueling. The two deployed fueling schemes, high field side pellet injection [6] and gas puffing, were employed to vary the particle source location at similar fueling rates. Dedicated scans of fueling rates (10, 20, 30 and 40 Torr-L/s) were performed with each fueling source. All plasma discharges had a plasma current of 1 MA and a toroidal magnetic field of 2 T in the upper single null (USN) configuration with the ion $B \times \nabla B$ drift towards the upper X-point. The upper closed divertor was chosen to achieve better control of residual neutrals via pumping and to reduce the recycling influx from the plasma-wall interaction zone [1, 42, 98]. Pellets were injected from the high-field side to increase penetration depth and densities of a Greenwald fraction of $n_e/n_{GW} \sim 0.4$ are obtained.

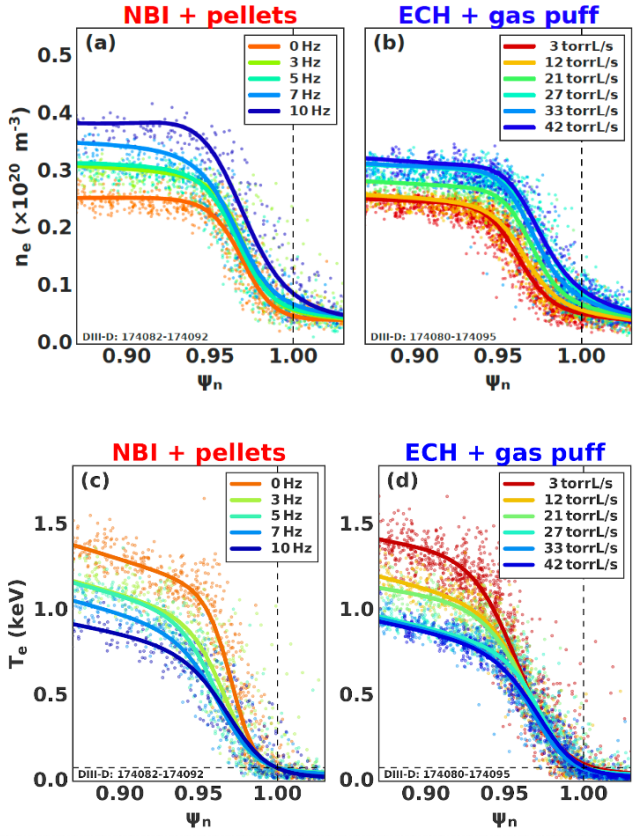

Figure 34: *Pedestal profiles at different particle injection rates. a) Electron density for NBI+pellets; b) electron density for ECH+gas puff; c) electron temperature for NBI+pellets; d) electron temperature for ECH+gas puff [70].*

To obtain the largest difference in fueling, the gas-fueled discharges were dominantly heated by electron cyclotron resonance heating (ECH) to avoid central fueling that occurs with neutral beam injection (NBI), which was applied in the pellet fueled discharges. The right panel of Fig. 33 compares time traces of a pellet- and gas-fueled discharge and indicates the time interval in which the pedestal structure is analyzed (grey shaded area). The two discharges that are compared had the same line-averaged density. Fig. 33a).

Modification of the Pedestal Structure through variation of the source location For the pedestal analysis, the profile data is filtered to remove modulations of the ELM crashes and pellet injection. Only data in the later part of an ELM cycle ($60-98\%$) was used to construct profile fits. Furthermore, only the later period after a pellet injection ($50\%-98\%$ of the time in between pellet injections) was included. During this period the density spike, which is caused by the immediate pellet ablation, has decayed and the line averaged density is almost stationary. The pedestal profiles (n_e,T_e) are fit by modified hyperbolic tangent (mtanh) curves [32] and they were aligned such that $T_e \sim 80\ eV$ at the

separatrix [91].

Fits to the n_e and T_e profiles of the two fueling scans are presented in Figure 34. In the gas-fueled fueling scan, the pedestal density ($n_{e_{ped}}$) increases by a factor of 1.3 over the full range of the fueling scan. In comparison, the pellet-fueled cases show a larger increase (up to a factor of 1.5) in $n_{e_{ped}}$. This suggests that central (pellet) fueling is more efficient than an equivalent rate of edge fueling (gas-puffing). Furthermore, the gas-fueled cases with the highest fueling rates (33 $TorrL/$ and 42 $TorrL/$) show barely any variation of $n_{e_{ped}}$. With both fueling methods, the separatrix density $n_{e_{sep}}$ increases by 30% across the range of applied fueling. Both the width of the density pedestal and the maximum density gradient ($\nabla n_{e_{max}}$) remain roughly constant throughout the fueling scans while the density gradient at the separatrix ($\nabla n_{e_{sep}}$) increases by a factor of 3 as a result of an outward shift of the electron density pedestal profile.

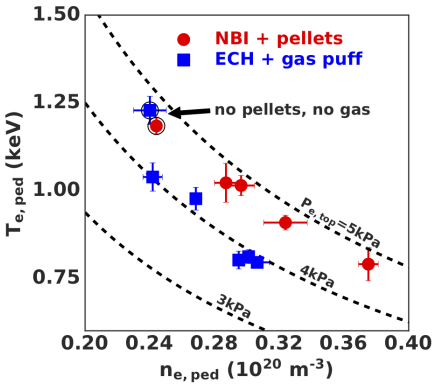

Figure 35: *Pedestal electron temperature vs pedestal electron density for NBI+pellets and ECH+gas puff. The density was increased by a higher fueling rate [70].*

Particularly in the gas-fueled cases, the density pedestal (location of steepest gradient) shifts outwards with respect to the temperature profile as the fueling rate increases. Similar relative shifts of the n_e and T_e profiles across fueling scans have been reported for ASDEX Upgrade [23] and JET [92] and have been previously reported for DIII-D [8]. However this shift is not observed in the high opacity discharges discussed in section 2. The ratio of pedestal to separatrix density ($n_{e_{ped}}/n_{e_{sep}}$) remains roughly constant throughout the gas fueling scan, whereas it increases for higher rates of pellet fueling. This is another indicator that more core fueling has a bigger effect on the n_e at the pedestal top than more edge fueling.

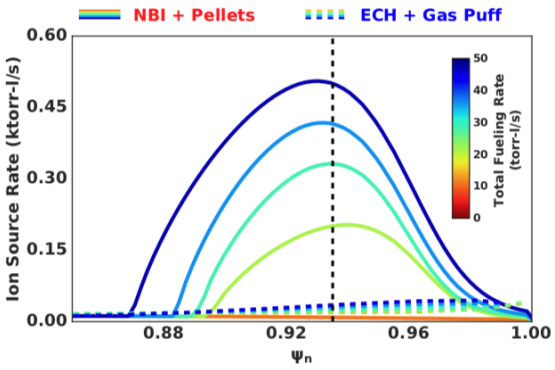

Figure 36: *Local ion source rate profiles for fueling scans. Pellet ablation profiles from PELLET are shown in solid lines, gas ionization profiles from UEDGE are shown in dashed lines. Same-color profiles have similar total fueling rates. Solid lines also include local source from beams. Ion source rates are plotted per ψ_N. Thus, the integral of each curve over entire minor radius, including beams, is equal to the total fueling rate in the confined plasma. The colors of the curves show the total fueling rates [70].*

Figure 35 shows the pedestal electron temperature ($T_{e_{ped}}$) versus the pedestal top electron density ($n_{e_{ped}}$) for both fueling scans. This figure also shows contours of constant pedestal electron pressure ($p_{e_{ped}}$), which is the product of $T_{e_{ped}}$ and $n_{e_{ped}}$. Independently of the applied type of fueling, these data show that the achieved $p_{e_{ped}}$ in each scan remained approximately constant, being about 5 kPa for the case with pellet fueling and 4 kPa for the case with gas puffing. However, when the lowest level of gas puff was introduced, $p_{e_{ped}}$ dropped by more than 10% from the no gas reference. In contrast, throughout the pellet-fueling scan, $p_{e_{ped}}$ remained at the level of the no pellet reference. The observed constant $p_{e_{ped}}$ throughout the fueling scans indicates that the

pedestal stored energy is conserved. The initial 10% drop of $p_{e_{ped}}$ in the gas fueling scan has to be investigated further. The application of ECH can lead to a so-called density pump-out [66, 100]. The density pump-out is related to specific changes in turbulent transport from $\rho \sim 0.6 - 0.9$. Without more detailed turbulent analysis we cannot make a statement as to what is contributing to the changes in the electron density pedestal structure.

Modeling of particle source Neutral fueling profiles have been computed for the discharges in the fueling scans studied here and are shown in Fig. 36. The solid lines show the local fueling source for the cases of pellets plus NBI. The fueling source from the beams is computed with TRANSP [14]. The total fueling rate from the beams is about 10.5 Torr-l/s which is primarily deep in the core; local beam fueling in the pedestal is very small compared to the pellet fueling. The pellet injection profiles are calculated with a standalone ablation model called PELLET [34]. This model computes the ablation rate of each fueling pellet as a function of the distance along the trajectory of the pellet, based on the geometry of the discharge and the experimentally measured density and temperature profiles. Ablation in the SOL is assumed to be negligible and is not included in the model. Within the experimentally obtained temperatures and densities, the computed pellet ablation profile peaks at the pedestal top (indicated by a dotted vertical line in Fig. 36) regardless of the plasma conditions. This confirms that pellets can be expected to deposit neutrals well inside the separatrix and throughout the pedestal and outer plasma region in DIII-D, in this case up to radii of $\psi_N \sim 0.88$.

Figure 36 also shows the 1D ion source profiles in the confined plasma region for the gas-fueled cases (dashed lines), as calculated in the UEDGE code [80]. These profiles were obtained by automatically matching the experimentally measured outer midplane ne, Te and Ti profiles in UEDGE by changing the particle diffusion and the electron and ion heat conduction. Robust matching was done with a new algorithm based on local gradients with a 3% fixed fraction carbon, high recycling plates, standard flux limits turned on and a SOL simulation region that covered approximately 10 times the DIII-D heat flux decay length. The ion source rate was calculated as the neutral gas density multiplied by the ionization rate coefficient, per volume element.

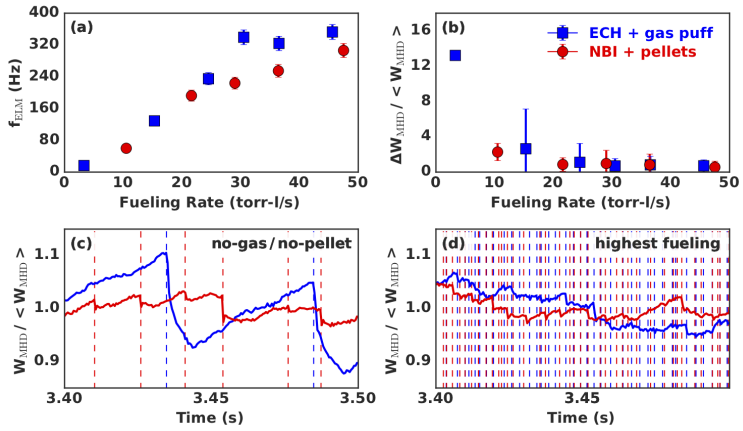

Figure 37: *Characterization of observed ELMs. (a) ELM frequency increases with increased fueling rate. (b) Average size of the ELMs, as determined from $\Delta W_{\rm MHD}$ drops with increasing fueling. (c,d) $W_{\rm MHD}$ normalized to average energy for entire shot $< W_{\rm MHD} >$ as a function of time for select shots. In (c), traces are the no-gas (blue) and no-pellet (red) reference cases. In (d), lines are from highest gas fueled shot (blue) and the highest pellet-fueled shot (red). Dashed lines mark ELM times [70].*

Prior to this experiment, it was expected that core pellets would fuel the pedestal more efficiently than gas puffing. The analysis shown in figure 36 supports this picture, showing that for the same fueling rate, the core pellets provided much more ionization in the pedestal (for $\psi_N \lesssim 0.98 - .99$) than obtained from gas fueling. This higher fueling rate for pellets, coupled with the observed changes in pedestal electron temperature and density profiles, shows that the location of the particle

source affected important details of the pedestal structure.

Characterization of ELM Behavior It is often observed in tokamaks that higher fueling rates modify the ELM characteristics by decreasing the average ELM size and increasing the ELM frequency [53]. This behavior was observed in this experiment. As shown figure 37(a,b), the ELM frequency increased and the ELM energy loss decreased with increasing fueling rate for both pellets and gas. Figure 37(c,d) compares the ELM behavior and energy losses for reference discharges without fueling (Fig. 37c) with highly fueled discharges (Fig. 37d). Each vertical dashed line indicates the occurrence of an ELM, characterized by a spike in the divertor D-alpha radiation. Comparison of Fig. 37c to Fig. 37d shows that as the ELM frequency increased due to higher fueling, the average ELM energy loss dropped. While the change in WMHD due to ELMs was quite different between the ECH-only and NBI-only reference shots in Fig. 37c, at the highest fueling level the drop in WMHD due to ELMs is very similar between the gas-fueled and pellet-fueled discharges (Fig. 37d).

Pedestal MHD Stability As noted above, some changes in the pedestal structure (especially the pedestal width and the displacement between the temperature and density pedestal locations) were observed during the fueling scans. These pedestal changes are expected to influence the behavior of instabilities in the pedestal, particularly the peeling-ballooning mode (PBM), which is driven by pressure gradients and edge currents [86]. This sensitivity has been demonstrated in other experiments which have shown that PBM stability is affected by profile details very near the separatrix, such as the exact location of the pedestal pressure gradient [61, 73].

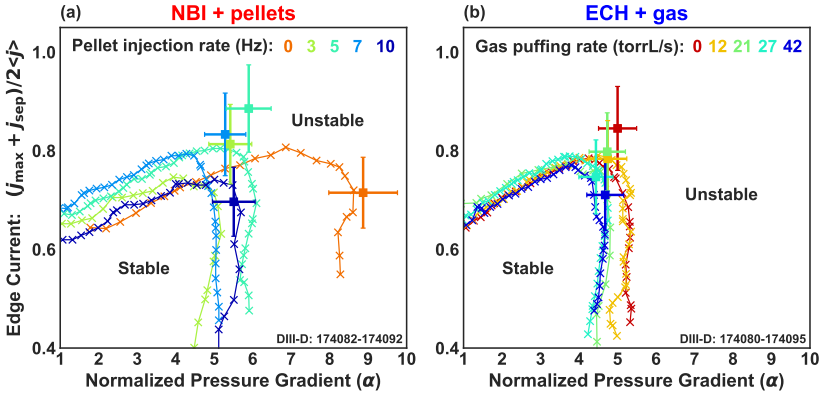

Figure 38: *Stability boundaries calculated with ELITE for (a) the pellet-fueled discharges and (b) the gas-fueled discharges. Stability boundaries are shown with lines (through X's) and solid points show experimental operating points just prior to ELM onset. Same-color profiles have similar total fueling rates [70].*

The ELITE code [87] was used to calculate the PB stability boundary for the set of discharges presented in this study. Figure 38 shows predicted instability thresholds as well as experimental operating points in the standard stability space of normalized pedestal current density vs normalized pedestal pressure gradient. Throughout the two fueling scans, the analyzed experimental cases are all near the nose of the PB stability boundary, suggesting that the ELMs in these discharges resulted from strongly coupled peeling and ballooning modes of moderate mode number. In the pellet-fueled discharges (figure 38a) a large reduction in the size of the stable region was observed after the injection of the first pellets. This large inward shift of the ballooning stability boundary is correlated with a strong reduction of the edge temperature gradient between 0 Hz and 3 Hz pellet injection, and indicates that there was a robust change in the plasma stability. For additional pellet fueling, the location of the PB boundary did not exhibit a clear trend and the computed PB thresholds are likely within the experimental uncertainties. It should be emphasized that the smaller normalized pressure gradient in the pellet-fueled cases compared to the 'no pellet' baseline does not correspond to lower pedestal performance since the pedestal widened, keeping the overall pedestal pressure constant. Increases in the fueling rate for gas-fueled shots showed a trend to

shift the ballooning boundary slightly inwardly, as shown in figure 38b. This result is in line with previous studies in closed divertor configuration on DIII-D [98].

An important implication of the fact that MHD stability limits the pedestal evolution is that stability-related physics may cause a very significant amount of the pedestal particle transport. Measurements on DIII-D have shown that for a wide range of plasma conditions, the time-averaged particle loss due to ELMs is about 25% of the total particle loss from the confined plasma [76]. Given that ELM losses are primarily from the pedestal, it is plausible that the pedestal contributes much of the total particle loss from ELMs and that the relative effect on the pedestal is larger than 25%. This issue more work in order to more fully understand the structure of the density pedestal.

Comparison to EPED1 Model The fueling scan and source location variation provide a good data set to test predictive capability of the EPED1 model [86], which predicts the pedestal height and width at a given density and in a type-I ELMing discharge. For both the gas-fueled and pellet-fueled scans, figure 39 shows a comparison of the pedestal height prediction from EPED1 (open markers) with the measured pedestal height (closed markers). Within error bars, including 15-20% on the model predictions, the predicted pedestal height is in reasonable agreement with the measured pedestal height for the gas-fueled discharges.

EPED1 also qualitatively reproduces the higher total pedestal pressure observed in the pellet-fueled cases compared to the gas-fueled discharges, which is demonstrated in Fig. 35. However, these predictions do not fully capture the quantitative difference in the height of the total pedestal pressure observed in experiment. In particular, the model consistently under predicts the pedestal height in the pellet-fueled discharges. These results suggest that a more centrally-located particle source location can increase the pedestal height above the EPED1 prediction. However, it remains to be seen if the qualitative differences between EPED1 modeling of pellet and gas fueled discharges would be observed over a wider data range.

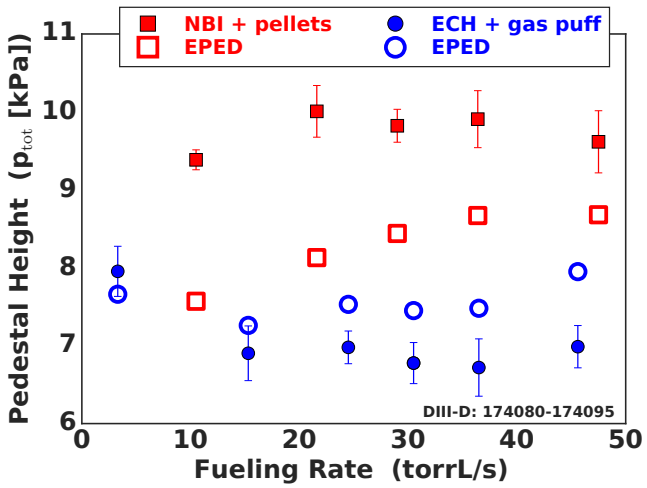

Figure 39: *Height of the total pedestal pressure profile vs fueling rate. Experimental values are shown with solid markers; EPED1 predictions are shown with open markers. EPED1 is unable to reproduce the full change in the pedestal height observed between the two fueling schemes [70].*

Differences in the comparison of EPED1 predictions vs experimental data for the pellet-fueled vs gas-fueled discharges potentially could be partly due to differences in fueling profiles. The role that neutral sources play in setting the pedestal density structure has yet to be incorporated into the EPED model. It should also be noted that a modified methodology for making predictions with the EPED model was used in this report for the section "Effect of Divertor Configuration on Pedestal". This methodology addressed changes in profile characteristics and it yielded improved agreement between pedestal predictions and experiment for studies in that section. This methodology has not been applied to the data shown here. It is plausible that such a treatment might improve the agreement between predictions and experiment for these data as well.

Summary of studies using fueling location to study pedestal structure An experiment was carried out in DIII-D in FY18 to determine the impact of the particle source location on the pedestal structure. The goal of this experiment was to vary the radial location of fueling from core to primarily edge/SOL fueling through a combination of pellet and NBI fueling (i.e. core) vs. gas puffing (i.e. SOL fueling). The intent of this experiment was to determine if there were measurable changes to the pedestal profiles due to a change between more core and more edge pedestal fueling. The thesis of the experiment was that more core fueling would provide a qualitative way to determine if a particle pinch must be invoked to help explain the pedestal density structure, in which case changes in local source might not have a discernible effect on the pedestal, or whether the pedestal structure was indifferent to the local source, which would suggest that particle transport, likely a pinch, plays an important role in setting the pedestal structure.

1) Scans of particle injection rate were performed with both the core source (pellets) and edge fueling (gas puffs). Systematic changes were measured for both the pedestal electron temperature and density profiles. For the same fueling rates, core fueling showed higher achieved pedestal electron densities and temperatures than edge fueling. In addition, discharges with more edge fueling generally showed a more significant outward shift of the density profile compared to the temperature profile than the discharges with more core fueling. Only at the highest achieved density did the pellet-fueled density display a similar shift.

2) Modeling was performed to obtain 1D radial profiles of the local particle source rate from these experiments. The modeling shows that the core fueling provided a much larger source in the pedestal than the edge fueling. This result confirmed the main expectation of the experiment, that the more core fueling scheme would indeed provide a larger particle source in the pedestal than the more edge fueling scheme.

3) Points 1) and 2) show that changes of the density pedestal structure occur with changes in the radial location of fueling. The changes are consistent with an increased local source increasing the the density in the pedestal. Thus, the experiment does not provide evidence that a pinch must be present to explain the experimental observations. Of course, the presence of a pinch cannot be completely ruled out by this work.

4) The increased particle source from gas puffing as well as pellet injection caused a significant increase in ELM frequency as well as a reduction in ELM size (energy loss per ELM). Certainly for gas fueling, this result is not new and is consistent with observations on many machines. Of interest here is that at the highest fueling levels, there was no measurable difference of energy loss for more core vs more edge fueling. These results show that pedestal fueling rate has a profound effect on pedestal structure by affecting the rate of approach towards the ELM instability.

5) The measured pedestal pressure profiles are consistent with the predictions of peeling-ballooning stability as made with the ELITE code. This is shown for the fueling scans with both more core and more edge fueling. These results are not surprising, given the success of the PB theory in explaining many pedestal observations. However, in the context here, it should be recognized that ELM effects due to PB stability limit how far the pedestal can evolve and thus are providing significant density transport.

6) For the gas-fueled discharges, the EPED1 model makes a small over prediction $\sim 10\%$ of the experiment pedestal pressure height. EPED1 also qualitatively reproduces the higher total pedestal pressure observed in the pellet-fueled cases due to the higher Shafranov shift, β_N, and $n_{e_{ped}}$ observed there. However, these parameter changes do not fully capture the quantitative difference and the experimental pedestal pressures are about 20% higher than the EPED1 predictions (as opposed to

about 10% lower for the gas fueled cases). The particle source profile is not explicitly modeled in EPED1 and these results provide evidence that accounting for this source may be needed to obtain best agreement with the data.

3.3 Variation of fueling location with low-field and high-field side gas injection and supersonic gas injection

New analysis has been performed on NSTX data from H-modes with gas injection at various locations (e.g., low-field side and high-field side conventional gas injectors and a supersonic gas injector. Under the assumption that the H-mode pedestal is fueled by neutrals recycling from the divertor target plates or main chamber, the pedestal density width with respect to edge neutrals is determined by the neutral penetration depth. The thermal neutrals penetration depth is in turn determined by the ionization and charge exchange mean-free-paths. In this model [58], the pedestal density width is inversely proportional to the pedestal height (i.e. density) because the neutrals mean-free path decreases with density. The pedestal electron density profile in such case has about the same characteristic scale length as the neutral density profile under the assumption of a spatially uniform particle diffusion coefficient. If the supersonic gas injection (SGI) penetrated into the edge plasma as a neutral gas jet, it could result, on the average, in a higher neutral penetration and increased pedestal widths. The goal of the analysis described below is aimed at studying systematic changes in pedestal profiles as a function of gas injection type (SGI, LFS, HFS) at various locations.

Fueling systems Since the work described below on fueling efficiency, we describe the NSTX fueling systems, namely the conventional and supersonic gas injectors.

Conventional gas injectors: Plasma fueling was accomplished with a number of conventional gas injectors on NSTX. Here the term conventional implies that the gas flowing through these injectors is always in the viscous (Poiseuille) flow regime with low Knudsen numbers (a ratio of the mean free path to a gas tube diameter), and the gas molecule (atom) distribution is close to thermal (Maxwellian). The flow rate in this regime is largely defined by gas pressure for a given hardware configuration: $\eta \sim D^4\ P^2$, where D is the tube diameter and P is the plenum pressure. The NSTX conventional gas injectors were built with commercially available components [15, 4]. They are composed of piezoelectric dozing valves controlled by the NSTX plasma control system and sufficiently large plena filled with gas at a pressure up to $P \leq 2500$ Torr. The gas injectors in this study are the low-field side Injector 1, located in the top part of NSTX, and two similar high-field side injectors, located on the inner wall at the equatorial plane (HFS) and about 1 m above the equatorial plane (HFS-shoulder) [46]. The locations of the conventional gas injectors are shown in Fig. 40. The injector 1 gas flow rate was calibrated and well controlled. The HFS injectors had a one-state pneumatic gate valve positioned about 2 m from the orifice, resulting in longer time response. Once the valve was opened, the HFS injector would produce a large initial injection rate followed by a continuous injection with decreasing rate. The midplane HFS injector has a long tube and a long time response compared to the HFS-shoulder injector. The HFS injector fueling was credited for improved H-mode access reliability and H-mode discharges with lower LH power threshold in NSTX [59, 60].

Supersonic gas injector: The SGI on NSTX has been described elsewhere [90, 89] and only some relevant details are highlighted here. The SGI is mounted on an outside port located about 19 cm above the equatorial plane on the low field side. The SGI apparatus includes a number of magnetic pickup coils, a Langmuir probe, two thermocouples, and a small converging-diverging graphite Laval

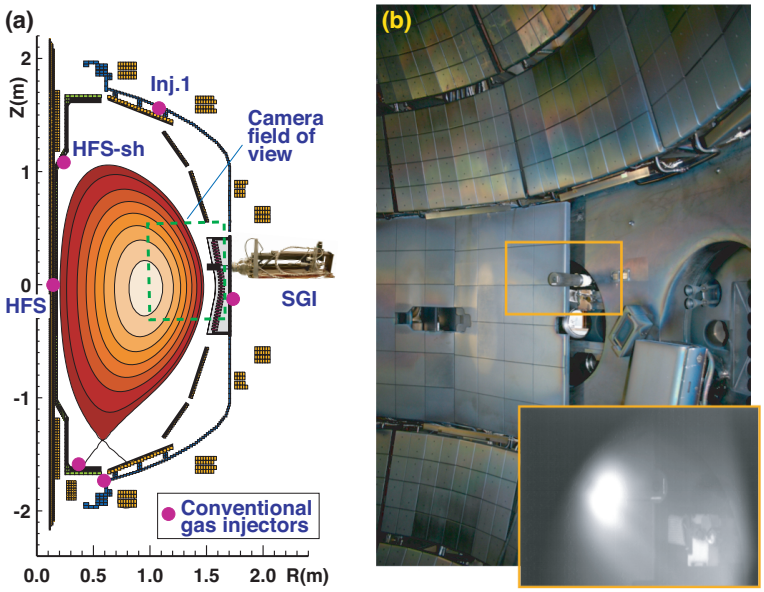

Figure 40: *A schematic of the SGI and conventional gas injectors on NSTX. (a) A schematic showing the midplane SGI, the top Injector 1, the top HFS-shoulder injector, (HFS-sh) and the midplane HFS injector. A camera field of view and an approximate domain of Degas 2 simulations is also shown. (b) A photograph of the SGI head inside the NSTX vacuum vessel at a typical fueling position. The inset shows a spectrally unfiltered image of the SGI gas injection into a H-mode plasma edge taken by a fast camera.*

nozzle attached to a piezoelectric gas valve with time response of 2-3 ms. The nozzle is capable of producing a deuterium jet with Mach number $M \leq 4$, a jet divergence half-angle of $\theta = 6 - 25°$, estimated gas density at the nozzle exit $n \leq 5 \times 10^{23}$ m^{-3}, estimated temperature $T \geq 70$ K, and flow velocity $v = 2.4$ km/s. The nozzle Reynolds number $Reis \simeq 6000$. The nozzle and the valve are enclosed in a protective shroud made of carbon fiber composite. The SGI package is mounted on a movable vacuum probe that enables nozzle radial translation. The range of translation is from $R_{major} = 198$ cm that corresponds to the vacuum vessel wall, to $R_{major} = 152 - 158$ cm that corresponds to the plasma separatrix. The SGI was implemented in two stages on NSTX: in the first stage a single-pulse capability (per one plasma discharge) and a 2500 Torr maximum reservoir (plenum) pressure P_0 were implemented. In the second stage, a multi-pulse capability and a 5000 Torr reservoir pressure were implemented. The SGI performance and gas jet characteristics were characterized by laboratory measurements to derive the above parameters. The SGI flow rate was calibrated *in situ* in the laboratory and on NSTX using absolutely calibrated pressure gauges and vacuum vessel volumes. Typically, the flow rate is about 150 Torr l / s at $P_0 = 2500$ Torr, and 220 Torr l /s at $P_0 = 5000$ Torr.

SGI fueling efficiency: A global metric

The SGI fueling efficiency was inferred in a number of experimental conditions using electron density measurements. The initial goal of these experiments was intended to compare fueling efficiency (FE) of the SGI and conventional gas injectors, and optimize the SGI free parameters, such as the plenum pressure P_0 (proportional to the flow rate), and the SGI-separatrix distance.

The fueling efficiency results are summarized for the NSTX ohmic H-mode discharges in a LSN configuration, 1-2 MW NBI-heated inner wall limited (IWL) L-mode discharges, and 2-6 MW NBI-heated LSN H-mode discharges with and without ELMs. The SGI experiments using the ohmic

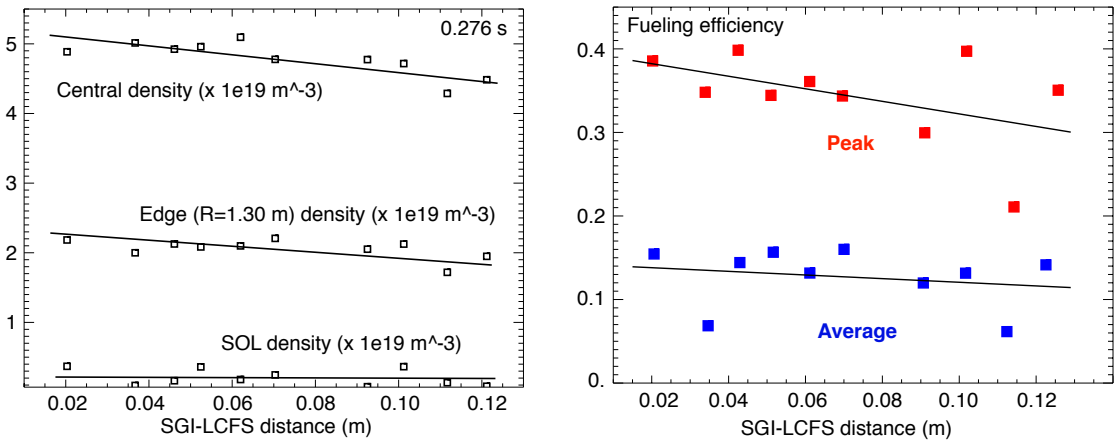

Figure 41: *Plasma densities (central, edge and SOL) (a) and fueling efficiencies (b) as a function of the SGI-separatrix distance in an ohmic NSTX discharge. A reduced SGI flow rate was used in the experiment.*

LSN and the IWL L-mode discharges were motivated by NSTX discharge start-up optimization studies, and the need to understand the SGI fueling during plasma formation and at lower densities. Some of the experiments were conducted in the initial phase of the SGI implementation on NSTX, when the SGI capabilities were limited to only one pulse per discharge, the flow rate was limited to 120 T l /s.

The FE is computed using electron density measurements from either Thomson scattering system [49] or far-infrared interferometer [50]. The total electron inventory N_e is obtained by volume-integrating the n_e profiles at each time point. When possible a reference discharge without an SGI pulse was used to account for the baseline particle inventory. The reported FE studies were conducted before massive quantities of lithium were used in NSTX for wall conditioning; hence, the contribution from carbon to electron density profiles could be neglected. The SGI jet fueling efficiency $(d\,\Delta N_e/dt)\Gamma_{SGI}^{-1}$ was inferred as a function of time in one discharge, and as a function of SGI pressure and SGI-separatrix distance in dedicated experiment.

Shown in Fig. 41 are electron densities and fueling efficiencies obtained in ohmically heated 0.75 MA 4.5 kG L-mode plasmas fueled by a LFS gas and a 70 ms deuterium SGI pulse at a rate 3.15×10^{21} s^{-1}. A distance between the SGI and the plasma separatrix was varied from 13 to 2 cm, and the SG jet fueling efficiency in the range 0.05 - 0.22 was obtained as a function of the distance.

Shown in Fig. 42 are representative waveforms of a 1 MA 0.45 T 1-2 MW NBI L-mode plasma discharge. The SGI was located at $R = 157$ cm, and injected deuterium at a rate of $\Gamma = 4.5 \times 10^{21}$ particles/s. The total amount of SGI gas was 0.75 Torr-l, whereas the LFS gas was 11.5 Torr-l. In this configuration, the SGI fueling efficiency varied from 0.1 to 0.6. In the ramp-up phase, the fueling efficiency was in the range 0.10-0.30 when the plasma was positioned on the inner wall at a distance from 20 to 8 cm from the SGI. Here the FE was calculated using line averaged density from the FIReTIP diagnostic [50] with the accuracy up to ± 0.1.

We note that the distance between the SGI nozzle and the separatrix was determined by external constrains. While in OH 0.6-0.8 MA L-mode plasmas we did not observe any disruptive effects on the plasma or SGI head overheating at distances down to 1 cm. In NBI-heated plasmas the SGI head was always positioned in a shadow of the HHFW antenna limiter at distances 6-15 cm to avoid interaction with lost orbit energetic particles.

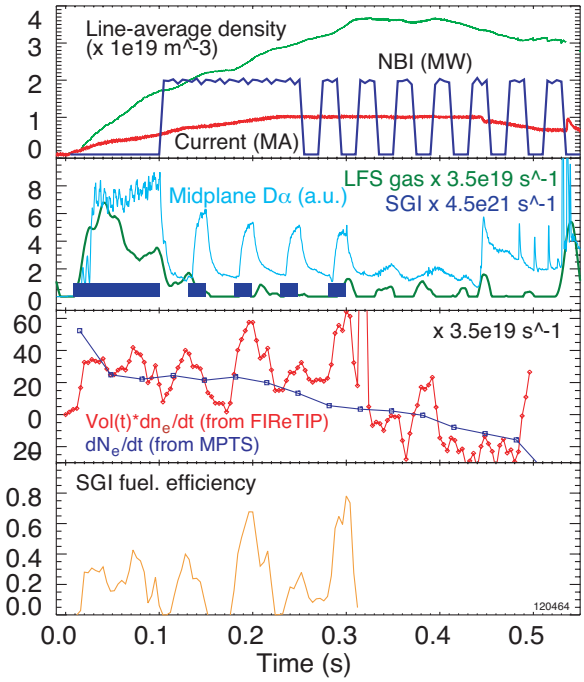

Figure 42: *Time traces in a inner-wall limited H-mode Discharge with a SGI injections. (a) Line-averaged density, NBI power, and plasma current; (b) LFS and SGI gas injection rates, Midplane D_α intensity; (c) Quantities used in fueling efficiency calculations: dN_e/dt from MPTS and $V_{NSTX}dN_e/dt$ from an interferometer; (d) Estimated SGI fueling efficiency.*

Because of the difference in fueling efficiencies and interaction with the plasma, it is difficult to compare the SGI and conventional gas injection (HFS or LFS) just by adding gas pulses into an existing H-mode plasma scenario. A different method was used to compare the SGI fueling with conventional gas injection fueling in diverted H-mode plasmas. A total amount of injected gas from a conventional gas injector and the SGI were compared, and matching plasma density was used as a criterion. The density was matched in 1 MA, 6-4 MW NBI heated H-mode discharges using different SGI and conventional gas injector scenarios. Then, the same injections were reproduced without plasmas to measure the amount of injected gas (i.e., injected particle inventory). This experiment is illustrated by Fig. 43 where two H-mode discharges fueled by the SGI and a LFS gas injection were contrasted. Also shown are calibrated neutral pressure measurements resulting from the SGI and conventional gas injector scenarios. Comparison of conventional LFS gas fueling at 80, 120 and 200 Torr l /s and SGI fueling showed that up to 1.3-2 higher rate needed for conventional gas to maintain same density (and plasma particle inventory).

Effect of fueling location

During the SGI injection, the injected particles were deposited in the H-mode pedestal by radial plasma transport and possibly direct ionization, hence the pedestal density quickly responded with an increase. However, the edge particle confinement time appeared to be low ($\tau \leq 10-20$ ms), and the deposited particles were eventually diffused from the pedestal region. The pedestal temperature usually decreased during the SGI pulse. The pedestal structure analysis was complicated by several experimental factors: in initial years of the SGI utilization, the SGI gas pressure was limited to 2500 Torr, hence a deep pedestal penetration was not expected based on the pressure balance argument (ram jet pressure vs plasma and magnetic pressures). The lithium conditioning

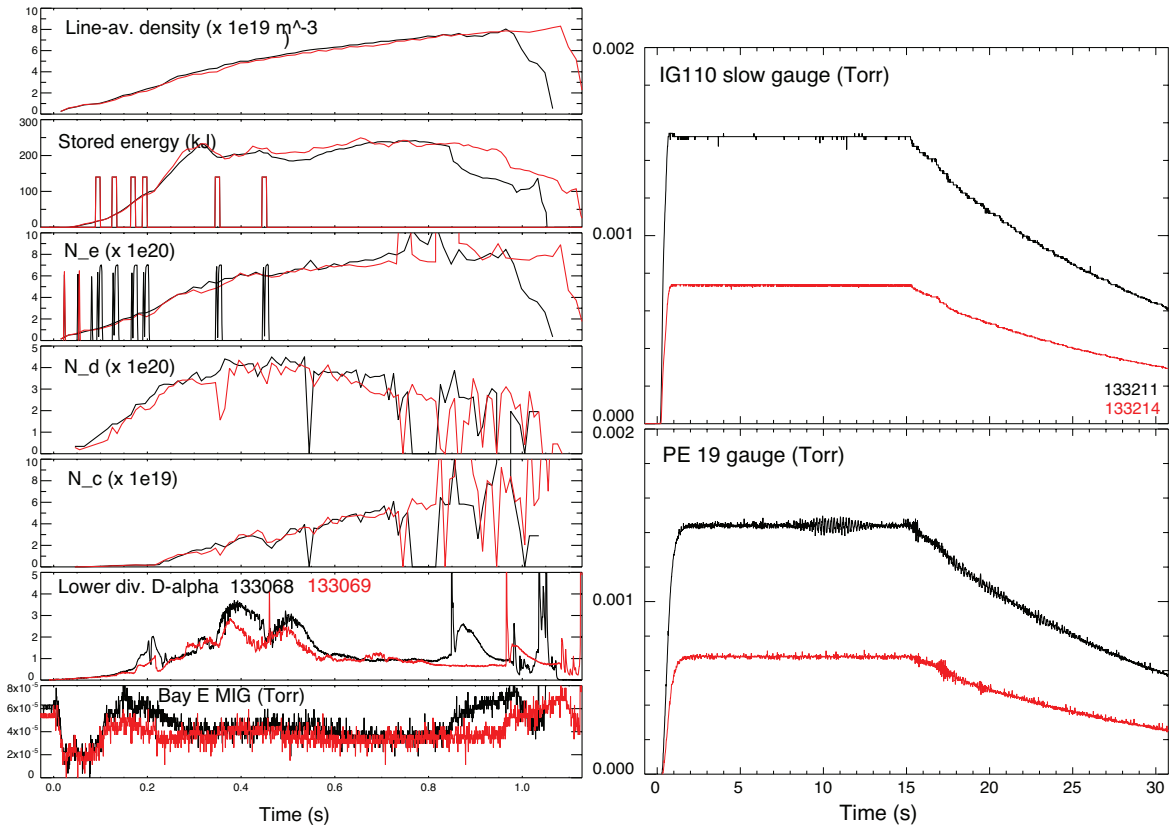

Figure 43: *Time traces of two H-mode discharges fueled by the SGI (red) and a LFS gas injection (black). (a) Line-averaged density; (b) Plasma stored energy and SGI time history; (c) Electron inventory and LFS gas injection history; (d) Ion inventory; (e) Carbon inventory; (f) Lower divertor D_α intensity; (g) Midplane neutral density. Right: Neutral pressure measurements resulting from the gas injection scenarios on the left, SGI (red) and a LFS gas injection (black).*

led to the modified edge impurity transport and pedestal stability, resulting in strong carbon accumulation in the pedestal and core plasmas. The analysis of pedestal structure was complicated as up to 30-40 % of the pedestal electron density would be coming from carbon ionization. It was not possible to fit the ion density profiles with a modified hyperbolic tangent function due to lack of charge exchange recombination spectroscopy (CHERS) diagnostic coverage at the edge and scrape-off layer regions. Shown in Fig. 44 are examples of edge density profiles in an H-mode discharge run well before the lithium conditioning campaigns, and a high-performance H-mode discharge with lithium conditioning. The MPTS diagnostic provides n_e profiles, whereas the CHERS diagnostic provides C VI density profiles, and the ion density profile is obtain by subtracting (six) electrons due to each carbon ion from the electron density profile. While it is possible to infer pedestal parameters based on electron density profiles, it is clear that carbon contribution is not negligible in lithium-conditioned H-mode profiles, while the connection between the neutral deuterium penetration and pedestal density structure (the pedestal height and width) is not clear. Fig. 45 and Fig. 46 show pedestal density operating spaces (pedestal n_e height and width) in different H-mode fueling scenarios in NSTX.

Summary

Both types of H-mode discharges with respect to lithium conditioning (well before and with) were

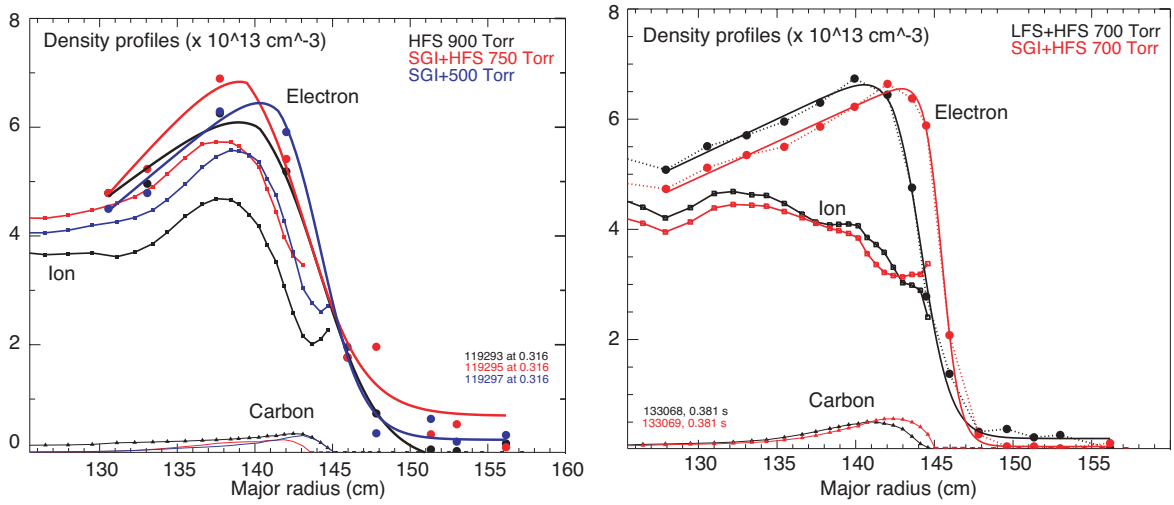

Figure 44: *A comparison of kinetic profiles measured in two H-mode discharges before lithium conditioning campaign (left), and with lithium conditioning (right). On the left panel, three discharges are shown: black lines, HFS-fueled discharge with 900 Torr, red lines - reduced HFS fueling (750 Torr) and SGI fueling, blue lines - reduced HFS fueling (500 Torr) and SGI fueling. On the right panel, two discharges fueled by LFS (black lines) and SGI (red lines), both with reduced HFS fueling (700 Torr).*

analyzed. Since the SGI and the LFS injectors were pulsed, the profiles were analyzed over some time during and immediately following the gas pulse. As the HFS gas injection was continuous, the n_e profiles were analyzed over a time period with densities similar to the SGI and/or LFS gas injector cases. From the presented data, two trends are apparent. First, the relationship (see Fig. 45) between the pedestal density and the pedestal density width is opposite to the pedestal gas fueling model [58] described above, where pedestal density width is inversely proportional to the pedestal density. Future work will investigate this observation. While the data has a high degree of scatter, the trend clearly shows that higher pedestal densities correspond to wider density pedestals for all fueling gas injector types (including SGI), suggesting that the impact of fueling location on NSTX pedestals is not as strong as in other devices.

The second trend is that H-mode discharges without lithium (ELMy) have wider density pedestals than the H-modes with lithium conditioning. This may be related to the pedestal broadening from ELMs in H-modes without lithium, and the shape of carbon contribution to electron density profiles, enhanced with lithium (as shown in Fig. 46). However, in general, neither trend is presently understood. With respect to the SGI fueling and penetration, the data are scattered and it is not possible to distinguish the SGI from other injectors based on the present analysis. This result could imply that a highly localized gas jet fueling, even if with higher edge neutral penetration, would not necessarily result in a wider density pedestal. It could also imply that the supersonic gas jet penetration (ionization profile) was similar to conventional HFS and LFS gas injection. This could be possible if the supersonic jet was fully penetrated by the ambient SOL plasma leading to molecular dissociation and atomic ionization as in a single particle approximation model rather than the jet acting as a self-shielding fluid jet. Additional experiments are needed to understand these results.

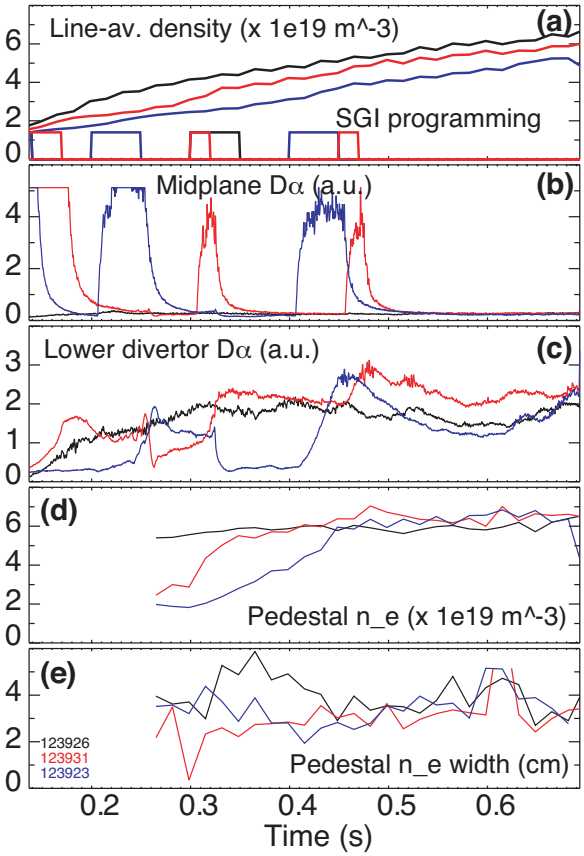

Figure 45: *Time traces of three 4 MW NBI-heated H-mode discharges with various amounts of fueling: black lines - HFS fueling (1100 Torr), red lines - reduced HFS fueling (500 Torr) and SGI fueling, blue lines - reduced HFS fueling (300 Torr) and SGI fueling. Reduced lithium amounts were used during the first lithium campaign on NSTX. (a) Line averaged density and SGI gas pulse programming; (b) Midplane D_α intensity showing SGI gas injections; (c) Lower divertor D_α intensity also showing SGI gas injections; (d) Pedestal density (pedestal height); (e) Pedestal density widths.*

3.4 Conclusion

Analysis of experiments has been performed to better understand the impact of the localization of the particle source on the pedestal structure. This study was performed with discharges using different fuelling technologies, which were expected to vary the radial location of fuelling, and with discharges using the same technology applied at different poloidal locations.

In DIII-D, scans of particle injection rate were performed using both a core source (pellets) as well as an edge source (gas puffs). Systematic changes were measured for both the pedestal electron temperature and density profiles. For the same fueling rates, core fueling showed higher achieved pedestal electron densities and temperatures than edge fueling. This is in agreement with modeling, which shows that the core fueling provided a much larger source in the pedestal than the edge fueling. In addition, discharges with more edge fueling generally showed a more significant outward shift of the density profile compared to the temperature profile than the discharges with more core fueling. Only at the highest achieved density did the pellet-fueled density display a similar shift.

The increased particle source from gas puffing as well as pellet injection caused a significant increase

in ELM frequency as well as a reduction in ELM size (energy loss per ELM). The measured pedestal pressure profiles are consistent with the predictions of peeling-ballooning stability as made with the ELITE code. This is shown for the fueling scans with both the more core and more edge fueling. However, in the context here, it should be recognized that ELM effects due to PB stability limit how far the pedestal can evolve and thus are providing significant density transport.

On NSTX-U, two trends are apparent. First, the relationship between the pedestal density and the pedestal density width is opposite to the pedestal gas fueling model [58] described above, where pedestal density width is inversely proportional to the pedestal height. Future work will investigate this observation. While the data has a high degree of scatter, the trend clearly shows that higher pedestal densities correspond to wider density pedestals for all fueling gas injector types (including SGI), suggesting that the impact of fueling location on NSTX pedestals is not as strong as in other devices.

The second trend is that H-mode discharges without lithium (ELMy) have wider density pedestals than the H-modes with lithium conditioning (see Fig. 44). This may be related to the pedestal broadening from ELMs in H-modes without lithium, and the shape of carbon contribution to electron density profiles, enhanced with lithium (as shown in Fig. 46). However, in general, neither trend is presently understood.

With respect to the SGI fueling and penetration, the data are scattered and it is not possible to distinguish the SGI from other injectors based on the present analysis. This result could imply that a highly localized gas jet fueling, even if with higher edge neutral penetration, would not necessarily result in a wider density pedestal. It could also imply that the supersonic gas jet penetration (ionization profile) was similar to conventional HFS and LFS gas injection. This could be possible if the supersonic jet was fully penetrated by the ambient SOL plasma leading to molecular dissociation and atomic ionization as in a single particle approximation model rather than the jet acting as a self-shielding fluid jet. Additional experiments are needed to understand these results.

The overall picture from studies on the two machines of the effect of fuelling location on the pedestal structure is mixed. Analysis of DIII-D data indicates that deeper fuelling with pellets did increase the pedestal density compared to equal fuelling in gas. In contrast, NSTX found that higher pedestal densities correspond to wider density pedestals, which suggests that the impact of fuelling location is weak. Understanding these varied observations requires improved understanding of the two determinants of the density pedestal: the particle source and the transport. These are both important long-standing problems. Understanding the particle source ultimately requires measurements of the source in addition to the data-constrained 2D edge modeling that is currently the best technique to determine the source. As noted above, all three machines have some diagnostics to measure the source and for DIII-D and NSTX-U continuation and expansion of the diagnostic capabilities is planned. Understanding the particle transport requires good knowledge of the source in order to quantitatively determine the transport as well as coupling between theoretical modeling and experiment in order to identify the underlying transport mechanisms.

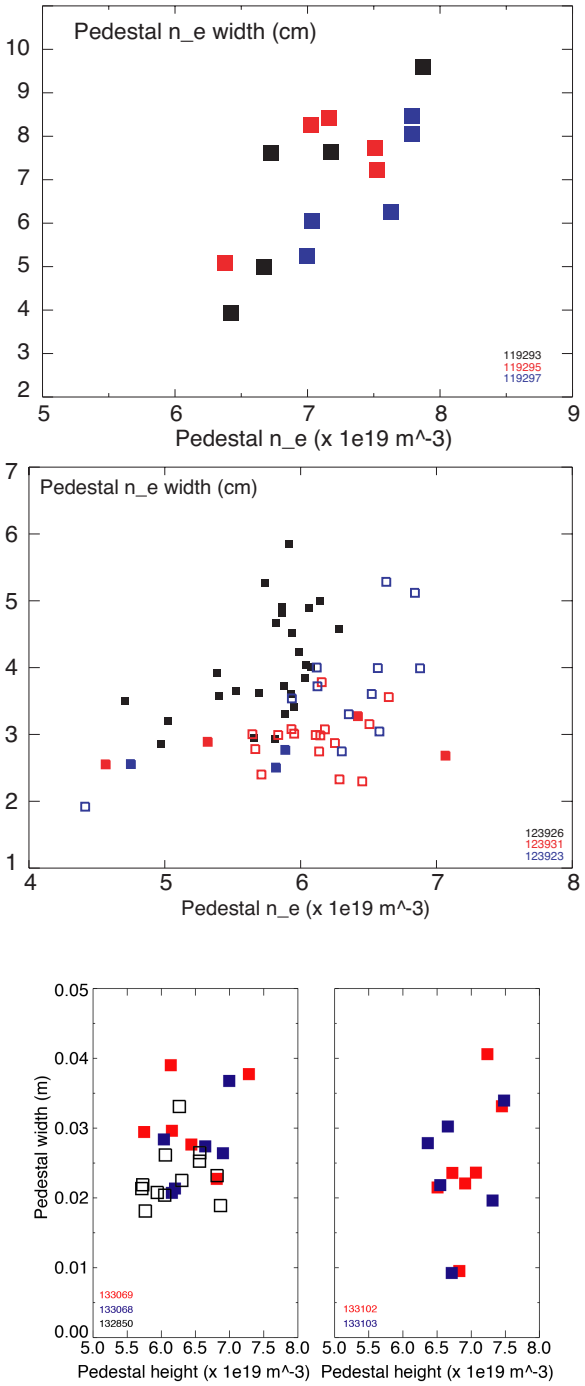

Figure 46: *Pedestal density operating spaces (pedestal width vs pedestal density (height)) for H–mode discharges with and without lithium conditioning and different fueling. (a) Discharges shown in Fig. 44 (a) with HFS and SGI fueling and before lithium conditioning campaigns on NSTX; (b) Discharges shown in Fig. 45 with HFS and SGI fueling and in the first lithium conditioning campaign on NSTX (reduced lithium); (c) Discharges shown in Fig. 44 (b) with HFS and SGI fueling and with lithium conditioning.*

4 Use of divertor closure to vary pedestal particle source

4.1 Introduction

In tokamaks, significant fueling of the plasma can come from recycled neutrals launched from near strike points in the divertor. Therefore, plasma performance features that fall under the influence of the edge ionization source may depend significantly on the degree of neutral screening from the divertor. Another term for screening is divertor closure, which refers to the ability of a divertor to baffle the escape of neutrals from the divertor. A more closed divertor better restricts neutral backflow to the main chamber plasma than does an open divertor.

It has long been recognized that modifications to divertor geometry to improve baffling of neutrals (degree of closure) was a promising route to improve divertor performance for future machines [57]. Several experiments have studied the capabilities of a more closed divertor. These include studies on JET to compare the Mark I, Mark IIa, and Mark IIGB divertor upgrades [77], studies on ASDEX of the LYRA Divertor II configuration [43], the use of a W-shaped divertor in JT-60 and its comparison to an open divertor [3], and variations of divertor geometry in Alcator C-Mod from a flat-plate to a vertical target to a slot divertor [55]. Experiments in DIII-D have compared the performance of a pumped, highly-baffled divertor desiged for high triangularity plasma shapes with an open divertor [2, 1]. Major goals of many of these studies were to enable divertor detachment at reduced upstream densities and to improve particle control by reducing core ionization.

A series of experiments have been performed in DIII-D by using different divertor geometries that vary divertor closure in order to investigate the roles of the deuterium ionization profile and radial transport in forming the density pedestal. The logic of these experiments was that an increase of divertor closure for otherwise similar plasmas would lead to a reduction of fueling within the pedestal. If core fueling was reduced, then measurements of a reduced electron density pedestalcould be used to help understand the role of neutral fueling on the pedestal.

For the research presented here, two types of comparisons were made. The first set of experiments used configurations in the standard DIII-D upper baffle and in a lower divertor with strike point on the divertor shelf. Based on experiments and modeling performed early in the operation of the upper divertor, the configuration with upper baffle was expected to have reduced fueling by about a factor of two as compared to the lower more open divertor [2, 1]. The second set of experiments compared the Small Angle Slot (SAS) divertor, recently installed on the ceiling of DIII-D [33, 84] with a divertor configuration with strike point on the lower baffle plate. SOLPS modeling was used in the design of the SAS divertor and predictions were that it would have very good baffling of neutrals (thus, high closure).

The research presented here shows that the degree of closure does quantitatively affect the ionization source in the pedestal. These charactistics, coupled with the large variation of closure that has been studied, show that the magnitude of the pedestal density increases with an increased ionization source in the pedestal. In addition, increased closure has led to some changes in the density pedestal structure by increasing the separatrix density relative to the pedestal density. Closure is also seen to affect the total pedestal pressure, indicating that divertor effects, presumably via the ionization source, play an important role in setting the pedestal structure.

4.2 Comparisons of Baffled Upper Divertor and Open Lower Divertor

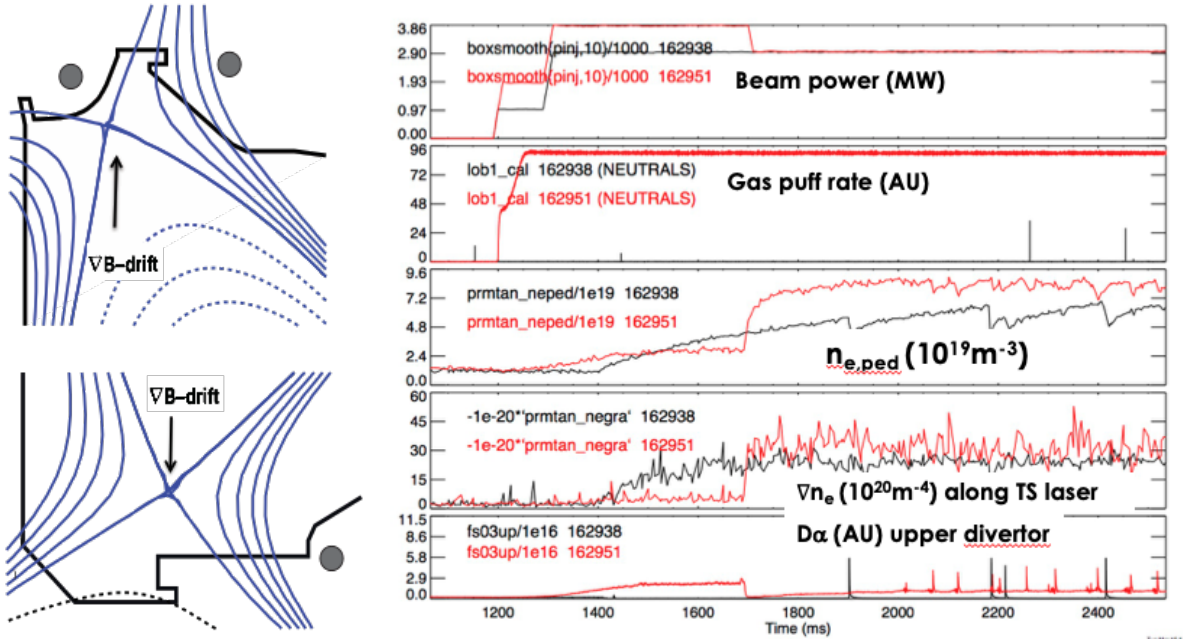

Figure 47: *a) Left panel: USN and LSN equilibria. Circles indicate locations of cryopumps. b) Right panel: Waveforms of beam power, gas puff rate, pedestal density, maximum gradient of pedestal electron density and divertor Dalpha for closed divertor at lowest (black) and highest gas puff (red).*

The first set of experiments was performed in standard DIII-D divertor configurations. The equilibria used are shown in Fig. 47. A lower single null (LSN) shape, with the outer strike point on the lower shelf, provided the lowest closure (lowest baffling of neutrals by the divertor). An upper single null (USN), with outer strike point in the baffle of the upper outer cryopump provided the highest closure (highest baffling of neutrals). Shapes of the two configurations were maintained as similar as possible. However, a higher triangularity was required for the closed divertor. The toroidal magnetic field BT direction was set so that the ion B x B drift was towards the X-point for both configurations. For all discharges, BT was 2.1 T, plasma current IP was 1.3-1.4 MA and data were taken at injected beam powers Pinj of 3 and 5 MW. For each configuration, a series of fueling scans was performed with constant gas puff rates applied during L and H-mode phases and changed shot by shot. The right panel of Fig. 47 compares waveforms for two closed divertor discharges, one with no gas puff and one with an applied gas puff. These waveforms show typical operation of the experiments with the beam power being held constant through the H-mode phase and gas puffs being applied well before the L-H transition and maintained constant

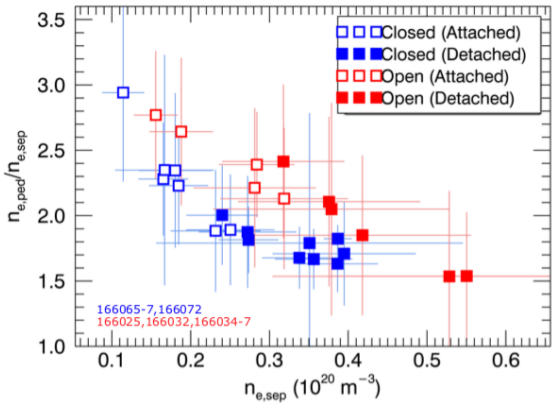

Figure 48: *Measured values of ratio of pedestal to separatrix density, as a function of ne,sep for open (red) and closed (blue) divertors. [67]*

throughout the discharge. These discharges show typical phenomenology: an increased gas puff increases the pedestal density, the maximum gradient of the pedestal density and the ELM frequency. Some results of these experiments have been already reported previously [51, 88, 98, 68, 18]. The results presented here extend the previous research and include analysis of fueling rates at higher heating powers than analyzed previously.

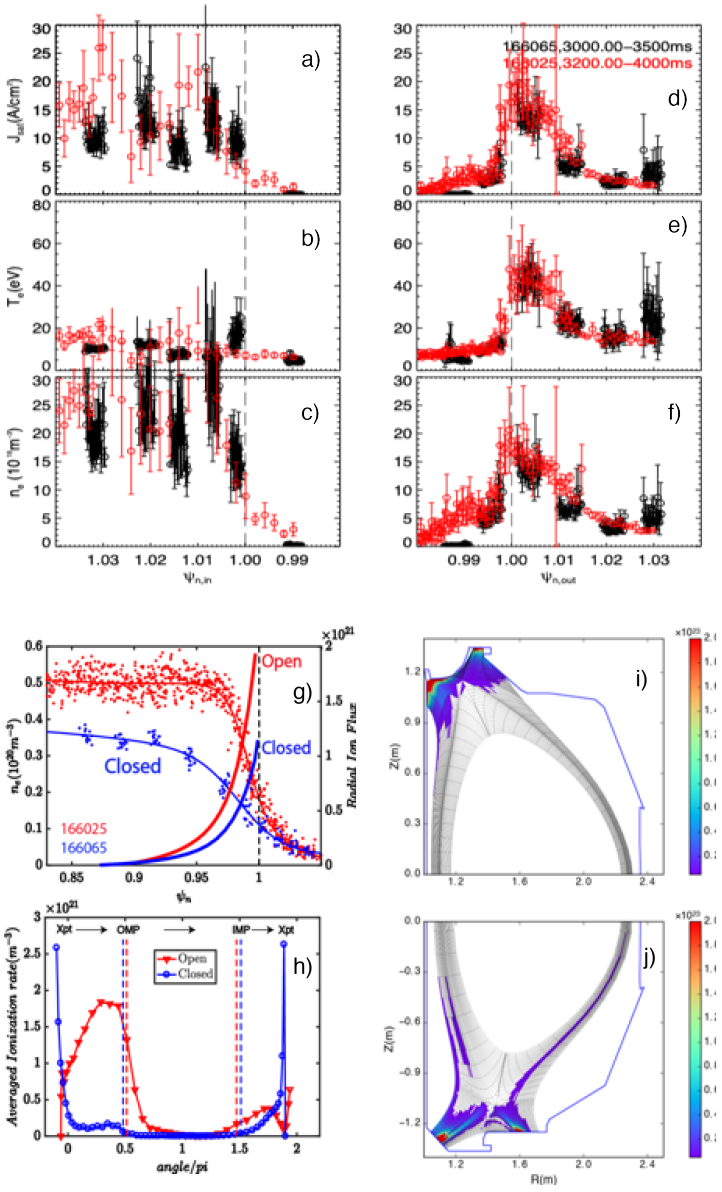

Figure 49: *a-f) Comparison of divertor Langmuir probe profiles for closed (black) and open (red) divertors. a-c) are profiles of JSat, Te and ne at inner divertor and d-f) are profiles at outer divertor; g) pedestal ne profiles for open (red) and closed divertors (blue) as well as radial ion fluxes based on OEDGE ionization sources for same cases; h) D ionization rates inside separatrix vs poloidal angle; 2D ionization rates (m-3 s-1) from OEDGE for (i) closed divertor and (j) open divertor [99].*

Effect of divertor closure on ratio of nesep to neped Analysis of these experiments shows that divertor closure affects important aspects of the density pedestal structure. An important trend is that the more closed divertor shows a lower ratio of electron density at the pedestal (neped) to the density at the separatrix (nesep) as compared to the more open divertor. This trend is illustrated in Fig. 48, which shows that the ratio is uniformly lower for the closed as opposed to open divertor over the range of available nesep in the database. The following sections will examine the density profiles and fueling in 3 different comparisons of open and closed divertor. In these cases, the more closed divertor has lower, equal and higher values of nesep than the open divertor discharge chosen for comparison.

Discharges with matched divertor parameters One basis for choosing USN and LSN discharges for comparison is to use discharges which have very similar profiles of JSat, Te, and ne at the divertor plates. The logic for this choice is that the two different divertors would have similar sources of neutrals, given similar plasmas at the divertor plates. Fig. 49a-f shows an example of LSN and USN divertor profiles which were very similar. These discharges exhibited clear changes in the pedestal density, illustrated in Fig. 49g, with the pedestal density and the separatrix density being lower for the closed than for the open divertor case.

The OEDGE code [56, 41] was used to model the neutral sources in the pedestal for the two discharges. OEDGE code computes 2D ionization based on extrapolation of divertor measurements of temperature and density to upstream measurements, obtained with Thomson Scattering. For the case studied here, 2D ionization rates from OEDGE are shown in Fig. 49i-j, which show significantly more ionization near the midplane for the open divertor than the closed divertor. (OEDGE does not have plasma between the outside of the mesh and the wall, but plasma density in that region is very low.) The net core ionization vs poloidal angle, shown in Fig. 49h, is higher for the more open divertor. This analysis shows that the open divertor allows for more neutral leakage up to the midplane than does the closed divertor. At the midplane the flux surfaces are much more compressed than near divertor targets and it is expected that it is easier for these neutrals to penetrate and fuel the pedestal. Thus the pedestal in the open divertor can be fueled to a higher density profile. Analysis of similar discharges with SOLPS confirms the qualitative picture that the closed divertor localizes fueling more to the divertor region than the open divertor [88, 18]. The modeled ionization rate profiles have been used with the measured pedestal profiles to compute radial ion fluxes in the pedestal, based on methodology discussed in [51]. These fluxes are shown in Fig. 49g and are roughly a factor of 2 higher for the more open divertor, consistent with a higher particle source in this configuration. The conclusion drawn from these results (and similar analysis in [51]) is that the increased pedestal ionization for the open divertor caused a higher pedestal density than obtained in the closed divertor.

Discharges with matched separatrix densities In the comparison of closed and open divertor discharges (DIII-D discharges 166065 and 166025, respectively) in the previous section, the discharges were chosen to have very similar profiles at the divertor. As shown in Fig. 49g, the pedestal density profile for the closed divertor discharge was lower than that of the open. In addition, as the figure shows, the density at the separatrix was lower for the closed compared to the open divertor discharge. Another metric for comparing pedestal density profiles is the separatrix density, nesep, given that it is at the boundary of pedestal and the plasma on open field lines.

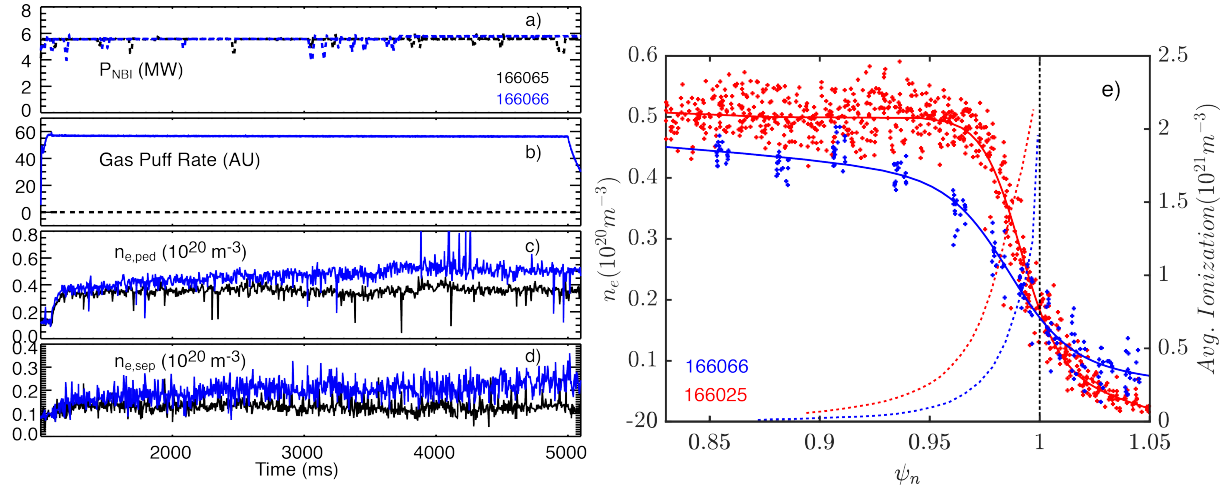

Figure 50: *a-d) Waveforms for 2 closed divertor discharges which differ only by gas puff. a) Heating power, b) Gas puff rate, c) neped, d) nesep. e) Pedestal density and ionization profiles for closed and open dischrges with matched nesep [67].*

With a suitable gas puff added to the closed divertor discharge, it was possible to match nesep of closed and open divertor discharges. Figure 50a-d shows a comparison of waveforms for two closed divertor discharges: the discharge used in the previous example and the discharge with

nesep increased to match the open divertor discharge. All control parameters for the two closed divertor discharges (shots 166065 and 166066) were identical with the exception of the gas puff rate. For example, Fig. 50a shows that the heating powers for these two discharges were the same whereas Figure 50b shows that discharge 166066 had an applied gas puff (blue line) compared to discharge 166065 which had no puff (dashed black line). This applied gas puff led to an increase of the both neped and nesep for discharge 166066 as compared to 166065 as can be seen by comparing the density profile in Fig.50e (blue data and line) with the density profile in Fig.49b (blue data and line). As Fig.50e shows, the separatrix density profiles for the open and closed divertor discharges in the comparison were identical, despite the fact that the closed divertor discharge had a lower pedestal density than the open divertor discharge. These data show that for a given nesep, the ratio of neped to nesep is lower for the closed compared to the open divertor discharge, consistent with the general trend that was shown in Fig. 48.

OEDGE analysis has been performed on these two data sets and the profiles of flux-surface averaged D ionization rates (m-3 s-1) are compared in Fig.50e (with the dotted lines). At all locations throughout the pedestal the average ionization rate is higher for the open compared to the closed divertor discharge. The computed ionization rates are nearly equal at the separatrix. As seen in the previous section, the implications are that a higher ionization rate in the pedestal produced a higher pedestal density.

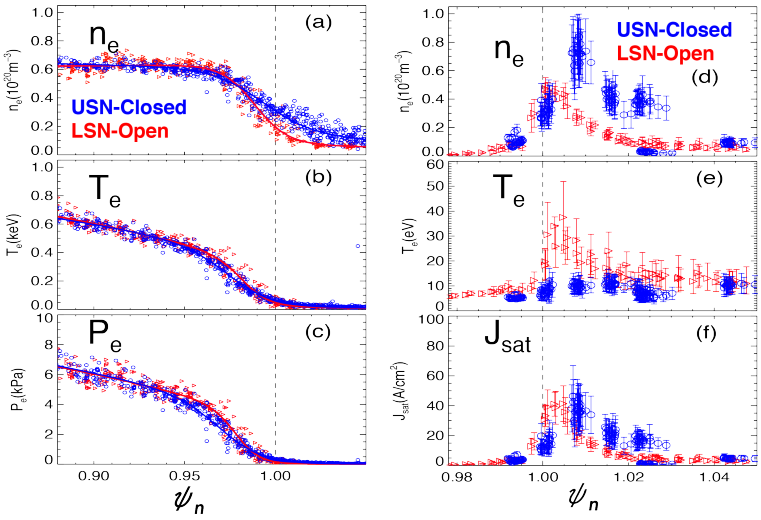

Figure 51: *Comparison of closed (USN) and open (LSN) divertors with same pedestal densities. Pedestal profiles for a) ne, b) Te and c) Pe. Profiles at outer divertor plates of d) ne, e) Te and f) Jsat. [99]*

Discharges with matched pedestal densities Another metric for comparing pedestal density profiles is the pedestal density, neped, given that it forms a boundary for the core density profile. With sufficient gas puffing, it has been possible to match pedestal densities for closed and open divertor configurations with other control parameters held constant. An example of this matching is shown in Fig.51a. In this comparison, the divertor plate parameters were not matched; the gas puff applied to the closed divertor resulted in a higher ne and Jsat at the divertor plate and a lower Te at the divertor plate compared to the more open divertor, shown by Fig.51 d, f and e,respectively. Under these divertor conditions, the closed configuration was partially detached while the open configuration was attached. Despite the higher gas puffing and partially detached divertor, the pedestal Te and pe values were nearly identical for the two configurations, as shown by Fig.51 b,c. One additional point of interest for this comparison is that for a given neped, the ratio of neped to nesep is lower for the closed compared to the open divertor discharge. This result is consistent with general trend that was shown in Fig. 48 and with the results of the previous two comparisons that have been discussed.

Modeling studies with SOLPS Modelling studies of the closed USN versus the open LSN

divertor configurations were also performed with the SOLPS5.0 code suite [18]. These calculations used the multi-fluid plasma transport code B2.5 [13] coupled to the Eirene Monte Carlo neutral transport code [79]. The background plasma is provided by B2.5 and Eirene is then used to launch neutrals into the plasma. SOLPS is a predictive code, but for this study, it was used in an interpretive way. That is, model transport coefficients were adjusted so that computed upstream profiles matched the experimental profiles. This modeling also included carbon.

This modeling was used to examine fueling in a pair of closed USN and open LSN discharges with the same separatrix electron density. The same heating power and recycling coefficients for both discharges and transport coefficients adjusted to match the upstream profiles. The results support expectations for the performance of the closed divertor and results of the OEDGE modeling, shown previously, that the closed divertor better confines neutrals to the divertor regions. Modeling was performed for open and closed discharges with the same nesep at the outer midplane. For this case, Fig. 52a-b show that there is a much higher molecular deuterium density confined to the volume near the closed divertor target than is the case for the open divertor.

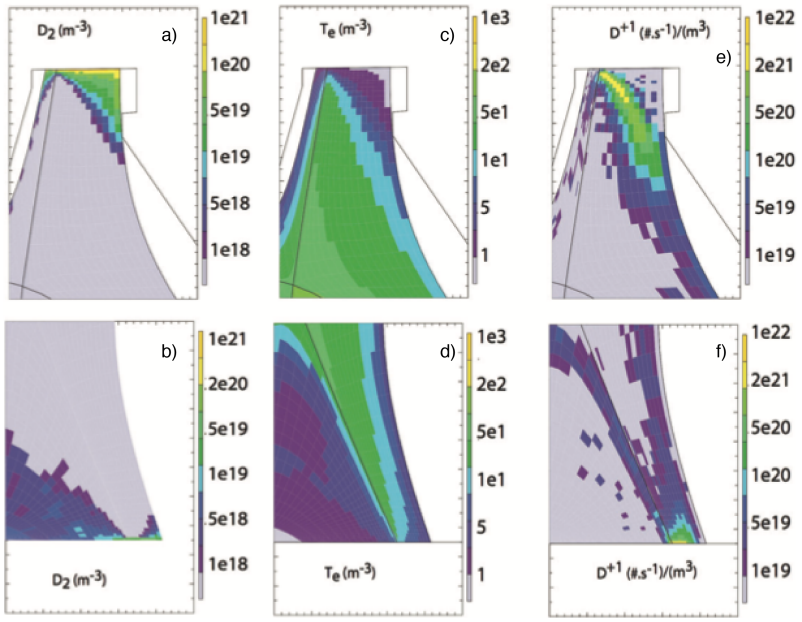

Figure 52: *2D contour plots from SOLPS modeling for closed (top) and open (bottom) divertor configurations. Divertor target is at top of each plot. a-b) D2 density, c-d) Te, e-f) Deuterium ionization rates for closed and open divertors, respectively. [18]*

This higher neutral density plays a role in maintaining a lower Te (Fig. 52c-d) and much higher ionization rate for Deuterium ions (Fig. 52e-f) near the divertor target for the closed compared to the open configuration. In addition, Fig. 52e-f demonstrates that higher ionization is computed outside of the divertor region for the open than for the closed configuration.

These results confirm the OEDGE modeling in showing the ability of the closed divertor to confine neutrals near the target whereas the open divertor configuration allows neutrals to escape from the divertor region towards regions where they may more easily penetrate the plasma. This SOLPS modeling is also consistent with previous SOLPS modeling of discharges in this dataset [88], which showed that the open divertor allowed neutrals to escape the divertor region much more so than for the closed divertor. All of these results also confirm the initial studies (2001) [1] of the closed USN divertor in which experiment and UEDGE modeling indicated that this configuration had significantly lower core ionization than an open LSN configuration. The recent modeling (e.g. Fig. 52) extends the previous results by using equilibrium re-constructions from the actual discharges, matching experimental upstream profiles and extending the analysis to several discharges.

4.3 Comparisons of SAS and LSN configurations

DIII-D recently installed a new upper tightly baffled divertor called SAS (Small Angle Slot) [33, 84] which allowed the comparison of discharges in a second closed divertor configuration and with the open divertor structure discussed previously [71]. The following section describes the effects on the pedestal obtained of switching between these two configurations.

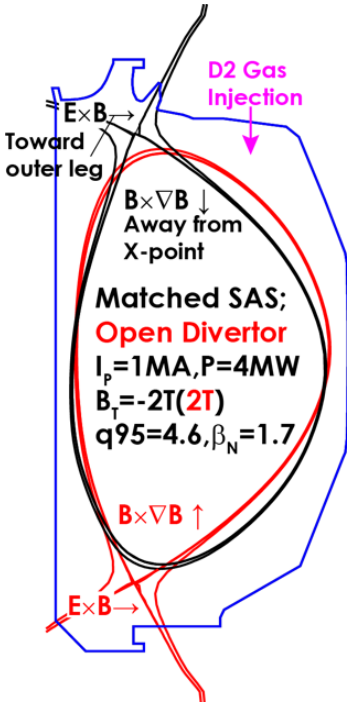

Figure 53: *Discharge shape used in the experiment testing the effect of divertor configuration on H-mode pedestal structure. Cases with the $B\times\nabla B$ drift in the unfavorable direction are shown. In the favorable direction both the $B\times\nabla B$ and $E\times B$ drifts are reversed [72].*

Experimental strategy The SAS divertor has been used in experiments to look at the effect of divertor closure and the $B \times \nabla B$ drift on pedestal characteristics. Discharges in the Small Angle Slot (SAS) divertor configuration were compared to Lower Single Null (LSN) open divertor discharges with both favorable and unfavorable $B \times \nabla B$ drift directions. Density ramps were carried out in each case via D_2 injection into the main chamber at both 4 and 8 MW co-neutral beam injection power. Figure 53 shows a comparison of the cross-sectional shapes of these discharges which were matched except for the vertical orientation.

Effects of divertor configuration on pedestal pressure Figure 54 compares the total pedestal pressure as a function of pedestal electron density for SAS with favorable $B \times \nabla B$ drift direction (black points), SAS with unfavorable $B \times \nabla B$ drift direction (blue points), and LSN with unfavorable $B \times \nabla B$ drift direction (red points). All these discharges had the same plasma current, toroidal field, cross-sectional shape and 4MW NBI. The Greenwald density for these discharges was $1.0 \times 10^{20} m^{-3}$. A large difference and trend in the pedestal pressure as a function of pedestal density was observed in these discharges in which only the divertor effects would be expected to differ. In the SAS and LSN discharges with unfavorable $B \times \nabla B$ drift direction, a pronounced reduction in the pedestal pressure and density was observed when a high radiation zone propagated to the region near the X-point. This X-point MARFE occurred at a significantly lower pedestal density in the LSN open divertor discharge and at a density slightly above the density at which the outer divertor leg became detached. For the SAS discharge with unfavorable $B \times \nabla B$ drift direction, detachment occurred at a somewhat lower density than in the LSN case but the high radiation zone did not reach the X-point until significantly higher density. Figure 54 also demonstrates that the pressure was significantly higher for the SAS divertor with favorable $B \times \nabla B$ drift direction than with unfavorable drift direction. Research discussed here concentrates on a comparison of the closed SAS and open divertors with unfavorable $B \times \nabla B$ drift direction.

Effects on profiles Figure 55(a-d) shows a comparison of the electron and ion profiles in the pedestal regions at a pedestal density of $0.46 \times 10^{20} m^{-3}$ for the three discharges of Figure 54. At this density all the discharges have very similar levels of carbon impurity density. The observed differences in the pedestal pressures are the result of differences in both the pedestal electron and ion temperatures. The width of both the electron temperature and density increase as the pedestal pressure increases. The ratio of the separatrix to pedestal electron density also is higher for the

discharges with unfavorable $B \times \nabla B$ drift direction.

Peeling-Ballooning Stability: Comparison of SAS and LSN Peeling-ballooning stability has been computed for the comparison of the closed SAS configuration to the open LSN configuration with the $B \times \nabla B$ drift in the unfavorable drift direction. For this purpose, kinetic equilibria were computed using the pressure profiles of Fig. 55 and current density profile set by MSE measurements in the core and a combination of Ohmic, neutral beam driven, and bootstrap current computed with NEO [7] in the pedestal. The pedestal pressure and current density were then varied independently to generate a grid of equilibria on which the ELITE code [87] was run to compute the stability threshold for peeling-ballooning modes, PBM. As is shown in Fig. 55e and is seen in many other experiments, the pedestals of these discharges reach the PBM threshold just before an ELM. Both the SAS and open divertor operating points are toward the ballooning branch but near the transition between peeling and ballooning with most unstable toroidal mode numbers of 25 and 35 respectively. Here the stability threshold is set as the point when the growth rate exceeds the diamagnetic stabilization level as computed from BOUT++ simulations in [85]. These results show that the pedestal pressure limits obtained in these two configurations are consistent with MHD limits due to peeling-ballooning stability.

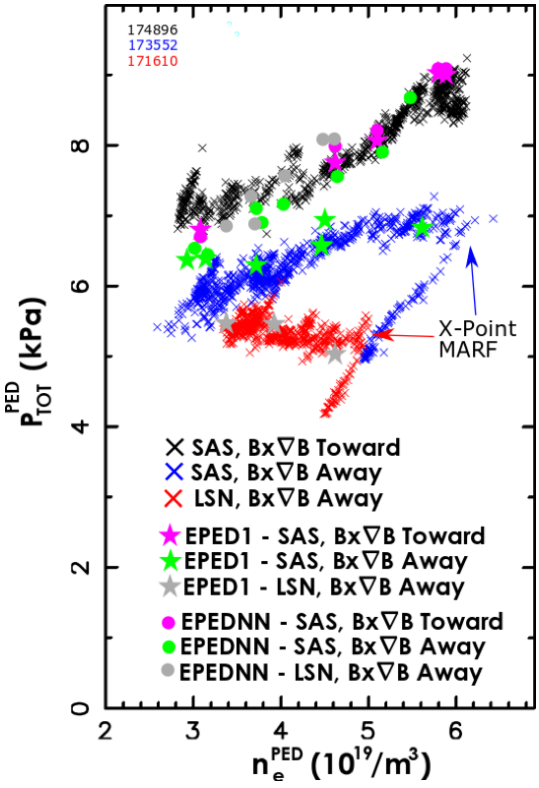

Figure 54: *Variation of the total (electron+ion) pedestal pressure with pedestal density for otherwise matched discharges with SAS divertor and $B \times \nabla B$ drift in the favorable direction (black crosses), SAS divertor with the $B \times \nabla B$ drift in the unfavorable direction (blue crosses), and LSN open divertor with the $B \times \nabla B$ drift in the unfavorable direction (red crosses). Also shown are predictions of the standard EPED1 model (filled-circles and labeled EPEDNN) and the alternative EPED1* model (filled-stars and labeled EPED1) [71].*

Time-dependent PBM stability during density scan During gas puffing into single null open divertor discharges with the $B \times \nabla B$ drift direction away from the X-point, the plasma stored energy, β_N, was observed to decrease with increasing electron density Fig. 56a. The overall stored energy reduction tracked the pedestal pressure reduction up until a high radiation zone reached the X-point resulting in strong pedestal pressure reduction relative to the central pressure and β_N, as shown in Fig. 56a. As the density rises the electron temperature profile becomes narrower while the ratio of the pedestal to separatrix electron density decreases and the gradient of the ion temperature decreases Fig. 56b-e. These relative changes in the pedestal profiles have an important impact on the stability of the pedestal peeling-ballooning mode that may be driving the pedestal pressure reduction with increasing density.

Particularly along the higher toroidal mode number ballooning mode branch of the PBM, the instability threshold is sensitive to the level of diamagnetic stabilization with the critical growth rate of the mode for instability $\gamma \sim \omega_{*i}/2$. Since $\omega_{*i} \propto \nabla p_i/n_i$, decreasing the ion temperature gradient while raising the separatrix density relative to the pedestal density tends to reduce ω_{*i},

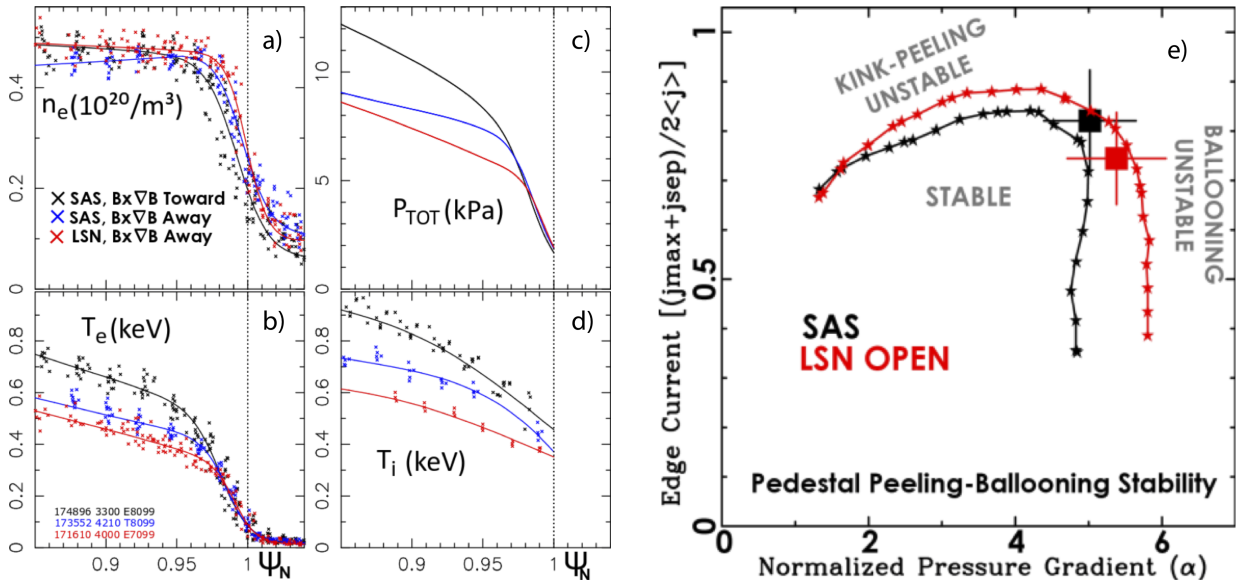

Figure 55: *Pedestal profiles of a)ne, b)Te, c)Ptot, d)Ti corresponding to the three discharges in Fig. 54 at* $n_{e_{ped}} \sim 0.46 \times 10^{20} m^{-3}$. *e) Pedestal peeling-ballooning stability boundary and experimental operating points from profiles of a-d [71].*

lowering the threshold for instability. This effect is demonstrated in Fig. 57a, with curve colors corresponding to times marked with vertical lines in Fig. 56a. In Fig. 57a the critical pressure gradient along the ballooning branch is reduced as the diamagnetic frequency decreases.

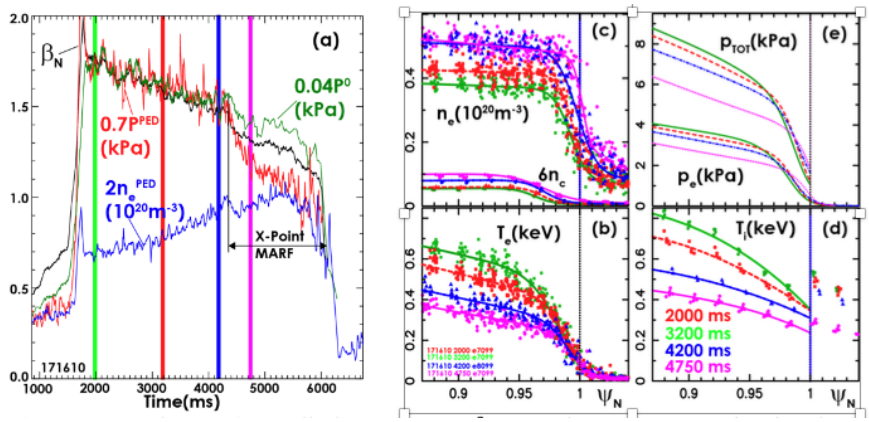

Figure 56: *a) Time evolution of overall plasma energy,* β_N, *central pressure,* P_0, *and pedestal pressure,* P_{PED}, *as pedestal density,* ne_{PED} *is raised with D2 gas puffing, b) electron temperature in the pedestal region, c) electron density, d) ion temperature, e) electron and total pressure; colors correspond to times marked in a) [72].*

If this reduction of the PBM ballooning branch instability threshold is combined with the pedestal width scaling corresponding to the kinetic ballooning mode constraint in the EPED model [85], $w = 0.076(\beta_{pol}^{ped})^{1/2}$ this model can account for the pressure reduction with density in this discharge, as shown in Fig. 57b. These results highlight the fact that, in the PBM ballooning branch limited regime, the achieved pedestal pressure is sensitive to the details of the relationship between the density and temperature profiles in the pedestal. A decrease in the ion pressure gradient will reduce diamagnetic stabilization and thereby the stability limit leading to further reduction in stability threshold. In a corresponding experiment using a closed rather than open divertor configuration, the ratio of the pedestal to

separatrix density did not decrease with increasing density and the diamagnetic stabilization improved resulting in an increase in the PBM critical gradient and pedestal pressure. This suggests that neutral fueling differences can impact the achieved pedestal pressure by changing the relative evolution of the density and temperature profiles thereby affecting the evolution of the diamagnetic stabilization and so the pedestal pressure limit. This is a key new interpretation of the data and suggests that neutral fueling may have more complex effects on pedestal structure than those that are usually considered.

Limitations of the EPED1.0 model and need for a better understanding of H-mode pedestal transport

The EPED model [85] successfully predicts the pressure at the top of the H-mode pedestal over a wide range of experiments to an accuracy of about 20%. In the model, the pedestal pressure gradient between ELMs is taken to have reached and to be limited by transport from kinetic ballooning modes, KBM. The KBM limit on the pressure gradient can be shown [85] to increase with pedestal width equivalent to the relation between pedestal width and height, $w \propto (\beta_{pol}^{ped})^{1/2}$. The pedestal expands and the pressure gradient expands, subject to the KBM constraint until a peeling-ballooning mode, PBM, is triggered thus setting the maximum pressure achieved between ELMs. In its usual form, EPED1.0, the model takes as inputs only the pedestal density and ZEFF, the overall β_N, I_P, B_T and the basic plasma shape parameters, R, a, elongation and triangularity. The model makes a number of assumptions 1) $T_e = T_i$, 2) the plasma boundary is located at one-half of the pedestal width out from the T maximum gradient point, 3) the n_e and T maximum gradient points are aligned, 4) the density at the plasma boundary is 1/4 the value at the top of the pedestal, 5) $Z_{\rm eff}$ is constant in the pedestal, 6) the equilibrium can be represented by an up/down symmetric shape without an x-point while matching the basic shape parameters. Many of these assumptions are known to impact the PBM stability but are not necessarily consistent with the experimental observations. Finally EPED1.0 takes the PBM instability threshold as the point where the growth rate exceeds the diamagnetic stabilization as estimated from the diamagnetic frequency, $\gamma/(\omega_{*i}/2) = 1$ where $\omega_{*i} = -(n/en_e)(\partial p_i/\partial\psi)$ is the maximum value in the pedestal. DIII-D experiments [52] indicate that a more accurate expression for the diamagnetic stabilization is required to improve the comparison of theory and data.

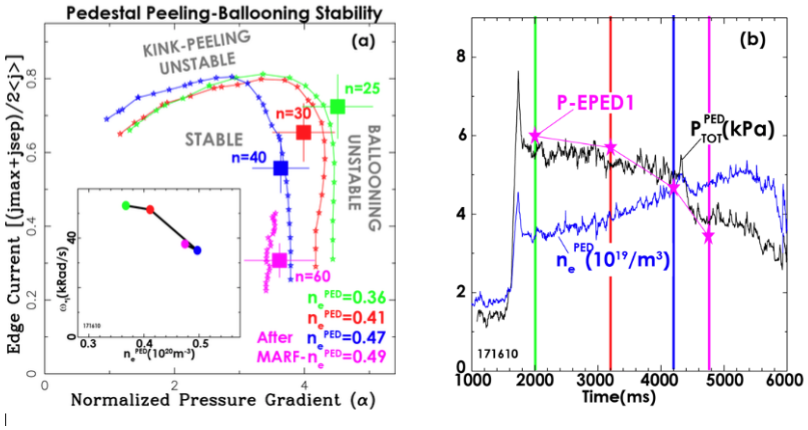

Figure 57: *a) Pedestal PBM stability through the density increase for times marked by corresponding colors in Fig. 56, showing the reduction in critical pressure gradient along the ballooning branch as diamagnetic stabilization weakens ω_{*i} in insert. b) Pedestal pressure reduction with increasing density is in agreement with predictions of EPED model [72].*

The limitations of the EPED1.0 model were clearly illustrated in DIII-D experiments where variations in the divertor conditions, keeping the usual inputs to EPED1.0 fixed, resulted in significant variation in the pedestal pressure. Figure 54 shows the variation in pedestal pressure with pedestal density, produced by main chamber D2 gas puffing, using the small angle slot divertor, SAS, configuration for the two different directions of the $B \times \nabla B$ drifts and an otherwise identically shaped lower single null, LSN, open divertor discharge. As expected, the EPED1.0 prediction for all three

cases is similar with small differences resulting from N and ZEFF variations. Here the EPED1.0 value is computed with a neural-net version of the code [63] labeled as EPEDNN in the figure. The EPED1.0 prediction however only agrees with the SAS case with $B \times \nabla B$ drift toward the X-point. However if the experimental relationship of the various profiles is maintained through a variation in width and height subject to the KBM constraint, and the actual experimental shape is used, and the more accurate form for the diamagnetic stabilization is used, good agreement between EPED and all of the cases is found. These calculations using an alternate evaluation of the EPED model are labeled EPED1* and are shown by the stars in Figure 54. These results demonstrate that while the constraints embodied in the EPED model are important in pedestal structure, additional physics, in particular the transport and source effects setting the relationship between the various profiles, is required for a fully predictive model.

Modeling Study with SOLPS

The design of the SAS divertor [84] was based on extensive modeling with the SOLPS5.0 code [13]. The approach was to use a slot divertor to provide very good baffling of neutrals, i.e., good closure. Subsequent more advanced modeling with SOLPS5.1, based on experimental data with the actual divertor structure, has confirmed that SAS divertor provides much better baffling than the open lower divertor in DIII-D [17]. Compared to SOLPS5.0, the SOLPS5.1 model uses a triangular mesh which spans the B2.5 mesh and the volume to the first wall. This SOLPS modeling is based on the same set of experiments and divertor shapes as shown in Fig. 53. The modeling used the same heating power and recycling coefficients for both discharges as well as fixed transport coefficients.

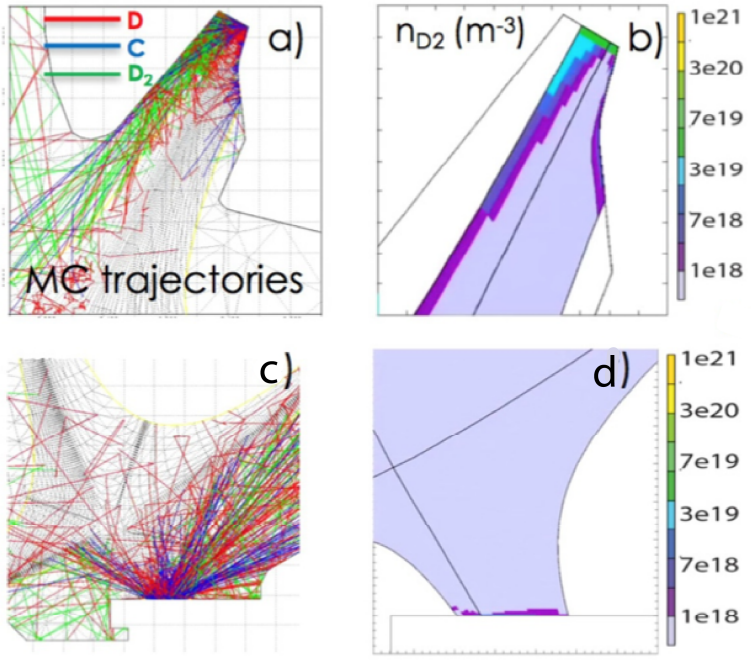

Figure 58: *SOLPS5.1 modeling for SAS (top) and open (bottom) divertor configurations. a,c) Monte Carlo trajectories of neutrals and b,d) 2D contour plots of D2 neutral density for SAS and open divertors, respectively [17].*

Fig. 58 shows results from modeling of a SAS and an open LSN discharge with the same separatrix density. Monte Carlo trajectories of atomic and molecular deuterium as well as neutral carbon are shown in Fig. 58a,c. This comparison shows that many more particles escape from the open divertor than from the SAS divertor. As a result, neutral baffing of the SAS divertor is much better and the neutral deuterium density near the SAS target plate is much higher than for the open divertor Fig. 58b,c. This modeling indicates that the SAS divertor does provide very good baffling of neutrals, as intended by the design.

4.4 Summary of studies using divertor closure as a tool to study pedestal structure

Divertor closure (baffling of neutrals) has been used as a tool on DIII-D to study pedestal structure and to address the goals of this milestone. Since divertor closure is strongly affected by divertor geometry, systematic experiments have been performed in different divertor geometries available on DIII-D in order to vary divertor closure and to document and model effects on the pedestal. In particular, systematic comparisons of USN discharges using the standard upper baffle have been compared with LSN discharges with the outer strike point on the lower baffle plate to provide relatively closed and open configurations, respectively. In the following summary, these studies will be referred to by the shorthand USN/LSN. Likewise, comparisons have been made of the new closed SAS divertor with the LSN discharges to provide complementary studies of closed vs open configurations. These studies will be referred to as SAS/LSN. Important results of these studies will summarized, as follows:

1) Modeling with SOLPS using experimental data confirms the expectation that the more closed divertors provide better confinement of neutrals to the region near the divertor plates for both the USN/LSN and SAS/LSN studies. Substantial modeling with OEDGE for the USN/LSN study indicates that increasing closure reduces the ionization source in the pedestal. For discharges with matched divertor conditions (ne, Te, Jsat), the pedestal ionization is computed to be about 50% lower for the more closed divertor.

2) For the USN/LSN study, neped shows changes associated with closure. With the same divertor target parameters, the more closed divertor exhibits lower neped than the more open divertor. These changes are associated with a reduction in the pedestal ionization modeled with OEDGE.

3) For the USN/LSN study, the ratio of neped/nesep is lower for a given nesep for the more closed divertor. This is understood as a result of reduction of neutral density in the main chamber for the more closed divertor compared to the more open divertor.

4) Points 2) and 3) show that changes of the density pedestal structure occur with changes in closure and these can be associated with changes in fueling with no obvious need to invoke changes in transport. Identifying the specific mechanisms of particle transport (turbulent, neoclassical, paleoclassical) in the pedestal is the subject of intensive study with numerical simulations.

5) The SAS/LSN studies exhibit changes in pedestal structure associated with changes in divertor configuration when other control parameters are held constant. These results strongly indicate that divertor physics related to fueling plays a significant effect on the pedestal structure. Two of the main observations are that for the $B \times \nabla B$ drift in the unfavorable direction, the closed SAS configuration has a signifcantly higher pedestal pressure than the open LSN divertor. In addition, for the SAS divertor, the pedestal pressure is higher for $B \times \nabla B$ drift in the favorable than in the unfavorable direction. This has also been shown for the LSN discharges also.

6) The pedestal pressure profile is consistent with the predictions of peeling-ballooning PB stability as made with the ELITE code. This is shown both by analysis of SAS and LSN pedestals at the same value of neped and also by time varying changes in pedestal stability as the pedestal evolves during gas scans. These results are not surprising, given the success of the PB theory in explaining many pedestal observations. However, in the context here, it should be recognized that ELM effects due to PB stability limit how far the pedestal can evolve and thus are providing significant density transport.

7) The EPED1 model shows some of its limitations in comparisons with some of the data in the SAS/LSN dataset. The EPED1 model uses some assumptions on profile quantities, such as a fixed ratio of nesep to neped and also assumptions on temperature profiles. When these assumptions are relaxed and the assumed quantities are actually taken from experiment, the predictions of this "full EPED" model with the data are significantly better than for the usual EPED1 predictions. These results demonstrate that while the constraints embodied in the EPED model are important in pedestal structure, additional physics, in particular the transport and particle source effects setting the relationship between the various profiles, is required for a fully predictive model.

8) DIII-D results presented here broadly indicate that the penetration of recycling neutrals into the plasma edge plays a dominant role in determining the H-mode density pedestal height. There is no need to invoke associated modifications to particle transport (diffusion or pinch) to explain these observations; only a low level of particle diffusivity in the edge barrier region, such that the profile responds in rough proportion to the source. The origin of this apparent level of diffusivity and scaling is not fundamentally understood at this time but is under intense study with theory colleagues.

4.5 Conclusions

The results of these studies using divertor closure generally indicate that increasing the particle source in the pedestal causes an increase of pedestal density; there is no compelling need to invoke a particle pinch in order to explain the results. In addition, the studies find changes in pedestal performance where all control parameters are constant except for divertor geometry; this strongly suggests that neutral fuelling effects have a significant impact on pedestal structure. This conclusion is supported by studies of peeling ballooning stability which suggest that neutral fueling differences can impact the achieved pedestal pressure by changing the relative evolution of the density and temperature profiles thereby affecting the evolution of the diamagnetic stabilization and so the pedestal pressure limit. In addition, studies with EPED indicate that additional physics, in particular the transport and source effects, are needed to develop a fully predictive model.

Future work to understand the density pedestal may well use divertor closure as a tool, but it must move beyond that also in several ways. Experimental measurements of the particle source are required. Quantitative knowledge of the source must be coupled with theoretical modeling in order to identify plausible mechanisms for particle transport in the pedestal. With such mechanisms identified, experiment and theory need to work together in order to devise sufficient experimental tests in order to validate models of transport.

5 Conclusions and Future work

5.1 Introduction

During this JRT, progress has been made in identifying various contributions of fueling to the pedestal structure. It is however clear from comparisons of modeling and experiments that much more work in this area is needed. We are only now beginning to grasp how the density pedestal structure will perform in more reactor like conditions.

There are however multiple open questions and issues that still need much more work. Building diagnostics that can measure the neutral density at multiple poloidal locations, since fueling is not poloidally uniform, is going to play a pivotal role in addressing how much neutrals contribute to the pedestal structure in current day devices and how this extrapolates to future devices. SOLPS-ITER simulations indicate that especially in very opaque conditions, there can be large discrepancies between the model and the prior observed neutral densities.

With improved measurements of the neutral densities we can now try and assess the role of transport in determining the pedestal structure. It is clear from the experiments in which the level of opaqueness was increased that a reduction in neutral density inside the pedestal does not result in a reduction of the pedestal electron density. This is an indication that transport plays a role in maintaining this barrier. How much of the particle transport is outward diffusion versus an inward pinch and how these ratios change with various plasma parameters is crucial to predict the pedestal density structure in any future device. Even a small pinch can have positive consequences for the fusion performance in ITER.

DIII-D results where the geometry of the divertor is altered clearly show the impact neutrals have in current day devices in determining the pedestal structure. There is no need to invoke associated modifications to particle transport (diffusion or pinch) to explain these observations; only a low level of particle diffusivity in the edge barrier region, such that the profile responds in rough proportion to the source. The origin of this apparent level of diffusivity and scaling is not fundamentally understood at this time but is under intense study with theory colleagues.

5.2 Neutral measurements

In order to further our understanding of how the edge density pedestal is determined in tokamaks, it is critical to close the loop on the edge ionization source. This has motivated improved experimental characterization of main chamber neutral density and ionization profiles. Such measurements provide both the means to directly evaluate particle fluxes and transport coefficients, but also provide valuable constraints on models of edge neutral transport. As seen above, instrumentation and interpretation of data have advanced considerably in recent years, with concerted effort supporting the goals of this JRT.

The ENDD instrument on NSTX was adapted successfully for use on NSTX-U during its initial campaign, allowing observation of well-resolved profiles of Balmer alpha emission from the NSTX-U plasma edge. These measurements were augmented with passive signals obtained from GPI, and the combined data were inverted to produce radial emissivity profiles. This made possible estimation of the upper bound of edge neutral density, under the assumption that all emission is due to electron impact ionization of atomic deuterium. Simulations using DEGAS2 were used

to validate the interpretation of these data, and demonstrated that the emission observed inside the separatrix was dominated by electron impact ionization as assumed, while emission in the lower temperature SOL is dominated by molecular contributions. Altogether this validation effort indicates that neutral (both atomic and molecular) density profiles can be obtained reliably from the coupled ENDD/DEGAS2 analysis, while radial ionization profiles inside the separatrix can be directly inferred from the ENDD data. This makes possible the evaluation of neutral penetration during changes in plasma confinement and obtained plasma density.

In recent DIII-D experiments supporting this JRT, filterscopes measuring main chamber Balmer alpha were used to provide an estimate of the edge neutral density during gas fueling scans. Future work will improve the interpretation of the filterscopes through application of calibrated geometric factors to the view chords, and through careful evaluation of the spatial and time dependence of local excitation coefficients. Future investigations of main chamber ionization will be augmented significantly by the recent installation of a LFS/HFS Lyman alpha profile diagnostic. Among these and other diagnostics, a fuller picture of the 2D structure of ionization is expected to emerge, and to provide powerful constraints on models of pedestal fueling.

5.3 Neutral opacity

In a series of experiments on DIII-D and C-Mod in which the SOL opacity was increased, we observed that neutral penetration was reduced. The reduction in the penetration of neutrals inside the separatrix did not result in a reduction of the pedestal density, nor did we observe a shift outward, which is often observed at lower opacity and performance. The higher the opacity the less effective additional gas puffing became in raising the pedestal density. SOLPS-ITER simulations show that while X-point fueling is an order of magnitude larger than the fueling at the mid plane, this fueling increase can be very localized over a small area, thus allowing main chamber fueling to play a considerable role.

The neutral density calculations from SOLPS-ITER for DIII-D are close to prior modeling results as well as prior experimental estimates using the filterscope system [20, 88, 74]. However we note that the value calculated at the midplane on C-Mod is approximately 2 orders of magnitude below what has been inferred experimentally in similar discharges [39]. This is closely linked to the need to have an outward particle flux at the core boundary condition in SOLPS-ITER, to increase the total radial particle flux across the separatrix. In DIII-D we found that small changes in recycling can strongly affect the need for such a flux and the neutral density inside the separatrix; however for C-Mod, all recycling values are already set to 1. While none of the simulations had any drifts, the drifts by themselves cannot resolve the 2 orders of magnitude discrepancy between current simulations and prior measurements.

One option to increase the neutral density inside the separatrix for C-Mod is to increase the energy of the neutrals. There is experimental evidence that in metallic wall machines, the energy of the reflected neutrals is higher than in Carbon machines [104]. The higher energy level would result in a deeper penetration depth and the neutrals would not get trapped in the far SOL. Moreover, SOLPS-ITER has mostly been tested in low-opacity discharges and it could well be that the high opacity discharges put a burden on the neutral dynamics simulated by the Monte-Carlo code. This would explain why integrated modeling simulations of ITER using SOLPS-ITER result in very low electron density profiles, without an artificial large core particle flux [81]. This shows yet again the need for developing more capabilities to measure the neutral density at various locations in the

plasma and provide direct data for validation of plasma edge codes, such as SOLPS-ITER.

As can be observed in sections 3 and 4 in current day machines, which operate at low opacity, fueling is a dominant factor in determining the pedestal density structure. To achieve high opaque conditions, we have to increase the SOL density, which affects also divertor conditions. Higher SOL densities also affect the divertor conditions and are linked to the onset of detachment in the outer divertor [54]. These changes in divertor conditions in turn affect the SOL and pedestal conditions [98, 105, 16]. For example, the detachment of the outer divertor will affect the parallel conductivity, which then in turn alters the filamentary and fluctuations behavior in the SOL. The increase in fluctuations is linked to an increase in radial turbulent transport and the formation of a flat spot in the near SOL density profile, also called a shoulder. The shoulder formation itself is very effective at increasing opacity and pushing the ionization front further out into the SOL. All these changes cannot be easily separated and further analysis and modeling is needed to help disentangle the transport from the fueling effects.

There is a strong need to further our understanding of particle transport in the pedestal. From these experiments in more opaque conditions than is usual, it is clear that ionization alone cannot determine the pedestal structure. Ionization plays a dominant role in most of our current day experiments, but when we increase the opacity in these experiments and thus limit the effects of ionization, we still observe a pedestal structure. A validation of edge modeling codes that capture the neutral dynamics is necessary before we couple these components to self-consistent transport simulations. Techniques to measure the transport changes directly using modulated gas puffs will benefit strongly from a much better prediction of the edge fueling source in order to test the separate transport components [65].

5.4 Effect of localization of fueling sources on pedestal structure

In DIII-D scans of particle injection rate were performed using both a core source (pellets) as well as an edge source (gas puffs). Systematic changes were measured for both the pedestal electron temperature and density profiles. For the same fueling rates, core fueling showed higher achieved pedestal electron densities and temperatures than edge fueling. This is in agreement with modeling, which shows that the core fueling provided a much larger source in the pedestal than the edge fueling. In addition, discharges with more edge fueling generally showed a more significant outward shift of the density profile compared to the temperature profile than the discharges with more core fueling. Only at the highest achieved density did the pellet-fueled density display a similar shift.

The increased particle source from gas puffing as well as pellet injection caused a significant increase in ELM frequency as well as a reduction in ELM size (energy loss per ELM). The measured pedestal pressure profiles are consistent with the predictions of peeling-ballooning stability as made with the ELITE code. This is shown for the fueling scans with both more core and more edge fueling. However, in the context here, it should be recognized that ELM effects due to PB stability limit how far the pedestal can evolve and thus are providing significant density transport.

On NSTX-U, two trends are apparent. First, the relationship between the pedestal density and the pedestal density width is opposite to the pedestal gas fueling model [58] described above, where pedestal density width is inversely proportional to the pedestal height. Future work will investigate this observation. While the data has a high degree of scattering, the trend clearly shows that higher pedestal densities correspond to wider density pedestals for all fueling gas injector types (including

SGI), suggesting that the impact of fueling location on NSTX pedestals is not as strong as in other devices.

The second trend is that H-mode discharges without lithium (ELMy) have wider density pedestals than the H-modes with lithium conditioning. This may be related to the pedestal broadening from ELMs in H-modes without lithium, and the shape of carbon contribution to electron density profiles, enhanced with lithium (as shown in Fig. 46). However, in general, neither trend is presently understood.

With respect to the SGI fueling and penetration, the data are scattered and it is not possible to distinguish the SGI from other injectors based on the present analysis. This result could imply that a highly localized gas jet fueling, even if with higher edge neutral penetration, would not necessarily result in a wider density pedestal. It could also imply that the supersonic gas jet penetration (ionization profile) was similar to conventional HFS and LFS gas injection. This could be possible if the supersonic jet was fully penetrated by the ambient SOL plasma leading to molecular dissociation and atomic ionization as in a single particle approximation model rather than the jet acting as a self-shielding fluid jet. Additional experiments are needed to understand these results.

5.5 Divertor closure as a tool to study pedestal structure

Divertor closure (baffling of neutrals) has been used as a tool on DIII-D to study pedestal structure and to address the goals of this milestone. Since divertor closure is strongly affected by divertor geometry, systematic experiments have been performed in different divertor geometries available on DIII-D in order to vary divertor closure and to document and model effects on the pedestal. In particular, systematic comparisons have been made of discharges using the standard high triangularity upper baffled divertor with discharges with the outer strike point on the lower baffle plate to provide relatively closed and open configurations, respectively. Likewise, comparisons have been made of the new closed Small Angle Slot (SAS) divertor with discharges in the more open divertor configuration to provide complementary studies of closed vs open configurations.

Both SOLPS and OEDGE modeling of the first set of the closure experiments indicate that increased closure reduced the pedestal particle source, with other control parameters held constant, and the experimental density profiles showed reductions in pedestal height in these conditions. These results indicate that the magnitude of the pedestal particle source has a clear effect on the pedestal density and there is no strong evidence that changes of transport need to be invoked to observe the response of the pedestal to a change of particle source.

Comparisons of the closed SAS and the open divertor geometries exhibited significant changes in pedestal structure associated with changes in divertor configuration when other control parameters were held constant. These results strongly indicate that divertor physics related to fueling has a significant effect on the pedestal structure in current day devices. In addition, predictions of pedestal height from the standard EPED1 model did not predict these significant variations of pedestal pressure obtained with changes of divertor configuration. However, a more complete EPED model, easing some of the standard constraints by using details of the experimental profiles (such as shift between temperature and density) provided good quantitative agreement with the experimental pressures for the various divertor configurations. These results demonstrate that while the constraints embodied in the EPED model are important in pedestal structure, additional

physics, in particular the transport and source effects setting the relationship between the various profiles, is required for a fully predictive model.

5.6 Overall conclusions and prospects understanding density pedestal

A primary underlying theme of this study was to obtain a better understanding of the physics of the density pedestal in order to better project what the density pedestal will be in ITER. ITER is expected to have an opaque scrape-off layer and to not have significant fuelling from the divertor or scrape-off layer, and there are uncertainties and concerns about what the structure of the density pedestal will be.

The results in this report broadly show that devices with low opacity, primarily NSTX and DIII-D in this study, are able to modify the density pedestal in various ways of fuelling the pedestal. Moreover, some of the results presented here show that the density pedestal is increased by an increase of the particle source in the pedestal. In contrast, experiments in C-Mod reached high neutral opacities, near those expected on ITER. At these high opacities, C-Mod found that the density pedestal did not increase with increases of gas puffing, as would be expected for an opaque SOL. Nevertheless, the density profile had a very significant gradient in the pedestal, similar to typical H-mode operation. This observation is contrary to the weak density pedestal expected by many for ITER.

We believe that the work presented here represents significant steps in the characterization and understanding of the density pedestal, but predictive capability remains a challenge. One need for predictive capability is to have confidence in what ITER's density pedestal will look like. As is well known, but emphasized in the report, is that a predictive capability of the source requires measurements of the particle source in the pedestal and an understanding of the pedestal particle transport. These are extremely difficult problems and increasing attention is being devoted to them throughout the international community as well as in the US program. NSTX-U and DIII-D are implementing diagnostics to measure neutral densities in the pedestal. These efforts are highly important steps and provide some prospect that a much better quantitative understanding of the particle source for the pedestal will ultimately emerge. The source is needed in order to validate theoretical models for the pedestal density. At this time, knowledge of the transport is poor. The main candidates for transport in the absence of MHD effects are neoclassical transport and fluctuation-driven transport. In addition, 3D effects such as ELMs or applied magnetic perturbations cause particle transport. The modeling capability in the US and world wide to study much of this physics is markedly improving, as shown by advances in gyrokinetic, neoclassical and extended MHD codes and applications of these codes to the pedestal. The prospects for making important advances in understanding the density pedestal are improving rapidly.

Acknowledgements

This report was only possible due to the many contributions of the DIII-D, NSTX-U and Alcator C-Mod teams. This material is based upon work supported by the U.S. Department of Energy, Office of Science, Office of Fusion Energy Sciences, using the DIII-D National Fusion Facility, a DOE Office of Science user facility, under Award DE-FC02-04ER54698; using Alcator C-Mod, a DOE Office of Science user facility, under Award DE-FC02-99ER54512; and using NSTX and NSTX-U, a DOE Office of Science user facility, under Award DE-AC02-09CH11466. Additional work was supported under DOE grants DE-SC0014264, DE-SC0007880, DE-SC0019302, H11466, DE-SC0014264, DE-SC0007880, DE-SC0019302, DE-AC05-00OR22725, DE-AC52-07NA27344.

Disclaimer

References

[1] S. Allen, J. Boedo, A. Bozek, N. Brooks, T. Carlstrom, T. Casper, R. Colchin, T. Evans, M. Fenstermacher, M. Friend, R. Isler, R. Jayakumar, C. Lasnier, A. Leonard, M. Mahdavi, R. Maingi, G. McKee, R. Moyer, M. Murakami, T. Osborne, R. O'Neill, T. Petrie, G. Porter, A. Ramsey, M. Schaffer, P. Stangeby, R. Stambaugh, M. Wade, J. Watkins, W. West, D. Whyte, and N. Wolf. Experiments and computational modeling focused on divertor and SOL optimization for advanced tokamak operation on DIII-D. *Journal of Nuclear Materials*, 290-293:995–1001, 2001.

[2] S. Allen, N. Brooks, R. Bastasz, J. Boedo, J. Brooks, J. Cuthbertson, T. Evans, M. Fenstermacher, D. Hill, D. Hillis, J. Hogan, A. Hyatt, R. Isler, G. Jackson, T. Jernigan, C. Lasnier, R. Lehmer, A. Leonard, M. Mahdavi, R. Maingi, W. Meyer, P. Mioduszewski, R. Moyer, D. Nilson, L. Owen, T. Petrie, G. Porter, M. Rensink, M. Schaffer, J. Smith, G. Staebler, R. Stambaugh, D. Thomas, M. Wade, W. Wampler, J. Watkins, W. West, D. Whyte, N. Wolf, C. Wong, R. Wood, D. Physics, and O. Teams. Radiative divertor and scrape-off layer experiments in open and baffled divertors on DIII-D. *Nuclear Fusion*, 39(11Y):2015–2023, nov 1999.

[3] N. Asakura, N. Hosogane, K. Itami, A. Sakasai, S. Sakurai, K. Shimizu, M. Shimada, H. Kubo, S. Higashijma, H. Takenaga, H. Tamai, S. Konoshima, T. Sugie, K. Masaki, Y. Koide, O. Naito, H. Shirai, T. Takizuka, T. Ishijima, S. Suzuki, and A. Kumagai. Role of divertor geometry on detachment and core plasma performance in JT60U. *Journal of Nuclear Materials*, 266-269:182 – 188, 1999.

[4] S. C. Bates and K. H. Burrell. Fast gas injection system for plasma physics experiments. *Rev. Sci. Instrum.*, 55(6):934, 1984.

[5] D. J. Battaglia, M. D. Boyer, S. P. Gerhardt, D. Mueller, C. E. Myers, W. Guttenfelder, J. E. Menard, S. A. Sabbagh, F. Scotti, F. Bedoya, R. E. Bell, J. Berkery, A. Diallo, N. Ferraro, S. M. Kaye, M. A. Jaworski, B. P. LeBlanc, M. Ono, J.-K. Park, M. Podesta, R. Raman, and V. Soukhanovskii. Scenario development during commissioning operations on the national spherical torus experiment upgrade. *Nuclear Fusion*, 2018.

[6] L. R. Baylor, T. C. Jernigan, R. J. Colchin, G. L. Jackson, L. W. Owen, and T. W. Petrie. Comparison of fueling efficiency from different fueling locations on DIII-D. *Journal of Nuclear Materials*, 313-316:530–533, 2003.

[7] E. Belli, J. Candy, O. Meneghini, and T. Osborne. Limitations of bootstrap current models. *Plasma Phys. Control. Fusion*, 56:045006, 2014.

[8] M. N. A. Beurskens, T. H. Osborne, P. A. Schneider, E. Wolfrum, L. Frassinetti, R. Groebner, P. Lomas, I. Nunes, S. Saarelma, R. Scannell, P. B. Snyder, D. Zarzoso, I. Balboa, B. Bray, M. Brix, J. Flanagan, C. Giroud, E. Giovannozzi, M. Kempenaars, A. Loarte, E. de la Luna, G. Maddison, C. F. Maggi, D. McDonald, R. Pasqualotto, G. Saibene, R. Sartori, E. R. Solano, M. Walsh, and L. Zabeo. H-mode pedestal scaling in DIII-D, ASDEX upgrade, and JET. *Physics of Plasmas*, 18(5):056120, 2011.

[9] R. L. Boivin, J. A. Goetz, A. E. Hubbard, J. W. Hughes, I. H. Hutchinson, J. H. Irby, B. LaBombard, E. S. Marmar, D. Mossessian, C. S. Pitcher, J. L. Terry, B. A. Carreras, and

L. W. Owen. Effects of neutral particles on edge dynamics in alcator c-mod plasmas. *Physics of Plasmas*, 7(5):1919–1926, 2000.

[10] R. L. Boivin, J. W. Hughes, B. LaBombard, D. Mossessian, and J. L. Terry. High resolution measurements of neutral density and ionization rate in the alcator C-Mod tokamak. *Review of Scientific Instruments*, 72(1):961–964, 2001.

[11] X. Bonnin, W. Dekeyser, R. Pitts, D. Coster, S. Voskoboynikov, and S. Wiesen. Presentation of the new SOLPS-ITER code package for tokamak plasma edge modelling. *Plasma and Fusion Research*, 11, 08 2016.

[12] B. Braams. *Computational studies in tokamak equilibrium and transport*. PhD thesis, Rijksuniversiteit Utrecht, 1986.

[13] B. Braams. A multi-fluid code for simulation of the edge plasma in tokamaks. Technical Report EUR-FU/XII-80/87/68, Next European Torus (NET) report, 1987.

[14] J. Breslau, M. Gorelenkova, F. Poli, J. Sachdev, and X. Yuan. Transp. Technical Report https://dx.doi. org/10.11578/dc.20180627.4, Princeton Plasma Physics Laboratory, 2018.

[15] K. Burrell. Fast hydrogen gas injection system for plasma physics experiments. *Review of Scientific Instruments*, 49(7):948–954, 1978.

[16] D. Carralero, M. Siccinio, M. Komm, S. Artene, F. Isa, J. Adamek, L. Aho-Mantila, G. Birkenmeier, M. Brix, G. Fuchert, M. Groth, T. Lunt, P. Manz, J. Madsen, S. Marsen, H. Mller, U. Stroth, H. Sun, N. Vianello, M. Wischmeier, E. Wolfrum, A. U. Team, C. Team, J. Contributors, and T. E. M. Team. Recent progress towards a quantitative description of filamentary SOL transport. *Nuclear Fusion*, 57(5):056044, 2017.

[17] L. Casali, B. Covele, and H. Guo. The effect of neutrals in the new sas divertor at DIII-D as modelled by SOLPS. *Nuclear Materials and Energy*, 19:537 – 543, 2019.

[18] L. Casali, C. Sang, A. Moser, B. Covele, H. Guo, and C. Samuell. Modelling the effect of divertor closure on detachment onset in DIII-D with the SOLPS code. *Contrib. Plasma Phys*, 58:725731, 2018.

[19] R. Colchin, R. Maingi, M. Fenstermacher, T. Carlstrom, R. Isler, L. Owen, and R. Groebner. Measurement of neutral density near the X point in the DIII-D tokamak. *Nuclear Fusion*, 40(2):175–180, feb 2000.

[20] R. Colchin and L. Owen. Neutral particle fueling at the midplane of DIII-D. *Journal of Nuclear Materials*, 313-316:609 – 613, 2003. Plasma-Surface Interactions in Controlled Fusion Devices 15.

[21] R. J. Colchin, D. L. Hillis, R. Maingi, C. C. Klepper, and N. H. Brooks. The filterscope. *Review of Scientific Instruments*, 74(3):2068–2070, 2003.

[22] A. Dominguez. *Study of Density Fluctuations and Particle Transport at the Edge of I-Mode Plasmas*. PhD thesis, Massachusetts Institue of Technology, 2012.

[23] M. G. Dunne, S. Potzel, F. Reimold, M. Wischmeier, E. Wolfrum, L. Frassinetti, M. Beurskens, P. Bilkova, M. Cavedon, R. Fischer, B. Kurzan, F. M. Laggner, R. M. McDermott, G. Tardini, E. Trier, E. Viezzer, and M. Willensdorfer. The role of the density profile in the ASDEX-upgrade pedestal structure. *Plasma Physics and Controlled Fusion*, 59(1):014017, 2017.

[24] H. Dylla, M. Bell, R. Fonck, K. Jaehnig, S. Kaye, D. Owens, D. Heifetz, and G. Schmidt. Gas fueling studies in the pdx tokamak: Ii. *J. Nucl. Mater.*, 121:144, 1984.

[25] H. Dylla, W. Blanchard, R. Budny, R. Fonck, D. Owens, and G. Schmidt. Gas-fueling studies in the pdx tokamak. *J. Nucl. Mater.*, 111-112:211, 1982.

[26] I. C. Faust, D. Brunner, B. LaBombard, R. R. Parker, J. L. Terry, D. G. Whyte, S. G. Baek, E. Edlund, A. E. Hubbard, J. W. Hughes, A. Q. Kuang, M. L. Reinke, S. Shiraiwa, G. M. Wallace, and J. R. Walk. Lower hybrid wave edge power loss quantification on the alcator C-Mod tokamak. *Physics of Plasmas*, 23(5):056115, 2016.

[27] M. E. Fenstermacher, A. W. Leonard, P. B. Snyder, J. A. Boedo, N. H. Brooks, R. J. Colchin, D. S. Gray, R. J. Groebner, M. Groth, E. Hollmann, C. J. Lasnier, T. H. Osborne, T. W. Petrie, D. L. Rudakov, H. Takahashi, J. G. Watkins, L. Zeng, and the DIII-D Team. ELM particle and energy transport in the SOL and divertor of DIII-D. *Plasma Physics and Controlled Fusion*, 45(9):1597–1626, aug 2003.

[28] Z. W. Friis, W. M. Stacey, A. W. Leonard, and M. Rensink. Analysis of neutral particle recycling and pedestal fueling in a H-mode DIII-D discharge. *Physics of Plasmas (1994-present)*, 17(2):022507, 2010.

[29] M. J. Gouge. Fueling of iter-scale fusion plasmas. *Fusion Technology*, 34(3P2):435, 1998.

[30] C. Grisolia, P. Ghendrih, B. Pégourié, and A. Grosman. Plasma wall particle balance in tore supra. *J. Nucl. Mater.*, 196-198:281, 1992.

[31] R. Groebner, M. Mahdavi, A. Leonard, T. Osborne, N. Wolf, G. Porter, P. Stangeby, N. Brooks, R. Colchin, and L. Owen. Comparison of H-mode barrier width with a model of neutral penetration length. *Nuclear Fusion*, 44(1):204, 2004.

[32] R. J. Groebner and T. N. Carlstrom. Critical edge parameters for H-mode transition in DIII-D. *Plasma Physics and Controlled Fusion*, 40(5):673–677, 1998.

[33] H. Guo, C. Sang, P. Stangeby, L. Lao, T. Taylor, and D. Thomas. Small angle slot divertor concept for long pulse advanced tokamaks. *Nuclear Fusion*, 57:044001, 2018.

[34] W. Houlberg, S. Milora, and S. Attenberger. Neutral and plasma shielding model for pellet ablation. *Nuclear Fusion*, 28(4):595–610, apr 1988.

[35] J. Hughes, A. Hubbard, G. Wallace, M. Greenwald, B. LaBombard, L. Lin, R. McDermott, R. Parker, M. Reinke, J. Rice, and J. Wilson. Modification of H-mode pedestal structure with lower hybrid waves on alcator C-Mod. *Nuclear Fusion*, 50(6):064001, may 2010.

[36] J. Hughes, B. LaBombard, J. Terry, A. Hubbard, and B. Lipschultz. Edge profile stiffness and insensitivity of the density pedestal to neutral fuelling in alcator C-Mod edge transport barriers. *Nuclear Fusion*, 47(8):1057, 2007.

[37] J. Hughes, A. Loarte, M. Reinke, J. Terry, D. Brunner, M. Greenwald, A. Hubbard, B. LaBombard, B. Lipschultz, Y. Ma, S. Wolfe, and S. Wukitch. Power requirements for superior H-mode confinement on alcator C-Mod: experiments in support of ITER. *Nuclear Fusion*, 51(8):083007, jun 2011.

[38] J. Hughes, P. Snyder, M. Reinke, B. LaBombard, S. Mordijck, S. Scott, E. Tolman, S. Baek, T. Golfinopoulos, R. Granetz, M. Greenwald, A. Hubbard, E. Marmar, J. Rice, A. White,

D. Whyte, T. Wilks, and S. Wolfe. Access to pedestal pressure relevant to burning plasmas on the high magnetic field tokamak alcator C-Mod. *Nuclear Fusion*, 58(11):112003, sep 2018.

[39] J. W. Hughes, B. LaBombard, D. A. Mossessian, A. E. Hubbard, J. Terry, T. Biewer, and the Alcator C-Mod Team. Advances in measurement and modeling of the high-confinement-mode pedestal on the alcator C-Mod tokamak. *Physics of Plasmas*, 13(5):056103, 2006.

[40] ITER Physics Expert Group on Divertor and ITER Physics Expert Group on Divertor Modelling and Database and ITER Physics Basis Editors. Chapter 4: Power and particle control. *Nucl. Fusion*, 39(12):2391, 1999.

[41] J.D.Elder, P.C.Stangeby, T.Abrams, R.Ding, A.W.Leonard, A.G.McLean, D.L.Rudakov, E.A.Unterberg, and J.G.Watkins. OEDGE modeling for the planned tungsten ring experiment on DIII-D. *Nuclear Materials and Energy*, 12:755–761, 2017.

[42] A. Kallenbach, D. Coster, J. C. Fuchs, H. Y. Guo, G. Haas, A. Herrmann, L. D. Horton, L. C. Ingesson, C. F. Maggi, G. F. Matthews, R. D. Monk, J. Neuhauser, F. Ryter, J. Schweinzer, J. Stober, W. Suttrop, A. U. Team, and J. Team. Closed divertor operation in ASDEX upgrade and JET. *Plasma Physics and Controlled Fusion*, 41(12B):B177–B189, 1999.

[43] A. Kallenbach, M. Kaufmann, D. Coster, J. Fuchs, A. Herrmann, J. Neuhauser, R. Schneider, K. Borrass, H.-S. Bosch, A. Carlson, J. Gafert, K. Lackner, K. Schmidtmann, J. Schweinzer, W. Suttrop, U. Wenzel, and A. U. Team. Scrape-off layer radiation and heat load to the ASDEX upgrade LYRA divertor. *Nuclear Fusion*, 39(7):901–917, jul 1999.

[44] A. Kirk, T. Gorman, S. Saarelma, R. Scannell, and H. R. W. and. A comparison of H-mode pedestal characteristics in MAST as a function of magnetic configuration and ELM type. *Plasma Physics and Controlled Fusion*, 51(6):065016, may 2009.

[45] S. I. Krasheninnikov, A. Y. Pigarov, T. K. Soboleva, and D. L. Rudakov. Strongly intermittent edge plasma transport: Issues with modeling and interpretation of experimental data. *Physics of Plasmas*, 16(1):014501, 2009.

[46] H. W. Kugel, M. Anderson, G. Barnes, M. Bell, W. Blanchard, L. Dudek, D. Gates, R. Gernhardt, R. Maingi, D. Mueller, T. Provost, R. Raman, V. Soukhanovskii, and J. Winston. NSTX high field side gas fueling system. In *20th IEEE/NPSS Symposium on Fusion Engineering, 2003.*, pages 82–85, Oct 2003.

[47] B. LaBombard, J. W. Hughes, N. Smick, A. Graf, K. Marr, R. McDermott, M. Reinke, M. Greenwald, B. Lipschultz, J. L. Terry, D. G. Whyte, and S. J. Zweben. Critical gradients and plasma flows in the edge plasma of alcator C-Mod. *Physics of Plasmas*, 15(5):056106, 2008.

[48] B. LaBombard, M. Umansky, R. Boivin, J. Goetz, J. Hughes, B. Lipschultz, D. Mossessian, C. Pitcher, J. Terry, and A. Group. Cross-field plasma transport and main-chamber recycling in diverted plasmas on alcator C-Mod. *Nuclear Fusion*, 40(12):2041–2060, dec 2000.

[49] B. P. LeBlanc, R. E. Bell, D. W. Johnson, D. E. Hoffman, D. C. Long, and R. W. Palladino. Operation of the NSTX thomson scattering system. *Rev. Sci. Instrum.*, 74(3):1659, 2003.

[50] K. C. Lee, C. W. Domier, B. H. Deng, M. Johnson, B. R. Nathan, N. C. Luhmann, and H. Park. A stark-tuned laser application for interferometry and polarimetry on the national spherical torus experiment. *Rev. Sci. Instrum.*, 74(3):1621, 2003.

[51] A. Leonard, J. Elder, R. Groebner, M. Makowski, A. McLean, A. Moser, T. Osborne, and P. Stangeby. Robust H-mode pedestal compatibility with SOL and divertor plasma constraints. In *26 ^{t}h IAEA Fusion Energy Conference (FEC 2016)*, 2016.

[52] A. Leonard, M. Makowski, T. Osborne, and P. Snyder. Compatibility of detached divertor operation with robust edge pedestal performance. *Journal of Nuclear Materials*, 463:519, 2015.

[53] A. W. Leonard. Edge-localized-modes in tokamaks. *Physics of Plasmas*, 21(9):090501, 2014.

[54] A. W. Leonard. Plasma detachment in divertor tokamaks. *Plasma Physics and Controlled Fusion*, 60(4):044001, 2018.

[55] B. Lipschultz, J. Goetz, I. Hutchinson, B. LaBombard, G. McCracken, Y. Takase, J. Terry, P. Bonoli, S. Golovato, P. O'Shea, M. Porkolab, R. Boivin, F. Bombarda, C. Fiore, D. Garnier, R. Granetz, M. Greenwald, S. Horne, A. Hubbard, J. Irby, E. Marmar, M. May, A. Mazurenko, J. Reardon, J. Rice, C. Rost, J. Schachter, J. Snipes, P. Stek, R. Watterson, J. Weaver, B. Welch, and S. Wolfe. Variation of the divertor geometry in alcator C-Mod. In 16^{th} *International Conference on Plasma Physics and Controlled Nuclear Fusion Research, Montreal, 7-11 October 1996*, 1996.

[56] S. Lisgo, P. Stangeby, J. Elder, J. Boedo, B. Bray, N. Brooks, M. Fenstermacher, M. Groth, D. Reiter, D. Rudakov, J. Watkins, W. West, and D. Whyte. Re-construction of detached divertor plasma conditions in DIII-D using spectroscopic and probe data. *Journal of Nuclear Materials*, 337339:256260, 2005.

[57] A. Loarte. Effects of divertor geometry on tokamak plasmas. *Plasma Physics and Controlled Fusion*, 43(6):R183, 2001.

[58] M. A. Mahdavi, R. Maingi, R. J. Groebner, A. W. Leonard, T. H. Osborne, and G. Porter. Physics of pedestal density profile formation and its impact on H-mode density limit in burning plasmas. *Physics of Plasmas*, 10(10):3984–3991, 2003.

[59] R. Maingi, M. Bell, R. Bell, C. Bush, E. Fredrickson, D. Gates, T. Gray, D. Johnson, R. Kaita, S. Kaye, S. Kubota, H. Kugel, C. Lasnier, B. LeBlanc, R. Maqueda, D. Mastrovito, J. Menard, D. Mueller, M. Ono, F. Paoletti, S. Paul, Y.-K. Peng, A. Roquemore, S. Sabbagh, C. Skinner, V. Soukhanovskii, D. Stutman, D. Swain, E. Synakowski, T. Tan, J. Wilgen, and S. Zweben. H-mode research in NSTX. *Nuc. Fusion*, 43(9):969–974, 2003.

[60] R. Maingi, C. S. Chang, S. Ku, T. Biewer, R. Maqueda, M. Bell, R. Bell, C. Bush, D. Gates, S. Kaye, H. Kugel, B. LeBlanc, J. Menard, D. Mueller, R. Raman, S. Sabbagh, V. Soukhanovskii, and the NSTX Team. Effect of gas fuelling location on H-mode access in NSTX. *Plasma Phys. Control. Fusion*, 46(5A):A305, 2004.

[61] R. Maingi, T. H. Osborne, B. P. LeBlanc, R. E. Bell, J. Manickam, P. B. Snyder, J. E. Menard, D. K. Mansfield, H. W. Kugel, R. Kaita, S. P. Gerhardt, S. A. Sabbagh, and F. A. Kelly. Edge-localized-mode suppression through density-profile modification with lithium-wall coatings in the national spherical torus experiment. *Phys. Rev. Lett.*, 103:075001, Aug 2009.

[62] G. McCracken, U. Samm, P. Stangeby, G. Bertschinger, J. Boedo, S. Davies, D. Gray, V. Philipps, R. Pitts, D. Goodall, A. Pospieszczyk, R. Schorn, B. Schweer, G. Telesca, B. Un-

terberg, and G. Waidmann. Experimental measurements of the fuelling efficiency of impurities injected into TEXTOR. *Nuclear Fusion*, 33(10):1409, 1993.

[63] O. Meneghini, S. Smith, P. Snyder, G. Staebler, J. Candy, E. Belli, M. K. L. Lao1, T. Luce, T. Luda, J. Park, and F. Poli. Self-consistent core-pedestal transport simulations with neural network accelerated models. *Nuclear Fusion*, 57:086034, 2017.

[64] S. Mordijck, P. Kress, R. Groebner, T. Osborne, J. Hughes, T. Terry, A. Jrvinen, A. Salmi, T. Tala, M. Shafer, F. Laggner, G. McKee, R. Moyer, and L. Zeng. Particle transport from the bottom up. In *27 ^{t}h IAEA Fusion Energy Conference (FEC 2017)*, 2018.

[65] S. Mordijck, T. Rhodes, L. Zeng, A. Salmi, T. Tala, C. Petty, G. McKee, F. Eriksson, E. Fransson, and H. Nordman. Collisionality driven turbulent particle transport changes in DIII-D H-mode plasmas. *Nuclear Fusion*, To be submitted, 2019.

[66] S. Mordijck, X. Wang, E. J. Doyle, T. L. Rhodes, L. Schmitz, L. Zeng, G. M. Staebler, C. C. Petty, R. J. Groebner, W. H. Ko, B. A. Grierson, W. M. Solomon, T. Tala, A. Salmi, C. Chrystal, P. H. Diamond, and G. R. Mckee. Particle transport in low-collisionality H-mode plasmas on DIII-D. *Nuclear Fusion*, 55(11), 2015.

[67] A. Moser, L. Casali, B. Covele, A. Leonard, A. McLean, M. Shafer, H. Wang, and J. Watkins. Effects of divertor geometry on H-mode pedestal structure near divertor detachment in the DIII-D tokamak. *submitted for publication*, 2019.

[68] A. Moser, A. Leonard, A. McLean, H. Wang, and J. Watkins. The effect of divertor closure on detachment onset in DIII-D. *Nuclear Materials and Energy*, 19:67–71, 2019.

[69] T. Nakano, N. Asakura, H. Takenaga, H. Kubo, Y. Miura, K. Shimizu, S. Konoshima, K. Masaki, S. Higashijima, and the JT-60Team. Impact of wall saturation on particle control in long and high-power-heated discharges in JT-60u. *Nuclear Fusion*, 46(5):626–634, apr 2006.

[70] A. O. Nelson, F. M. Laggner, R. Groebner, B. A. Grierson, O. Izacard, D. Eldon, M. W. Shafer, A. Leonard, D. Shiraki, A. C. Sontag, E. Kolemen, and the DIII-D Team. Setting the H-mode pedestal structure: variations of particle source location using gas puff and pellet fueling. *to be submitted for publication*, 2019.

[71] T. Osborne, L. Casali, H. Guo, A. Moser, and S. M. Comparison of H-mode pedestal characteristics in SAS and open divertor configurations on DIII-D. *Proceedings of the 46th European Physical Society Conference on Plasma Physics (Milan 2019)*, 43C:P5.1035, 2019.

[72] T. Osborne, L. Casali, H. Guo, A. Moser, and S. M. Comparison of H-mode pedestal characteristics in SAS and open divertor configurations on DIII-D. Poster at 2019 EPS conference, Milan, Italy, July 8-12, 2019, 2019.

[73] T. Osborne, G. Jackson, Z. Yan, R. Maingi, D. Mansfield, B. Grierson, C. Chrobak, A. McLean, S. Allen, D. Battaglia, A. Briesemeister, M. Fenstermacher, G. McKee, and P. S. and. Enhanced H-mode pedestals with lithium injection in DIII-D. *Nuclear Fusion*, 55(6):063018, may 2015.

[74] L. Owen, J. Canik, R. Groebner, J. Callen, X. Bonnin, and T. Osborne. Comparing 1.5d ONETWO and 2d SOLPS analyses of inter-ELM H-mode plasma in DIII-D. *Nuclear Fusion*, 50(6):064017, may 2010.

[75] W. Pfeiffer and et al. ONETWO: a computer code for modeling plasma transport in tokamaks. Technical Report GA-A16178, General Atomics Company Report, 1980.

[76] G. D. Porter, T. A. Casper, and J. M. Moller. Edge localized mode particle losses from the DIII-D tokamak. *Physics of Plasmas*, 8(12):5140–5150, 2001.

[77] J. T. (prepared by R.D Monk). Recent results from divertor and scrape-off layer studies at JET. *Nuclear Fusion*, 39(11Y):1751–1762, nov 1999.

[78] F. Reimold, M. Wischmeier, S. Potzel, L. Guimarais, D. Reiter, M. Bernert, M. Dunne, and T. Lunt. The high field side high density region in SOLPS-modeling of nitrogen-seeded H-modes in ASDEX upgrade. *Nuclear Materials and Energy*, 12:193 – 199, 2017. Proceedings of the 22nd International Conference on Plasma Surface Interactions 2016, 22nd PSI.

[79] D. Reiter. The eirene code user manual. Technical Report http://www.eirene.de/, Institut fur Energie- und Klimaforschung Plasmaphysik Forschungszentrum Julich GmbH, 2009.

[80] T. Rognlien, J. Milovich, M. Rensink, and G. Porter. A fully implicit, time dependent 2-D fluid code for modeling tokamak edge plasmas. *Journal of Nuclear Materials*, 196-198:347 – 351, 1992. Plasma-Surface Interactions in Controlled Fusion Devices.

[81] M. Romanelli, V. Parail, P. da Silva Aresta Belo, G. Corrigan, L. Garzotti, D. Harting, F. Koechl, E. Militello-Asp, R. Ambrosino, M. Cavinato, A. Kukushkin, A. Loarte, M. Mattei, and R. Sartori. Modelling of plasma performance and transient density behaviour in the h-mode access for ITER gas fuelled scenarios. *Nuclear Fusion*, 55(9):093008, 2015.

[82] A. M. Rosenthal, J. W. Hughes, A. Bortolon, F. Laggner, and T. M. Wilks. A lyman-alpha camera for neutral studies of the pedestal region on the DIII-D tokamak. *in preparation*, 2019.

[83] D. Rudakov, J. Boedo, R. Moyer, P. Stangeby, J. Watkins, D. Whyte, L. Zeng, N. Brooks, R. Doerner, T. Evans, M. Fenstermacher, M. Groth, E. Hollmann, S. Krasheninnikov, C. Lasnier, A. Leonard, M. Mahdavi, G. McKee, A. McLean, A. Pigarov, W. Wampler, G. Wang, W. West, and C. Wong. Far SOL transport and main wall plasma interaction in DIII-D. *Nuclear Fusion*, 45(12):1589–1599, nov 2005.

[84] C. Sang, H. Guo, P. Stangeby, L. Lao, and T. Taylor. SOLPS analysis of neutral baffling for the design of a new diverter in DIII-D. *Nuclear Fusion*, 57:056043, 2018.

[85] P. Snyder, R. Groebner, J. Hughes, T. Osborne, M. Beurskens, A. Leonard, H. Wilson, and X. Xu. A first-principles predictive model of the pedestal height and width: development, testing and ITER optimization with the EPED model. *Nuclear Fusion*, 51(10):103016, 2011.

[86] P. B. Snyder, R. J. Groebner, A. W. Leonard, T. H. Osborne, and H. R. Wilson. Development and validation of a predictive model for the pedestal height. *Physics of Plasmas*, 16:056118, 2009.

[87] P. B. Snyder, H. R. Wilson, J. R. Ferron, L. L. Lao, A. W. Leonard, T. H. Osborne, A. D. Turnbull, D. Mossessian, M. Murakami, and X. Q. Xu. Edge localized modes and the pedestal: A model based on coupled peeling - ballooning modes. *Physics of Plasmas*, 9:2037–2043, 2002.

[88] A. Sontag, X. Chen, J. Canik, A. Leonard, J. Lore, A. Moser, M. Murakami, J. Park, and C. Petty. SOL effects on the pedestal structure in DIII-D discharges. *Nuclear Fusion*, 57:076025, 2017.

[89] V. Soukhanovskii, W. Blanchard, J. Dong, R. Kaita, H. Kugel, J. Menard, T. Provost, R. Raman, A. Roquemore, and P. Sichta. Supersonic gas injector for plasma fueling in the national spherical torus experiment. *Fusion Science and Technology*, 75(1):1, 2019.

[90] V. Soukhanovskii, H. Kugel, R. Kaita, R. Majeski, and A. Roquemore. Supersonic gas injector for fueling and diagnostic applications on the national spherical torus experiment. *Rev. Sci. Instrum.*, 75(10 II):4320, 2004.

[91] P. C. Stangeby, J. M. Canik, J. D. Elder, C. J. Lasnier, A. W. Leonard, D. Eldon, M. A. Makowski, T. H. Osborne, and B. A. Grierson. Identifying the location of the omp separatrix in DIII-D using power accounting. *Nuclear Fusion*, 55(9):093014, 2015.

[92] E. Stefanikova, L. Frassinetti, S. Saarelma, A. Loarte, I. Nunes, L. Garzotti, P. Lomas, F. Rimini, P. Drewelow, U. Kruezi, B. Lomanowski, E. de la Luna, L. Meneses, M. Peterka, B. Viola, C. Giroud, and C. Maggi. Effect of the relative shift between the electron density and temperature pedestal position on the pedestal stability in JET-ILW and comparison with JET-C. *Nuclear Fusion*, 58(5), 2018.

[93] D. P. Stotler and C. Karney. Neutral gas transport modeling with DEGAS2. *Contrib. Plasma Phys.*, 34:392–397, 1994.

[94] D. P. Stotler, F. Scotti, R. E. Bell, A. Diallo, B. P. LeBlanc, M. Podesta, A. L. Roquemore, and P. W. Ross. Midpdata neutral density profiles in the national spherical torus experiments. *Phys. Plasmas*, 22:082506, 2015.

[95] D. P. Stotler, F. Scotti, R. E. Bell, B. P. LeBlanc, and R. Raman. Reconstruction of nstx midplane neutral density profiles from visible imaging data. *J. Nucl. Mater.*, 463:897–901, 2015.

[96] J. Terry, N. Basse, I. Cziegler, M. Greenwald, O. Grulke, B. LaBombard, S. Zweben, E. Edlund, J. Hughes, L. Lin, Y. Lin, M. Porkolab, M. Sampsell, B. Veto, and S. Wukitch. Transport phenomena in the edge of alcator C-Mod plasmas. *Nuclear Fusion*, 45(11):1321–1327, oct 2005.

[97] G. M. Wallace, I. C. Faust, O. Meneghini, R. R. Parker, S. Shiraiwa, S. G. Baek, P. T. Bonoli, A. E. Hubbard, J. W. Hughes, B. L. LaBombard, C. Lau, Y. Ma, M. L. Reinke, J. L. Terry, D. G. Whyte, J. C. Wright, S. J. Wukitch, R. W. Harvey, A. E. Schmidt, A. P. Smirnov, and J. R. Wilson. Lower hybrid current drive at high density in the multi-pass regime. *Physics of Plasmas*, 19(6):062505, 2012.

[98] H. Wang, H. Guo, A. Leonard, A. Moser, T. Osborne, P. Snyder, E. Belli, R. Groebner, D. Thomas, J. Watkins, Z. Yan, and the DIII-D group. Effects of divertor geometry on H-mode pedestal structure in attached and detached plasmas in the DIII-D tokamak. *Nuclear Fusion*, 58(9):096014, 2018.

[99] H. Q. Wang, H. Y. Guo, A. W. Leonard, A. L. Moser, T. H. Osborne, P. B. Snyder, E. Belli, L. Casali, R. J. Groebner, M. Groth, A. Jaervinen, A. C. Sontag, D. M. Thomas, J. G. Watkins, Z. Yan, and the DIII-D group. Separating divertor closure effects in the SOL and pedestal in DIII-D. Presented at 2018 PSI, Princeton, NJ, June 1722, 2018, 2018.

[100] X. Wang, S. Mordijck, E. J. Doyle, T. L. Rhodes, L. Zeng, G. R. McKee, M. E. Austin, O. Meneghini, G. M. Staebler, and S. P. Smith. Understanding ech density pump-out in DIII-D H-mode plasmas. *Nuclear Fusion*, 57(11), 2017.

[101] D. G. Whyte, B. L. Lipschultz, P. C. Stangeby, J. Boedo, D. L. Rudakov, J. G. Watkins, and W. P. West. The magnitude of plasma flux to the main-wall in the DIII-D tokamak. *Plasma Physics and Controlled Fusion*, 47(10):1579–1607, sep 2005.

[102] S. Wiesen, D. Reiter, V. Kotov, M. Baelmans, W. Dekeyser, A. Kukushkin, S. Lisgo, R. Pitts, V. Rozhansky, G. Saibene, I. Veselova, and S. Voskoboynikov. The new SOLPS-ITER code package. *Journal of Nuclear Materials*, 463:480 – 484, 2015.

[103] M. Willensdorfer, E. Wolfrum, A. Scarabosio, F. Aumayr, R. Fischer, B. Kurzan, R. McDermott, A. Mlynek, B. Nold, S. Rathgeber, et al. Electron density evolution after L–H transitions and the L–H/H–L cycle in ASDEX Upgrade. *Nuclear Fusion*, 52(11):114026, 2012.

[104] E. Wolfrum, M. Beurskens, M. Dunne, L. Frassinetti, X. Gao, C. Giroud, J. Hughes, T. Lunt, R. Maingi, T. Osborne, M. Reinke, and H. Urano. Impact of wall materials and seeding gases on the pedestal and on core plasma performance. *Nuclear Materials and Energy*, 12:18 – 27, 2017. Proceedings of the 22nd International Conference on Plasma Surface Interactions 2016, 22nd PSI.

[105] A. Wynn, B. Lipschultz, I. Cziegler, J. Harrison, A. Jaervinen, G. F. Matthews, J. Schmitz, B. Tal, M. Brix, C. Guillemaut, D. Frigione, A. Huber, E. Joffrin, U. Kruzei, F. Militello, A. Nielsen, N. Walkden, S. Wiesen, and J. Contributors. Investigation into the formation of the scrape-off layer density shoulder in JET ITER-like wall L-mode and H-mode plasmas. *Nuclear Fusion*, 58(5):056001, 2018.

[106] K. Yamada, S. Tsuji, K. Shimizu, T. Nishitani, and K. N. and. A study of particle confinement properties in ohmically and neutral beam heated hydrogen plasmas in the JT-60 tokamak. *Nuclear Fusion*, 27(8):1203, 1987.

[107] S. J. Zweben, J. L. Terry, D. P. Stotler, and R. J. Maqueda. Gas puff imaging diagnostics of edge plasma turbulence in magnetic fusion devices. *Review of Scientific Instruments*, 88(4):041101, 2017.